

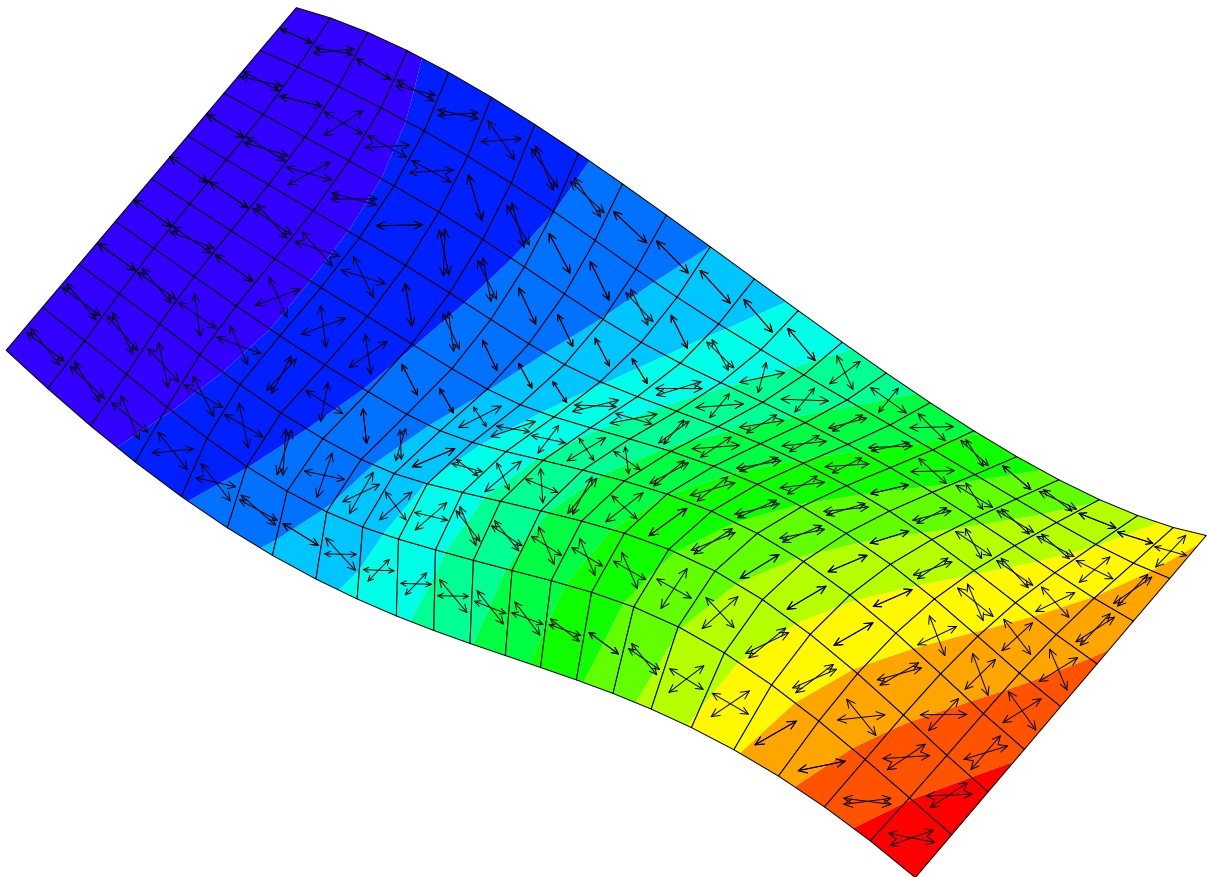
AALBORG UNIVERSITY

DESIGN OF MECHANICAL SYSTEMS

DMS4 PROJECT

N. M. BERTELSEN & N. K. K. STAGSTED

**4-Node Stabilised Shell Element Accounting for Large
Displacements, Drilling and Draping in Structural
Optimisation of Laminated Composites**



01/06-2023



Fifth Year of Study at
The Faculty of Engineering and Science
Design of Mechanical Systems
Fibigerstræde 16
9000 Aalborg

Title:

4-Node Stabilised Shell Element Accounting for Large Displacements, Drilling and Draping in Structural Optimisation of Laminated Composites

Project:

Master's Thesis

Project period:

1. February 2023 -
1. June 2023

ECTS:

30

Participants:

Niklas K. K. Stagsted
Nikolaj Madum Bertelsen

Supervisor:

Erik Lund

Report pagenumber:

97 (5 blank pages)

Attachment pagenumber: 6

Total pagenumber: 122

Concluded 01-06-2023

Synopsis:

Design of laminated composite structures is a complex process that requires the use of efficient modelling and optimisation tools. This thesis presents a finite element formulation with the option to include draping in structural analysis and optimisation. The element is a 4-node shell element stabilised with enhanced assumed strains and mixed interpolation of tensorial components. The element is formulated to account for nonlinearities from large displacements and stress stiffening with a novel penalty method presented for inclusion of the drilling degree of freedom. Discrete material optimisation is used for fibre angle optimisation with draped fibre angles from a decoupled draping analysis included through the rotation of the constitutive matrix. Improved accuracy was achieved in linear tests and improved convergence in geometrically non-linear tests with independence from the drilling penalty observed in almost all cases. Both inclusion of draping and use of discrete material optimisation was successful and yielded different optimal designs in linear compliance optimisation with draping. The 4-node shell element is proved efficient, robust and accurate in analysis and optimisation of laminated composites. Including draping in linear compliance optimisation only showed little gain but more is possible in complex problems and for other optimisation objectives, such as strength.

Preface

This is a master's thesis written during the fourth semester at the M.Sc. program in Design of Mechanical Systems at the Department of Materials and Production at the Faculty of Engineering and Science at Aalborg University. The master's thesis was completed during the period from 1. February 2023 to 1. June 2023.

Source references are placed in the text and refers to the bibliography with the Harvard method. For some chapters that heavily rely on a source it is referenced in the beginning of the chapter to avoid referencing at every equation.

The authors would like to acknowledge Postdoc Christian Krogh for providing expertise on the subject of draping during the initial stages of the project.



Niklas K. K. Stagsted



Nikolaj Madum Bertelsen

Resumé

Design af laminerede kompositstrukturer kan være en kompleks proces som kræver avanceret optimering for at udnytte de specifikke styrke- og stivhedsparametre for fibrene. Som kompositstrukturene bliver større, gør det designprocessen mere kompliceret og modelleringen af den strukturelle opførsel tager længere tid. Dette speciale præsenterer et udbygget 4-knudsers skaelement til brug i optimering for laminerede kompositstrukturer. For at sikre sig robusthed og præcision af skaelementet, vil det blive stabiliseret med enhanced assumed strain og mixed interpolation of tensorial components metoderne for at håndtere låsning af elementet. Arbejdet med optimering af generelle kompositstrukturer nødvendiggør, at den initiale 5 frihedsgraders elementformulering bliver udviklet til at håndtere den sjette frihedsgrad i form af den inplane rotationsfrihedsgrad. For at modellere et større spektrum af strukturelle opførsler, bliver elementformuleringen lavet med Green-Lagrange tøjninger for at medtage store flytninger i formuleringen. Derudover inkluderes en fremstillingsproces, kaldet drapering, som forårsager ændringer i fibervinklerne, når fibermåtter lægges i forme med dobbeltkrumme overflader. Optimeringen er gennemført med diskret materiale optimering ved at anvende diskrete fibervinkler som kandidatmaterialer for den laminerede komposit og vælge den optimale kandidat ved anvendelse af principper fra topologioptimering.

Undersøgelsen for modellering og optimering af laminerede kompositstrukturer med drapering førte til følgende problemformulering:

Udled og implementer et stabiliseret 4-knudsers skaelement med store flytninger og udvikl metoder til at inkludere den inplane rotationsfrihedsgrad og drapering til brug i diskret materiale optimering af laminerede kompositstrukturer

4-knudsers skaelementet er formuleret ud fra en degenerering af et 8-knudsers solidelement gennem formfunktioner og overfladenormalerne i knuderne. Green-Lagrange tøjningen er redegjort for samt de kovariante og kontravariante koordinatsystemer, som bliver anvendt til gennemgangen af tøjning-flytningsforholdet. Sammen med de konstitutive forhold for laminerede kompositter, bliver de styrende ligninger og den numeriske integration på finite element form udledt og sammensat for et 4-knudsers skaelement, der er stabiliseret med enhanced assumed strain og mixed interpolation of tensorial components. For det geometrisk ikke-lineære skaelement bliver lineariseret buling også redegjort for ved Eulers stabilitetsproblem.

For at inkludere den inplane rotationsfrihedsgrad er elementstivhedsmatricen udvidet til en 6 gange 6 matrice, hvor fiktive stivheder bliver lagt ind på den sjette række og søjle. Hvordan de fiktive stivheder skal defineres og effekten af disse stivheder, bliver undersøgt igennem test med et lignende element fra ANSYS. På baggrund af en analyse af de forskellige tests bliver en ny metode foreslået og testet, hvor en simpel fiktiv stivhed bliver anvendt sammen med en koordinattransformation, for at medtage effekten af at have forskellige overfladenormaler i knuderne i forhold til midten af elementet.

Den diskrete materiale optimering bliver gennemgået med beskrivelse af optimeringsproblemerne og parametrene, der bruges til disse. Dette indeholder stivheds- og bulingsoptimering, samt beskrivelser for hvordan metoden sætter diskrete fibervinkler op som kandidatmaterialer og

vælger blandt disse. Dette anvendes med overvejelser for, hvordan drapering bedst kan medtages i parametriseringen og optimeringen.

Den præsenterede elementformulering er testet med ikke-lineære finite element problemer for at se om ikke-lineariteten med store flytninger er inkluderet korrekt. Yderligere bliver forskellige optimeringsproblemer med diskret materiale optimering gennemført med den præsenterede elementformulering og draperings analyser for at undersøge effekten ved anvendelse af disse metoder.

Det bliver konkluderet, at den præsenterede elementformulering og tilføjelser til denne er implementeret korrekt og at den nye metode for inkludering af den inplane rotationsfrihedsgrad er meget fordelagtig for skalelementets præcision samt muliggør fuld seks frihedsgraders analyse. For eksempler med krumme kanter brugt til last eller randbetingelser, blev det observeret, at den fiktive stivhed har en indflydelse, som er problemafhængig, så en mere fysisk baseret stivhed vil være bedre i disse situationer. Optimeringerne med draperede fibervinkler viste, at det kunne resultere i andre optimale fiberretninger. Selvom andre optimale fibervinkler blev fundet med drapering, var der ikke meget forskel på stivheden. Der vil sandsynligvis være større fordele hvis optimeringen udføres på mere komplekse situationer eller med andre optimeringsproblemer som f.eks. styrke.

Nomenclature

Symbols

$[\] , \{ \ }$	Matrix, vector brackets	
$[\sigma], \sigma$	Cauchy stress	Pa
$[\varepsilon], \{\varepsilon\}, \varepsilon_{ij}$	Engineering strain	
$[B]$	Strain-Displacement matrix	$1/m$
$[C]$	Constitutive matrix	
$[E], \{E\}, E_{ij}$	Green-Lagrange Strain	
$[F]$	Deformation gradient	
$[I]$	Identity matrix	
$[k], [k_e]$	Element stiffness matrix	N/m
$[K], [K_T], [K_0], [K_L], [K_\sigma]$	Global, tangent, linear, displacement, stress stiffening matrices	N/m
$[k_{uu}], [k_{\alpha u}], [k_{u\alpha}], [k_{\alpha\alpha}]$	EAS stiffness matrices	N/m
$[M]$	Enhanced Strain Interpolation matrix	
$[S], S_{ij}$	2nd Piola-Kirchhoff Stress	Pa
$[T], [T_\theta]$	Transformation matrix	
$\alpha, \beta, \phi, \theta, drill, \gamma$	Angle	rad
β	Bound	
Δ	Increment	
δ	First variational sign	
δ_i^j	Mixed Kronecker's delta	
γ	Shear strain	
κ	Shear correction factor	
λ	Buckling eigenvalue	
ν	Poisson's ratio	
Π	Total potential energy	J
$\{\alpha\}$	Internal degrees of freedom	

$\{a_i\}$	Material base vectors	
$\{d\}, \{D\}$	Element, Global nodal displacement vector	m
$\{d_i\}$	Local orthonormal base vectors	
$\{e_i\}$	Global base vectors	
$\{f_{int}\}, \{f_{ext}\}, \{f_{eas}\}$	Internal, external and EAS load vectors	N
$\{g^i\}$	Contravariant base vectors	
$\{g_i\}$	Covariant base vectors	
$\{R\}$	Global load or residual vector	N, Nm
$\{r\}, r_e$	External load or residual vector	N, Nm
$\{V_{ij}\}$	Node director i for node j	
B	Body force	N/m^3
C	Compliance	J
E	Young's modulus	GPa
F, f	Force	N
G	Shear modulus	GPa
g_{ij}, g^{ij}	Metric tensor	
h	Height	m
h	Step length	
h_ϵ	Ratio of converged elements	
l, s	Length	m
N	Shape function	
p	Penalty factor	
p_d	Percentage difference	
r	Radius	m
r, s, t	Natural coordinates	
S	Surface, Sensitivity	
T	Traction forces	Pa
t	Thickness	m

U	Strain energy	J
u	Strain energy density	J/m^3
$u_i, \{u\}, \{u, v, w\}$	Displacements	m
V	Volume	m^3
W	Stored energy function	J/m^3
W	Work	J
w_i	Weight functions	
x, y, z	Global coordinates	
x_i	Design variables	
$x_i, \{x\}$	Position, position vector	m

Abbreviations

<i>AAU</i>	Aalborg University
<i>CFAO</i>	Continuous fibre angle optimisation
<i>DMO</i>	Discrete material optimisation
<i>DOF</i>	Degree of freedom
<i>EAS</i>	Enhanced assumed strain
<i>FE</i>	Finite element
<i>FEA</i>	Finite element analysis
<i>FEM</i>	Finite element method/modelling
<i>FRP</i>	Fibre-reinforced polymer
<i>GNL</i>	Geometrically non-linear
<i>MITC</i>	Mixed interpolation of tensorial components
<i>MUST</i>	Multidisciplinary synthesis tool
<i>NCF</i>	Non-crimp fabric
<i>UD</i>	Uni-directional

Contents

Preface	iii
Nomenclature	vii
1 Introduction	1
1.1 Problem Statement	2
1.2 Project Outline	3
2 Problem Analysis	5
2.1 Laminated Composites	5
2.2 Draping of Fibre-Reinforced Polymer Fabrics	7
2.3 Modelling Laminated Composite Shells	12
2.4 Optimisation of Laminated Composites	17
3 Problem Formulation	21
3.1 Requirements	21
3.2 Delimitations	22
4 Large Displacement Formulation of Stabilised 4-node Shell Element	23
4.1 Overview of 4-node Shell Element	23
4.2 Green-Lagrange Strain	26
4.3 Constitutive Relations	33
4.4 Derivation of Governing FE Equations	34
4.5 Numerical Integration of Governing Equations	41
4.6 Linearised Buckling Analysis	43
5 Drilling Degree of Freedom	45
5.1 Inclusion of the Drilling DOF	45
5.2 Effect of Varying Drilling Stiffness	48
5.3 Novel Method for Including Drilling in Curved Shell Elements	52
5.4 Testing of Drilling Method	54
6 Draped Discrete Material Optimisation	61
6.1 Derivation of the DMO Method	61
6.2 Incorporating Draping Into DMO	67
7 Structural Tests for the Element Formulation	71
7.1 Non-Linear Tests of 4-node Shell Element Formulation	71
7.2 Tests of DMO Implementation	79
8 Conclusion	93
9 Future Perspective	95

9.1	Improvements to the Element Formulation	95
9.2	Further Optimisation with Draped Fibre Directions	96
Bibliography		99
A Strain Displacement Matrix		105
A.1	Strain Displacement Matrices on Matrix-Vector Form	105
A.2	Derivative of Strain-Displacement Matrix	106
B Plots for Non-Linear Problems		109
B.1	Residual Plot Spherical Shell Tests	109
B.2	Clamped Angle Response 5 and 6 DOF	110

Introduction 1

Over the years, use of laminated composites as stacked layers of fibre-reinforced polymers (FRPs) and other materials has increased significantly. This is due to the high specific strength and stiffness that can be achieved with low weight along with other desirable properties such as resistance against fatigue and corrosion. These characteristics mean laminated composites are widely used in weight critical structures, such as wind turbine blades, aeroplanes and high-performance bikes and cars amongst many other things. The market for FRP was estimated to be US\$228.8 billion in 2019, which contains the fibre materials such as carbon, glass, aramid, basalt and others. The market experienced negative growth during the COVID-19 lockdown but now is resumed at full capacity and is expected to have a positive growth at a compound annual growth rate of 7.32% from 2019 to 2026 (Research and Markets, 2022).

The use of laminated composites introduces several considerations specific to the design of the laminated composites, increasing the complexity of the design process. The considerations include amongst others the choice of material, fibre orientation in the FRP layers and thickness of each layer as well as the number of layers stacked to create the laminated composite. These considerations must be combined in a manner that best utilises the material properties, while the design is also capable of being manufactured. It is therefore useful to develop methods to systematically handle and ease parts of the design process. For this purpose, the use of suitable structural optimisation tools provides systematic methods of finding the optimal choice for laminate specifications such as fibre orientation with regards to specific structural responses.

Several structural optimisation tools have been developed for this purpose, the one used in this thesis is the MULTidisciplinary Synthesis Tool (MUST) developed at the Department of Materials and Production at Aalborg University. MUST is a finite element based program for mainly structural analysis and optimisation among other subjects. MUST can complete the finite element calculations with different element formulations, but does require commercial software such as ANSYS or Abaqus, for meshing and preprocessing. MUST contains implementations of methods for structural optimisation of laminated composites along with gradient based solvers for optimisation problems. However, a functional geometrically non-linear stabilised 4-node shell element has not yet been implemented successfully and would allow for more efficient finite element modelling and optimisation. Therefore, this thesis will derive and implement a 4-node stabilised shell element with large displacements in MUST.

The derivation of shell elements generally utilises 5 locally defined degrees of freedom (DOFs) at each node by neglecting rotations around the surface normal. This causes difficulty with application of boundary conditions in a global coordinate system with 6 DOFs. Therefore, a drilling DOF is often included in shell elements through the use of various penalisation methods. On a previous semester, the authors derived a geometrically linear 4-node shell element and

discovered in the process a noticeable influence on the accuracy of the element in modelling double curved geometries from the method used to include the drilling DOF. Therefore, the inclusion of the drilling DOF will be investigated further and a novel method for including the drilling DOF is proposed as an extension to the formulation of the shell element.

Furthermore, when specifically double curved geometries with laminated composites are considered, the manufacturing process called draping can also be relevant. On double curved surfaces the fibre orientation of each layer changes throughout the layer, as the fibre fabric experiences shearing in order to conform with the mould surface. The changed fibre orientations throughout each layer influences the stiffness and strength properties of the laminated composite. In structural optimisation, including the draped fibre orientation for a more physically realistic material behaviour may lead to a different layup being the optimal choice. Including draping in structural optimisation would allow for minimisation of the desired structural response more directly. Instead of the more common approach, to optimise draping with regards to minimisation of shearing angles as a measure of the difference compared with nominal fibre orientations or other manufacturing parameters such as material waste. In order to investigate the possibility of further improving double curved laminated composites, a method to account for draping in the structural analysis and optimisation is proposed.

1.1 Problem Statement

This thesis presents a geometrically non-linear stabilised 4-node shell element implemented for structural optimisation of laminated composites in MUST, which is further developed with a novel method for including the drilling DOF and the possibility of taking into account draped fibre orientations.

1.2 Project Outline

The outline of the master's thesis is given below, to give an overview of the process and work made to complete the shell element formulation for use in structural optimisation.

- In chapter 2, the basic knowledge of the fields of interest is obtained and an overview is given for laminated composites in terms of; material behaviour, draping, the finite element method (FEM) and different optimisation methods.
- A more concise description of the problem set out to solve in this master's thesis is given in chapter 3, with requirements for completion.
- In chapter 4, the derivation of the geometrically non-linear stabilised 4-node shell element is presented.
- The inclusion of the drilling DOF is analysed in chapter 5, where a novel method for including the drilling DOF is proposed based on the analyses.
- The optimisation method used with the element is presented in chapter 6 along with the inclusion of draped fibre angles in both analysis and optimisation.
- A number of tests are performed in chapter 7 to validate the shell element and the implementation with structural optimisation in MUST.
- The conclusions of this thesis are gathered in chapter 8 with chapter 9 presenting possible further work within the topics covered.

Problem Analysis 2

In order to derive and implement a shell element for analysis and optimisation of laminated composites, an understanding of the components in a composite laminate is necessary along with the specifications used for design of structures using laminated composites. Additionally, the draping process is analysed to provide insight into how draping influences the structural response. The approach taken to model the laminated composite using shell elements is also presented with an introduction to the geometric non-linearities to account for. The drilling DOF is analysed to determine why it is necessary and provide an overview of existing literature on the subject. Finally, a number of different approaches to structural optimisation of laminated composites are analysed to determine the most suitable approach for this thesis.

2.1 Laminated Composites

Laminated composites are covered extensively in literature and this section will only present the basic definitions as described by Jones (1999), needed for the work presented in this project.

2.1.1 Composition of Composite Laminates and Fibre-Reinforced Polymers

Composites are materials made up of two or more different materials on a macroscopic scale. In laminated composites, this is through the stacking of layers with different material properties. These material properties are derived from the material used, which could be any material, such as metals, polymers, ceramics or composites. Often these layers will be made of fibre-reinforced polymers with fibres and a matrix combined as illustrated in Fig. 2.1 to make layers with high strength and stiffness in the fibre direction.

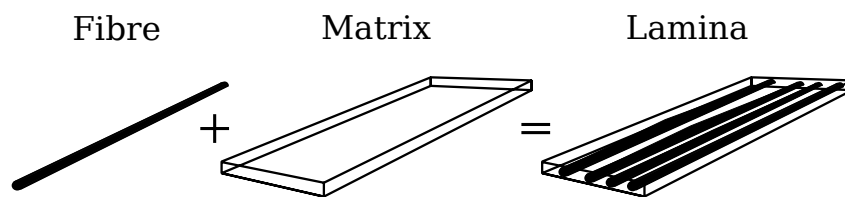


Figure 2.1. Macroscopic components of a fibre-reinforced composite lamina.

In the process of making the FRP layers, the fibres are gathered in bundles called rovings which are used to create fabrics. These fabrics can have different fibre architectures depending on how the rovings are woven or stitched together. In this master's thesis, only the uni-directional (UD) fibre architecture illustrated in Fig. 2.1 is considered. The fabrics are laid out in moulds to conform with the desired geometry of the laminate. If these moulds are double curved, then the fabric will shear and the fibre orientations throughout each layer will change. Since the high stiffness and strength of a FRP layer is achieved along the fibres, the change in fibre orientation

will have an influence on the structural behaviour. Additional layers are made from stacking the fibre fabrics and the FRP lamination process is concluded by infusing resin into the stack of fibre fabrics to create the laminate.

Each layer of the laminate is known as a lamina, with each having different properties depending on the composition of the lamina. The properties of a lamina differs depending on the material used and thickness. If the material used has different properties in different directions as a FRP with UD fibres, then the orientation also affects the properties of the lamina.

2.1.2 Design of Laminates

The properties of the laminate is affected by the properties of each lamina as well as the stacking sequence. In the design of a laminate, the designer can tailor the laminate properties by varying the layup, defined by the sequence of materials, thicknesses and orientations of the chosen number of lamina as illustrated in Fig. 2.2. The layup options make laminated composite designs highly customisable, as desirable properties of the laminate can be achieved. However, the design of laminated composite structures becomes very complex as several new variables can alter the behaviour of the created structure, increasing the amount of feasible designs to chose from in the design process. It is therefore important to be able to determine laminate properties and model laminate behaviour in an efficient and robust manner. The use of optimisation schemes also becomes important, in order to search the feasible design space efficiently and develop optimal designs.

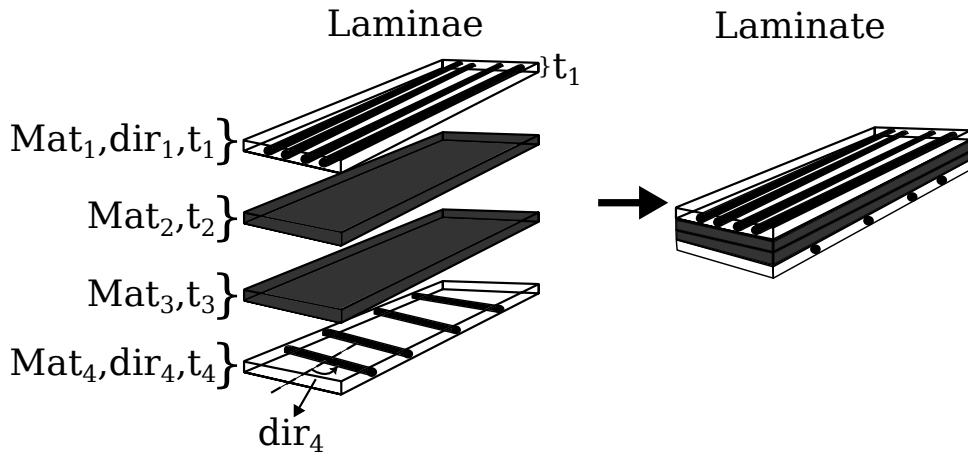


Figure 2.2. Layup of several laminae with laminate specifications. Layup specifications are numbered by the lamina it pertains to such that t_1 , t_2 , t_3 and t_4 can be equal.

In order to differentiate between designs and find the optimum layup, the constraints on the design space and objectives need to be specified. These are highly dependent on the application of the laminate, making it desirable to be able to take into account multiple different constraints and objectives. In laminated composites, constraints on the design space are typically given in terms of requirements towards displacements and strength under different types of loads. The loads can be static or dynamic and the laminate behaviour can involve non-linearity, buckling and delamination amongst others. The objectives can involve optimisation of strength, cost, weight or any conceivable laminate characteristic. Taking into account everything is impossible.

Therefore, this thesis is limited to optimisation with regards to displacements in terms of stiffness under static loading with linear and geometrically non-linear behaviour in addition to buckling behaviour as some of the most commonly encountered structural behaviours.

2.2 Draping of Fibre-Reinforced Polymer Fabrics

Draping is the manufacturing process of conforming initially flat fibre fabrics to moulds in order to obtain the geometry desired from the FRP lamina. In the case of double curved moulds, the fabric conforms through in-plane deformation resulting in changed fibre orientations, as illustrated in Fig. 2.3.

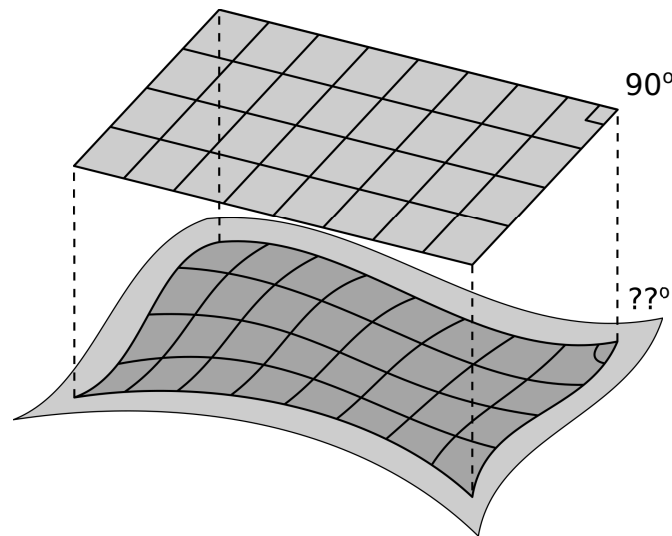


Figure 2.3. Deformation of initially perpendicular fibres to conform with double curved surface resulting in changed fibre angles.

The fibre orientation of FRP laminae serves as a useful parameter for designing laminates with desired properties. For double curved laminate geometries, the draping effect causes fibre orientations in draped lamina to be different from the specified orientations. This results in different laminate properties than expected from a specified layup. Taking into account the draping effect in optimisation of laminated composites might result in different optimal laminate designs. These different optimal laminates can be either better or worse in terms of objective value, however they are based on more accurate modelling of laminate properties if draping is taken into account.

In this section, the draping effect is characterised to determine the parameters pertaining to the draping process with influence on the resulting fibre orientations. Furthermore, modelling approaches presented in literature are analysed and evaluated to determine the most useful method for taking draping into account in optimisation and structural analysis of laminated composites.

2.2.1 Characterisation of Draping Effect

To design a laminated composite structure, FRP in lamina can be built through different fibre architectures, which are the ways to gather the fibres into rovings and the rovings into fabrics. The layup can be made with biaxial behaviour as with the woven fabrics and the biaxial non-crimp fabrics (NCFs) illustrated in Fig. 2.4, where the characterisation methods and draping behaviour is well known (Schirmaier et al., 2016). The biaxial NCF consists of two uni-directional non-crimp fabrics (UD-NCFs) which are stitched together. A UD-NCF illustrated in Fig. 2.4, may also be utilised individually as a lamina which enables greater ability to tailor the laminated composite structure, by allowing each layer to have its fibre direction chosen individually. However, the draping behaviour of UD-NCF has only been investigated sparsely in comparison to the biaxial fabrics (Schirmaier et al., 2016).

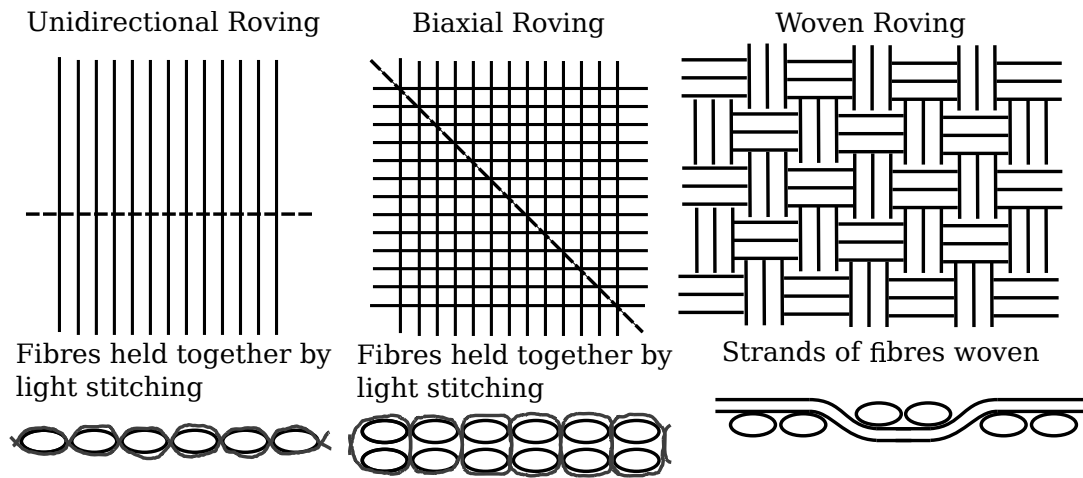


Figure 2.4. Fibre architectures considered with the rovings woven or held together by the stitching illustrated with a dashed line.

Schirmaier et al. (2016) describes the draping characteristics of the woven and biaxial NCF. Through the experimentation of the study, Schirmaier et al. (2016) shows the draping behaviour of stitched UD-NCFs. The woven fabric holds the fibres in place in the cross-over points and can be reasonably approximated as "pin-jointed". Furthermore, the woven fabric exhibits non-linear tensile behaviour that depends on strain ratio. The biaxial NCFs are able to slide between individual layers at the cross-over points and thereby not "pin-jointed". This is caused by only having a light stitching to hold the fibres. Because of the light stitching, the biaxial NCFs show no non-linearities in tensile behaviour and no dependencies on biaxial strain ratio. However, some stitching methods hold the fibres better together and the behaviour will be more akin to the woven fabrics. Additionally, the stiffness of the fabric can be increased in the stitching direction compared to the direction transverse to the stitching. For the UD-NCFs, draping behaviour is distinctly different from the biaxial fabrics with different in-plane deformation modes, highly nonlinear and partly irreversible transverse tensile behaviour and additional wrinkling modes. These differences stem from the lack of cross-over points with other layers. The fibres can more freely slide than even the biaxial NCFs given the lack of friction between additional layers. Depending on the UD-NCF it can sometimes be modelled as undergoing simple shear, where the pin-jointed approximation of woven fabrics corresponds to pure shear (Lim and Ramakrishna,

2002; Fengler et al., 2018). The simple shear and pure shear behaviour is illustrated in Fig. 2.5.

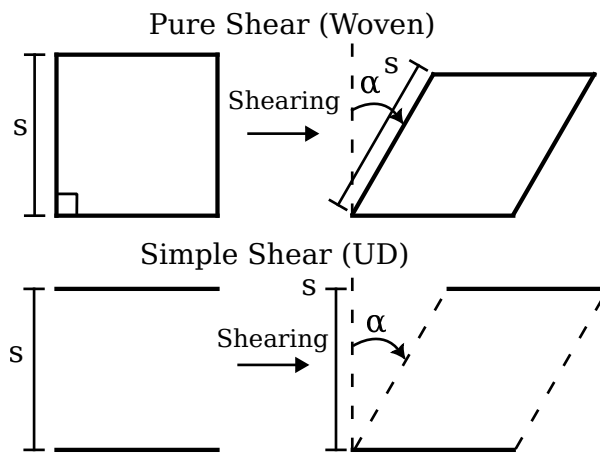


Figure 2.5. Shear behaviour for the modelling of the fabrics.

The chosen fibre architecture used in the fabrics for the FRP lamina influences the draping behaviour and consequently the fibre orientations throughout draped lamina. The fibre fabrics regardless of fibre architecture, behave non-isotropically with properties depending on the orientation of the fibres. Therefore, the orientation of the fibres in the initially flat fabric has an influence on the fibre orientation after draping. The first point of contact with the mould and initial draping direction illustrated in Fig. 2.6, sets the seed from where the fabric deforms in-plane as a point and direction with no deformation in the fabric. It is also possible to apply initial in-plane deformations known as preshear γ_{pre} , to the fabric as a way to alter the resulting fibre orientations (Krogh et al., 2021).

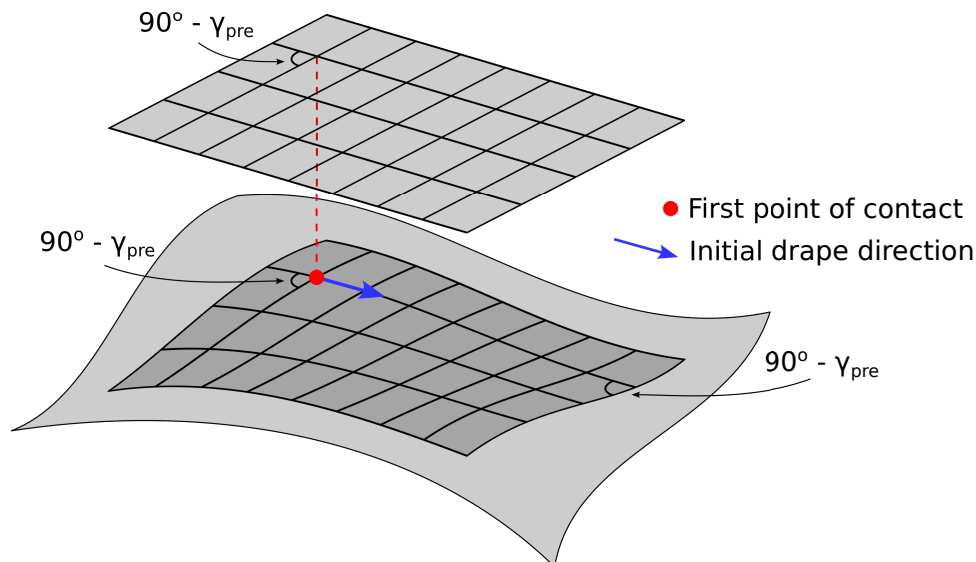


Figure 2.6. Deformation of fabric with preshear resulting from first point of contact and initial draping direction.

For the draping to be accounted for in structural analyses, the change in fibre orientations must be determined. This is typically found through models providing a fibre angle deviation ϕ , illustrated by Fig. 2.7. Another important parameter for cross-ply fabrics is the shear angle γ

defined from the fibre angle deviations of two initially perpendicular fibres.

$$(2.1) \quad \gamma = \phi_1 - \phi_2$$

The fibre angle deviations ϕ_1 and ϕ_2 are defined with counter clockwise rotation as positive. Physically, the shear angle definition is the difference in the angle between two fibres compared to the initially perpendicular angle.

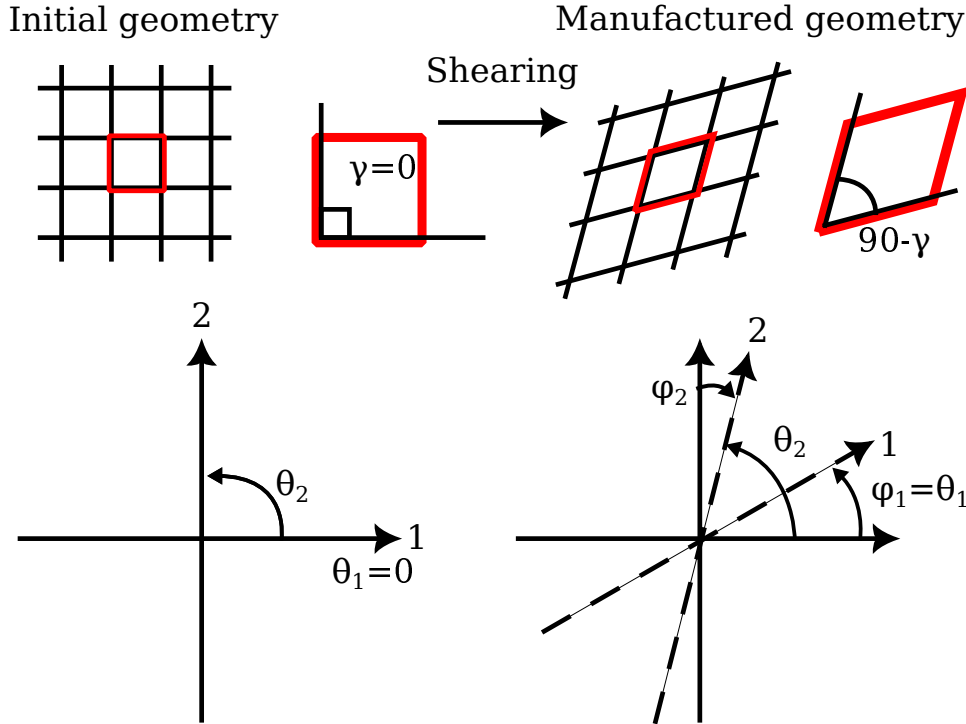


Figure 2.7. Definition of fibre deviation and shear angles in relation to initial and resulting fibre orientations of cross-ply fabrics with two initially perpendicular fibre orientations. θ denotes the fibre orientations, ϕ the fibre deviation angles and γ the shear angle. Note ϕ_2 is clockwise and thereby negative.

The response of a draping analysis that can be used in a structural analysis, are the fibre deviation angles, as these can be included to determine more realistic fibre orientations and structural response. From the draping deviation angles the shearing angle may also be found, which can be used to determine if excessive shear that would lead to wrinkling, is present in the structure. The presence of wrinkling is usually determined by comparing the shear angle to a material limit, called the locking angle.

2.2.2 Modelling of Draped Laminated Composites

The two methodologies that exist in the modelling of the draping effect are the mechanical and kinematic models. The mechanical draping model can use non-linear and dynamic finite element analysis (FEA) to model the elastic constitutive behaviour of the fibres during draping with continuum mechanics. The mechanical models are able to accurately model the draping behaviour for shear angles that exceed the locking angle, as they can include the non-linear effect of increasing shear resistance (Vanclouster et al., 2008). The kinematic model makes several assumptions to solve the draping response numerically for arbitrary surfaces in a more

computationally efficient manner. The assumptions are typically that the fibres can be assumed to have zero shear and bending stiffness, zero slipping and infinite extensional stiffness (Krogh et al., 2021).

Vanloooster et al. (2008) investigated woven fabrics and the difference between kinematic and mechanical models with experimental data and showed that the mechanical model can more accurately model the draping response through a large range of shear angles. It was also shown that the kinematic model fail to accurately describe the large range of shear angles, which is attributed to unrealistic initial conditions and not taking the fabric draping behaviour into account. However, the kinematic model was able to provide accurate results in a range of 15 to 45 degrees shear angle dependent on the situation.

For modelling of biaxial NCFs, it depends on the stitching if similar behaviour to the woven fabrics is observed. If the sliding behaviour should be included, the mechanical model on meso-scale is able to consider the phenomenon (Crech and Pickett, 2006). The meso-scale modelling involves the solid mechanical modelling of the dry tows and stitching at the individual tow and stitch level. The added level of complexity increases the computational costs of the meso-scale mechanical model. Decent accuracy can also be achieved on macro-level by neglecting friction (Thije and Akkerman, 2005).

For UD-NCFs, a kinematic model was developed by Denkena et al. (2021), which replaced the "pin-joints" from the woven fabric approach with "pin-eyes" that allow the carbon rovings to be free and move through the fabric structure without friction, while constraining the spatial distance to each other. The shearing of the textile is subsequently defined by the shift between adjacent rovings.

In taking into account a wider range of draping effects with high accuracy, the mechanical models are superior to the kinematic models. However, with small shear angles and no wrinkling as seen in most structural applications, the kinematic models provide a high computational efficiency and decent accuracy. The low computational costs of the kinematic models make these particularly attractive for optimisation purposes. The kinematic models are also typically used in literature considering draping in optimisation (Fengler et al., 2018; Krogh et al., 2021; Kussmaul et al., 2019).

In this thesis, a kinematic model will be utilised for determining draped fibre orientations and shear angles. Specifically, Abaqus Composites Modeler (Dassault Systemes, 2022) is used. However, the different behaviours of woven, biaxial NCF and UD-NCF mean no general model is applicable for all. In order to maintain a more general applicability of a structural optimisation with draping included, it would be desirable to decouple the draping analysis from the structural optimisation and analysis. This means, the incorporation of draped fibre orientations in structural analyses and optimisation should be independent of the model used to obtain the draped fibre orientations. It will then be possible to apply any suitable draping model including both mechanical and kinematic models.

2.3 Modelling Laminated Composite Shells

The laminated composite models allow for evaluation of the objectives and constraints used to guide the optimisation, from the design variables used to define the designs. As stated in section 2.1.2, this thesis uses the displacements under static loading with linear, geometrically non-linear and buckling behaviour for setting up objectives and constraints. The objectives and constraints are evaluated based on designs defined by the layup in terms of lamina material, orientation and thickness, as illustrated in Fig. 2.2. The designs are also defined by the draping manufacturing parameters used in section 2.2 to model draped fibre orientations, which are taken into account in the laminate models. Laminated composites are typically used to make thin shell structures modelled most efficiently using shell elements in FEAs. Specifically, this thesis applies the 4-node stabilised shell for its high computational efficiency and robustness. This element uses different formulations for modelling linear, geometrically non-linear and buckling behaviour.

A linear 4-node stabilised shell element has already been implemented in MUST by the authors on a previous semester and will be used for the linear analyses (Stagsted and Bertelsen, 2022). However, MUST does not have a working implementation of the 4-node stabilised shell element for geometrically non-linear and buckling analysis. Therefore, an overview of FEA with non-linearity and buckling is presented, to determine what is needed for the derivation and implementation of a stabilised 4-node shell element capable of analysing these phenomena. During implementation of the linear shell element, it was discovered that the inclusion of a drilling DOF in curved shell elements has a significant influence on structural behaviour in curved shell structures. The need for the drilling DOF and existing literature on the subject is presented to provide a basis for further investigation of the influence on structural analysis. Finally, it is described how the draped fibre orientations can be included in FEAs using shell elements.

2.3.1 Linear Element Formulation for Static FEA

The linear element formulation calculates the stiffness matrix $[k_e]$ of each element in a structure, which is used to assemble a global stiffness matrix $[K]$ and solve the set of linear algebraic equations relating nodal DOFs $\{D\}$ to the nodal loads $\{R\}$ (Cook et al., 2001).

$$(2.2) \quad [K]\{D\} = \{R\}$$

In general linear analyses, the element stiffness matrix $[k_e]$ is calculated from the strain displacement relation $[B]$ and constitutive relation $[C]$ using the well known expression derived from the total elastic potential.

$$(2.3) \quad [k_e] = \int_V [B]^T [C] [B] dV$$

The element stiffness matrix used in this thesis, is based on the curved shell element introduced by Ahmad et al. (1970), which has been augmented using enhanced assumed strains (EAS) (Simo and Rifai, 1990; Vu-Quoc and Tan, 2003) and mixed interpolation of tensorial components (MITC) (Dvorkin and Bathe, 1984). The element uses full Gauss integration and models

laminates based on equivalent single layer theory with a penalty stiffness to include a drilling DOF (Cook et al., 2001; Jones, 1999).

Formulating the global stiffness matrix $[K]$ and deriving the global load vector $\{R\}$ allows for the calculation of nodal displacements $\{D\}$. These displacements can be used in the optimisation to setup constraints or objectives directly. The displacements can also be used to calculate strains and stresses through the strain interpolation and constitutive relations. Most failure criteria in general are based on strains and stresses in the structure. Therefore, the use of the linear 4-node stabilised shell element in FEA allows for evaluation of several different failure criteria to be used as constraints or objectives in optimisation.

2.3.2 Geometrically Non-linear Element Formulation for FEA

In static structural analysis there can be several non-linearities present such as, material, contact and geometric. The geometric non-linearities may further be contributed from three parts, which are defined from the displacements, strains and rotations. These may be gathered in different ways as to what seems relevant for the situation. In this thesis, the focus will be on large displacements in the non-linear analyses.

The changes of this non-linearity from a linear static analysis will then be examined. For all geometrically non-linear analyses, the equilibrium equations must be formulated for the deformed configuration. This is handled with different stress and strain definitions that must be work consistent to avoid creating non-physical energy. For the changed strain definition, the Green-Lagrange strain tensor E_{ij} is used to avoid rigid body motion instead of the engineering strain tensor ε_{ij} (Lund and Lindgaard, 2021).

$$(2.4) \quad E_{ij} = \varepsilon_{ij} + \frac{1}{2}\varepsilon_{ij}^2$$

The Green-Lagrange strain tensor E_{ij} is given by the following, where x'_i and x'_j are the vectors/coordinates to the undeformed configuration of the body and u_i is the displacements.

$$(2.5) \quad E_{ij} = \frac{1}{2} \left(\frac{\partial u_i}{\partial x'_j} + \frac{\partial u_j}{\partial x'_i} + \frac{\partial u_k}{\partial x'_i} \frac{\partial u_k}{\partial x'_j} \right)$$

The last term is the non-linear part, which is neglected in linear problems with small displacements, resulting in Cauchy's linearised strain tensor.

From the linear analysis, the stress tensor used is the Cauchy stress tensor σ which is defined as force in deformed configuration per unit of deformed area. For small strains, this stress tensor is consistent with the engineering strain tensor. This works well in a linear analysis where the difference can be neglected, but in a non-linear analysis the deformed area is not known and the deformations are too large to neglect the difference. Therefore, the stress tensor with force on the undeformed configuration per unit of undeformed area called the 2nd Piola Kirchhoff stress tensor S , is needed and used with the Green-Lagrange strain tensor. The difference in the two stress tensors is illustrated in Fig. 2.8 and the strain energy density is consistent with the stress and strain tensors, which results in the following expression (Lund and Lindgaard, 2021).

$$(2.6) \quad \sigma_{ij}\varepsilon_{ij} = S_{ij}E_{ij}$$

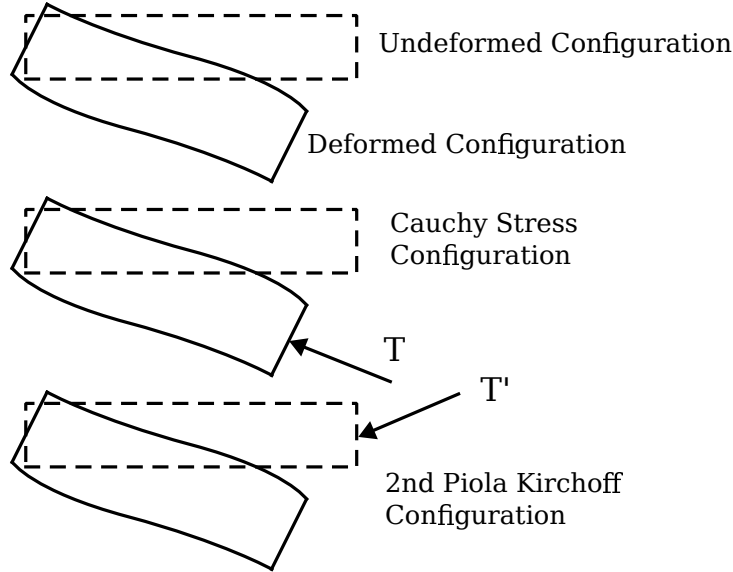


Figure 2.8. Configurations for Cauchy stress tensor with deformed force on deformed area and 2nd Piola Kirchoff stress tensor with undeformed force on undeformed area.

In non-linear analysis, the problem is solved iteratively with steps taken based on a linearisation of the stiffness at each iteration. This stiffness is called the tangent stiffness matrix $[K_T]$ and can be expressed from three parts in a non-linear analysis (Lund and Lindgaard, 2021).

$$(2.7) \quad [K_T] = [K_0] + [K_L(\{D\})] + [K_\sigma(\{\sigma\})]$$

$[K_0]$ is the linear stiffness matrix in Eq. (2.3). $[K_L]$ is the displacement stiffness matrix which contributes the change in stiffness that occurs as the body experiences displacement. $[K_\sigma]$ is the stress stiffness matrix that contributes the stiffness change due to membrane forces $\{F\}$. The change in stiffness given membrane stresses, can also be utilised to analyse structural stability through a linearised Euler stability analysis. The analysis uses the linear and stress stiffness matrices in the linear Euler stability problem, where λ are the eigenvalues and $\{\delta D\}$ are the corresponding eigenvectors (Lund and Lindgaard, 2021).

$$(2.8) \quad ([K_0] + \lambda[K_\sigma(\{F\})])\{\delta D\} = \{0\}$$

The large displacement formulation of the stabilised 4-node shell element requires the derivation of the tangent stiffness matrix. The derivations take offset in the use of the Green-Lagrange strain definition in the expression of the total elastic potential as will be derived in chapter 4.

2.3.3 Drilling DOF in Curved Shells

The element formulation with 5 DOF based on Ahmad et al. (1970), results in a robust and efficient element capable of modelling laminated composite shell structures. However, it comes with a loss in generality from the lack of a drilling DOF for rotation around the surface normal. The DOFs of the 4-node shell element are illustrated in Fig. 2.9.

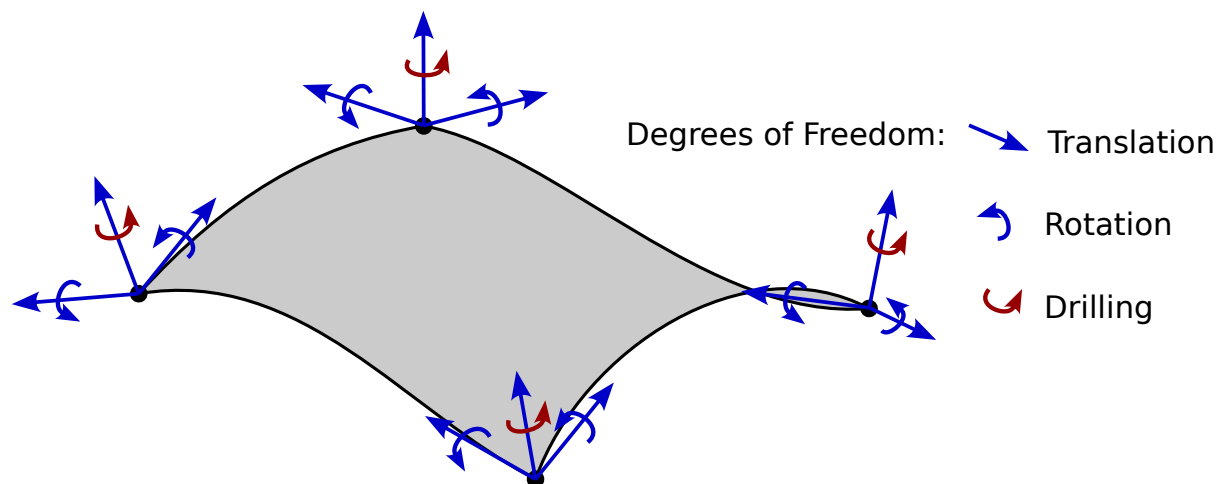


Figure 2.9. Degrees of freedom for a 4-node shell element with the drilling DOF marked in red.

The lack of a drilling DOF results in problems with applying boundary conditions to this type of rotation. This extends to the modelling of T-joints and similar with more than two element edges connected along the same line, as the non-existent drilling DOF can line up with the other rotational DOFs, as illustrated in Fig. 2.10. The drilling DOF is therefore normally included as a 6th DOF in commercial codes based on the 5 DOF formulation using a penalty stiffness. This is done to allow for rotational boundary conditions to be applied in the global structural coordinate system rather than a locally defined system for each node as those illustrated in Fig. 2.9. It also allows the element to be used in T-joints and similar (Lund, 2022; ANSYS Inc., 2018; Dassault Systemes, 2023).

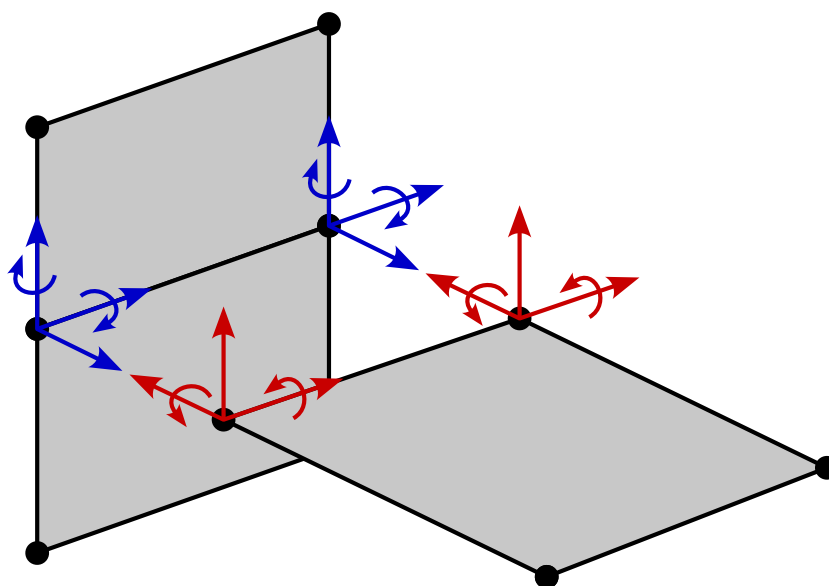


Figure 2.10. T-joint with undefined drilling DOFs lining up with in-plane rotational DOFs.

Several methods exist to include the drilling stiffness around the surface normals in shell elements. However, most of these methods are developed for flat shell elements such as membrane, plate-bending and a combination of these (Yang et al., 2000). In most of these elements the drilling rotation is included as a rotation around the surface normal at the centre

of the element, as the surface normal is the same throughout the flat elements (Gruttmann et al., 1992). A similar approach using a penalty stiffness for rotation around the surface normal at the centre of the element is seen in existing shell elements in MUST and was used for the linear element derived on a previous semester by the authors (Stagsted and Bertelsen, 2022). However, in curved shell elements based on Ahmad et al. (1970) the surface normals at the nodes differ from the surface normal at the element centre prompting the need for a different approach.

One such approach was presented by Fathelrahman et al. (2013) with the degenerated 4-node shell formulation used in this project. Here 3 rotational DOFs are achieved through a transformation of the in-plane rotation applied at each node by Ahmad et al. (1970) and illustrated with blue in Fig. 2.9. This transformation is made prior to the interpolation of the DOFs and thus requires several changes to the derivation of the stiffness matrix. Additionally, Fathelrahman et al. (2013) introduces a constraint on the torsional stiffness which is included in the variational formulation of the element and utilises a torsional constant as a penalty parameter that influences structural response. The most common method to include the drilling DOF in curved shell elements is through a penalty stiffness as done in the shell elements by ANSYS Inc. (2018) and Dassault Systemes (2023). However, literature on the choice of penalty stiffness for shells is sparse with the explanation of the Abaqus penalty stiffness by Tavares et al. (2022) being the only source found by the authors and the method used by ANSYS being undisclosed. In order to provide a general approach that can be applied to 5 DOF degenerated shell elements without significant alterations to the element formulation, a further investigation into the use of a penalty stiffness is made.

Since the penalty stiffness is a fictitious stiffness, it seems reasonable that it should be as small as possible to reduce error, while being large enough that a singular matrix is avoided. However, it was shown by Tavares et al. (2022) that for torsional loads in shell structures, the penalty stiffness should not necessarily be as small as possible even though singularities are avoided. Preliminary studies by the authors also showed a significant influence from the drilling stiffness on the element accuracy in double curved structures. It will therefore be investigated further, how the drilling stiffness affects the element performance in double curved structures and a method for including the drilling stiffness will be proposed and used for the FEAs of this thesis.

2.3.4 Inclusion of Draped Fibre Orientations in FEAs

The fibre angle deviations found from the draping analysis, describe the change in fibre orientation compared to the initially specified or nominal fibre orientations, as illustrated in Fig. 2.7. The draped fibre orientations θ_{drape} can thus be found by adding the fibre angle deviations ϕ to the nominal fibre orientations θ_{nom} .

$$(2.9) \quad \theta_{drape} = \theta_{nom} + \phi$$

The changed fibre orientations cause a change in material properties. These are included in FEAs through the constitutive matrix as exemplified with the linear element stiffness matrix in Eq. (2.3). Jones (1999) describes how the constitutive matrix is calculated for lamina in a laminated composite.

For FRP lamina, the constitutive matrix is initially defined in a material coordinate system, which is aligned with the fibre direction of a UD lamina. For biaxial lamina, the two fibre directions are often separated into individual UD layers when considering the constitutive matrix. The constitutive matrix defined in the material coordinate system, is then rotated in-plane to be aligned with the specified fibre orientation, as illustrated in Fig. 2.11. In a FEA, this rotation is performed for each element and each lamina within that element.

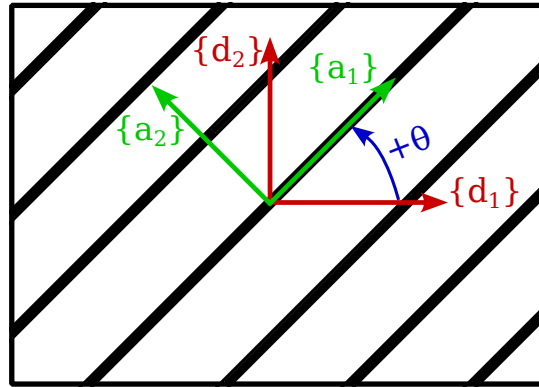


Figure 2.11. Material coordinate system ($\{a_1\}, \{a_2\}$) with in-plane rotation θ from local coordinate system ($\{d_1\}, \{d_2\}$).

The nominal fibre orientation of each lamina is constant within each patch of fabric laid out in the mould. This is changed when accounting for draping, as the draped fibre orientations will be different for each element within the draped patch of fabric. The material properties of a laminate with draped lamina is taken into account by rotating the constitutive matrix of each lamina in each element with the draped fibre orientation θ_{drape} instead of the nominal fibre orientation θ_{nom} .

2.4 Optimisation of Laminated Composites

Given the complexity and high customisability of fibre-reinforced composites, optimisation is a very popular tool and research topic in the design of composite structures. The methodologies can be categorised into the direct and indirect parameterisation with several distinct methods within each category. The main problem that the different parameterisations try to solve, is finding the global optimum in the non-convex design space of laminated composites, illustrated by the curve in Fig. 2.12. The intent of this section is to choose the method for structural optimisation of laminated composites that seems the best fit for incorporating the draping process. Once the optimisation method has been chosen, the possible objectives and design variables to consider in this thesis are specified.

2.4.1 Indirect Parameter Optimisation

The indirect parameters used for optimisation of composite laminates are the lamination parameters introduced by Tsai and Hahn (1980). The lamination parameters are trigonometric functions of the ply orientation and can express the ABD stiffness tensors as linear functions of material stiffness (Bloomfield et al., 2008). This expression allows for a parameterisation

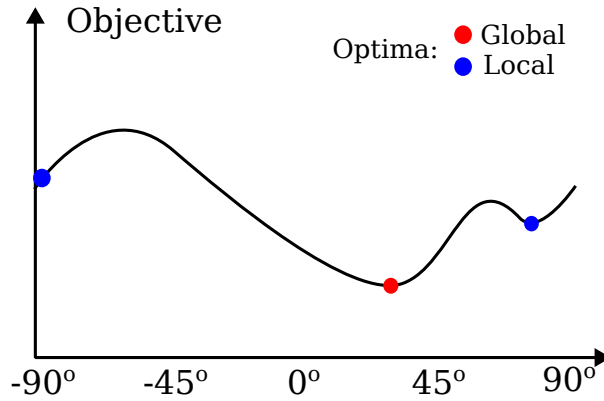


Figure 2.12. Global and local optima for fibre orientation of a single layer laminate with FRP.

of the optimisation problem that is convex, as illustrated in Fig. 2.13. This means gradient based optimisation algorithms can be used without the risk of ending up with local optimum designs. However, it is very difficult to relate constraints to upper and lower bounds on the lamination parameters. Therefore, the methodology has difficulties in incorporating the advanced manufacturing constraints in laminated composite structures and must often use post-processing to reach a manufacturable design (Yan et al., 2022).

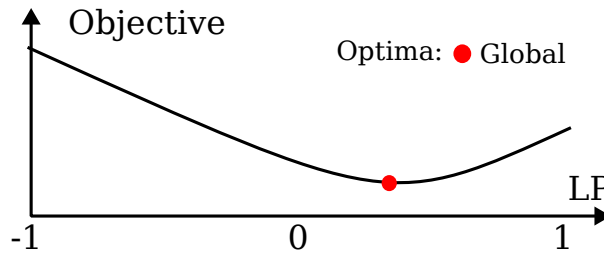


Figure 2.13. Optimisation problem is parameterised indirectly using lamination parameters resulting in a convex design space and no local optima. Post-processing is necessary to determine the fibre orientation corresponding to the optimal value of the lamination parameters.

Using the lamination parameters require a redefinition of the stiffness calculation for the linear shell element to evaluate the laminates. Furthermore, the inclusion of draped fibre orientations will likely involve the derivation of new functions to express the laminate stiffness from the lamination parameters.

2.4.2 Direct Parameter Optimisation

The direct parameter optimisation uses the parameters for the laminate layup as design variables. The main problem with the methodology is the non-convex design space with numerous local minima, making it difficult to obtain the global optimal solution. For methods such as continuous fibre angle optimisation (CFAO) that directly use the fibre orientations as design variables, this often results in the need for genetic algorithms (Yan et al., 2022). The genetic algorithms use random mutation and mixing of the best designs in a set to determine designs for the next set and iteratively find the global optimal solution. This process is very computationally expensive and therefore requires simple setups with few design variables and a small design space to be practically applicable (Arora, 2012). To include the draped fibre orientations, the draping

analysis would need to be included in the design iterations along with the FEAs. This would further increase the computational cost of each iteration and consequently the optimisation.

To achieve a lower computational cost, a different approach has been made with the inspiration of topology optimisation, which is the discrete material optimisation (DMO) method made by Lund and Stegmann (2005); Stegmann and Lund (2005). The DMO method uses principles from multi-material topology optimisation to select the optimal material for a lamina from a set of predefined candidate materials. These candidates can differ in material and for FRP lamina in fibre orientation. The method can be visualised in a simple illustrative example with finding the fibre orientation of a laminate with one lamina, as illustrated by Fig. 2.14. By using candidate materials as a FRP lamina with rotations of -45° , 0° , 45° and 90° , the DMO method will find the candidate with the fibre orientation closest to the optimal. Comparatively with gradient based optimisation, CFAO methods will likely end up in local minima, if the initial fibre orientation is outside the interval created by the neighbouring peaks to the optimum solution. By discretising the design space, the DMO method becomes more likely to find a global optimum. However, the design space is still non-convex and with the use of gradient based optimisation it is still possible for the DMO method to find local optima.

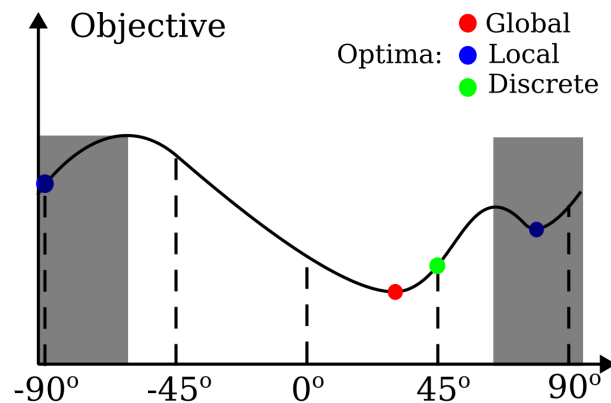


Figure 2.14. Global, local and discrete optima for fibre orientation of a single layer laminate with FRP. The grey regions mark initial fibre orientation values resulting in local optima with CFAO using gradient based methods.

Draped fibre orientations could be included by performing a single draping analysis with each candidate material and using the draped fibre orientations in evaluating the objective, as described in section 2.3.4. The draping itself could also be optimised by defining candidate materials with different draping parameters, such as fibre architecture or first point of contact with the mould. This simple way of including draped fibre orientations in DMO only requires a few draping simulations, which reduces the computational cost of the draping analysis.

2.4.3 Selection of Optimisation Method

The overview of the indirect and direct optimisation methodologies has given insight in which method to utilise in the structural optimisation of laminated composites with draping taken into account. The indirect parameterisation used to obtain a convex optimisation problem allows for gradient based methods to obtain global optima. In spite of that, difficulties with applying

constraints and incorporating draping while requiring post-processing results in the indirect method to be deemed inappropriate.

The direct method can be used with the draping parameters more conveniently added as direct parameters using CFAO to determine fibre orientations. The genetic algorithms are very good methods to achieve well optimised structures. However, the necessity of using genetic algorithms to avoid local minima with the high computational cost does not align well with the inclusion of a draping model. The CFAO approach will therefore not be used.

As a compromise between computational efficiency and robustness, the DMO method is chosen as the optimisation method that will be utilised in the structural optimisation of laminated composites with draping taken into account. The choice is given the gradient based nature of DMO and the possibility of including draping in a simple decoupled manner that is less sensitive to the computational cost of the draping analysis.

Problem Formulation 3

The investigation of laminated composites and draping with a focus on analysis and optimisation through the means of FEM has made it possible to further specify the problem statement put forward in this thesis and propose a solution strategy.

Derive and implement a stabilised 4-node shell element with large displacements and develop methods for including the drilling degree of freedom and draping for use in discrete material optimisation of laminated composites.

This is achieved through completion of the following primary tasks:

- Derive and implement a large displacement formulation of the 4-node stabilised shell element.
- Investigate inclusion of drilling DOF in the shell element and develop a method for including the drilling DOF through use of a penalty stiffness.
- Derive and parameterise discrete material optimisation problems accounting for draped fibre orientations in evaluation of objectives and constraints.

3.1 Requirements

The primary tasks will be considered achieved upon completion of the following requirements.

Large Displacement Formulation of Stabilised 4-node Shell Element

The implementation of the large displacement formulation requires the derivation and calculation of the tangent stiffness matrix from Eq. (2.7). The derivation is achieved based on the Green-Lagrange strains and 2nd Piola Kirchhoff stresses. Completing the derivation and implementation of the large displacement formulation allows for linear buckling in addition to analyses of structures with large displacements.

Drilling Degree of Freedom

For the generality of the element formulation it is required to use a 6 DOF formulation with drilling instead of the 5 DOF formulation. It was mentioned in section 2.3.3 that the inclusion of the drilling DOF has an influence on the element accuracy in double curved structures. This influence is investigated using a commercial element from ANSYS Inc. (2018) to understand the influence on the structural response of using a penalty stiffness to include the drilling DOF. Based on the investigation a new method for including the drilling DOF is proposed.

Discrete Material Optimisation with Draping

It was chosen to utilise the discrete material optimisation (DMO) method as the optimisation method to incorporate draping into and use the stabilised 4-node shell element formulation. The requirements for incorporation of draping are to set up an optimisation problem with draped candidate materials, which is used to analyse the effect of including draping in structural optimisation.

3.2 Delimitations

In order to ensure a feasible scope for this thesis a number of delimitations are made.

- Specifics on the non-linear solvers used or assembly of global system matrices for the FEA is not considered as these are already implemented in MUST.
- Of the various types of non-linearities that can be included only the non-linearity associated with large displacements and stress stiffening is included in the element formulation.
- The validity of the draped fibre angles obtained using Abaqus Composites Modeler (Dassault Systemes, 2022) is not considered, as the focus is on the implementation of the draped fibre angles in the analyses and optimisations.
- DMO is utilised with the optimisation using candidates that only differ in nominal fibre angle.

Large Displacement Formulation of Stabilised 4-node Shell Element 4

This chapter will derive the non-linear large displacement formulation of a 4-node shell element stabilised with MITC and EAS. This is done through an introduction to the shell assumptions and the displacement interpolations specific to the 4-node shell element. The Green-Lagrange strains are necessary to account for large displacements in the strain-displacement relation and are derived in curvilinear coordinates using co- and contravariant bases.

From the Green-Lagrange strains and displacement interpolations, the strain-displacement relation is derived and then modified using MITC to mitigate transverse shear locking. The use of Green-Lagrange strains introduce non-linearity to the governing FE equations which are derived from a linearisation of the first variation in the total elastic potential. Included in the total elastic potential is the enhanced strains following the EAS method to mitigate in-plane shear locking. Finally, the numerical integration of stiffness terms in the governing equations results in the stiffness matrices used in geometrical nonlinear static analysis and linearised buckling analysis.

4.1 Overview of 4-node Shell Element

The formulation of the shell element originates from Ahmad et al. (1970) which present the shell element as an element capable of efficiently being able to describe three dimensional curved geometry with a two dimensional element. The shell element is a surface which is allowed to be curved, often defined as the mid-surface from the inner and outer surfaces of the solid element. These surfaces are separated with a comparatively small thickness. The overview presented in this section is based on Cook et al. (2001) and Lund (2022).

4.1.1 Degeneration of 8-node Solid Element

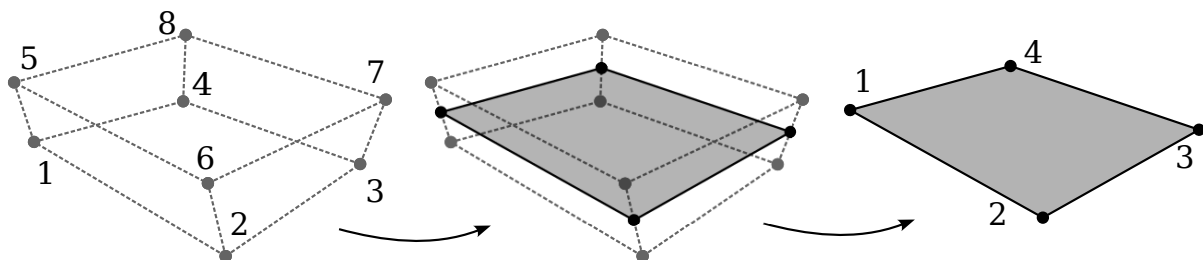


Figure 4.1. Degeneration method applied to an 8-node solid element to achieve a 4-node shell element.

One of the ways to achieve the described characteristics is to degenerate an 8-node solid element into a 4-node shell element, as illustrated in Fig. 4.1. The degeneration is achieved by combining opposing nodes in the thickness direction at the mid-surface to reduce the number of nodes from 8 to 4. The translational displacements of the mid-surface nodes are equal to the average of the outer surface nodes and rotation around the mid-surface nodes are used to describe the difference between the outer surface nodes.

4.1.2 Node Directors

By adding two rotational DOFs to the mid-surface nodes as rotations of node directors, positions throughout the element can be described using 5 DOFs per node. Node directors are used to describe the displacement from the surface nodes. The thickness node director $\{V_{3i}\}$ for node i is defined as the unit vector pointing from the bottom surface node $\{X_i^{bottom}\}$ to the top node $\{X_i^{top}\}$ separated by the height h_i .

$$(4.1) \quad \{V_{3i}\} = \frac{\{X_i^{top}\} - \{X_i^{bottom}\}}{h_i}$$

In order to describe the rotation of the node director $\{V_{3i}\}$, a director coordinate system is defined. The other vectors in this coordinate system are defined from cross product (\times) of the node director and Cartesian coordinate system ($\{e_1\}, \{e_2\}, \{e_3\}$).

$$(4.2) \quad \{V_{1i}\} = \frac{\{e_2\} \times \{V_{3i}\}}{\|\{e_2\} \times \{V_{3i}\}\|}$$

$$(4.3) \quad \{V_{2i}\} = \{V_{3i}\} \times \{V_{1i}\}$$

The use of node directors allow for the position within the element to be described from the mid-surface nodes and a distance along the node director. This conforms with the Reissner-Mindlin shell theory as the following assumptions are enforced when using the node directors as illustrated in Fig. 4.2.

1. Transverse normals are inextensible.
2. Transverse normals remain straight after deformation.
3. Transverse normals are allowed to rotate.

The Reissner-Mindlin shell assumptions and resulting element characteristics have some limitations as a result of the simplified element behaviour. The inextensible transverse normals correspond to a plane strain assumption meaning the transverse normal strain ϵ_{33} is equal to 0. By allowing the transverse normals to rotate and requiring them to remain straight, the transverse shear strains will be constant through the thickness. Both of these effects have an influence on the definition of the constitutive matrix, which will be covered in section 4.3. Despite the mentioned results of the assumptions, the Reissner-Mindlin theory provides good results for thin to moderately thick shells.

4.1.3 Positional and Displacement Interpolations

The change from an 8-node solid element with 3 DOFs per node to a 4-node shell element with 5 DOFs per node is achieved through the displacement interpolation. Geometric interpolation

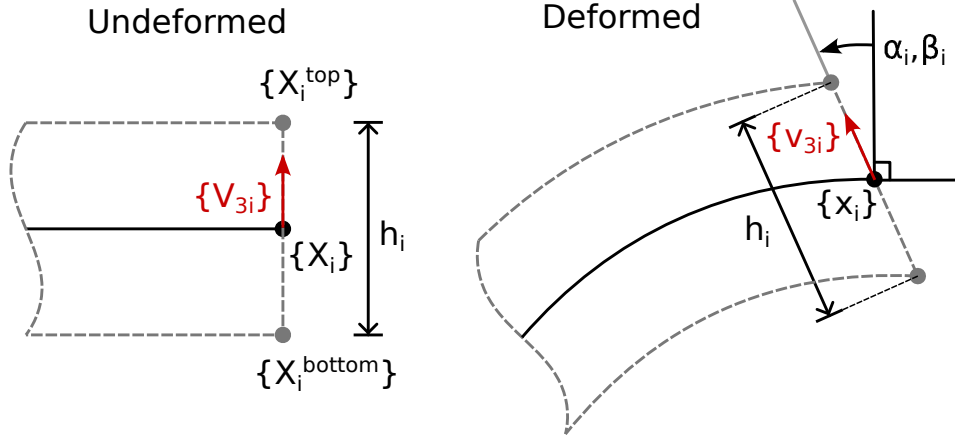


Figure 4.2. Node directors on the shell element from a degenerated solid element. Rotation of transverse normal by α or β with inextensible transverse normal.

is used to describe positions and displacements for a continuous body through the nodal values. For the three dimensional 8-node solid element the interpolation used is

$$(4.4) \quad N_i^{3D} = \frac{1}{8}(1 \pm r)(1 \pm s)(1 \pm t)$$

The interpolation is split into an in-plane part and thickness-direction part respectively.

$$(4.5) \quad N_i^{2D} = \frac{1}{4}(1 \pm r)(1 \pm s)$$

$$(4.6) \quad N_i^t = \frac{1}{2}(1 \pm t)$$

The position $\{x\}$ can be described from the in-plane interpolation between the mid-surface nodes $\{x_i\}$ to describe the mid-surface and a thickness interpolation using the node director $\{V_{3i}\}$ to describe positions away from the mid-surface (Ahmad et al., 1970).

$$(4.7) \quad \{x\} = \sum_{i=1}^4 N_i^{2D} \{x_i\} + \sum_{i=1}^4 \frac{t}{2} N_i^{2D} h_i \{V_{3i}\}$$

Displacements $\{u\}$ are defined as the change from the position in the undeformed configuration $\{X\}$ to the position in the deformed configuration $\{x\}$.

$$(4.8) \quad \{u\} = \{x\} - \{X\}$$

The displacements may then be interpolated as done with the position.

$$(4.9) \quad \{u\} = \sum_{i=1}^4 N_i^{2D} \{u_i\} + \sum_{i=1}^4 \frac{t}{2} N_i^{2D} h_i (\{v_{3i}\} - \{V_{3i}\})$$

The displacements $\{u\}$ are thus expressed from the translational DOFs $\{u_i\}$ of node i and the change in the node director $(\{v_{3i}\} - \{V_{3i}\})$. This change must be expressed in terms of DOFs and is achieved through the rotations of the director coordinate system, which is illustrated in Fig. 4.3.

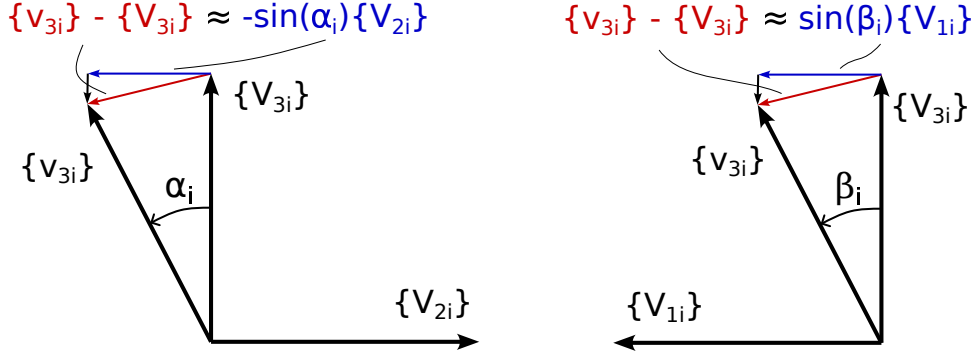


Figure 4.3. In-plane rotation α and β about $\{V_{1i}\}$ and $\{V_{2i}\}$ respectively, used to express the difference between the deformed and undeformed node director $v_{3i} - V_{3i}$.

α and β are defined as the angles of rotation around the $\{V_{1i}\}$ and $\{V_{2i}\}$ vectors respectively. With small rotations considered, the contribution from α can be approximated by only including the $\{V_{2i}\}$ directional part as $-\sin(\alpha_i)\{V_{2i}\}$, which can be further linearised as $-\alpha_i\{V_{2i}\}$. Similarly, the addition of β is approximated to be $\sin(\beta_i)\{V_{1i}\}$ and linearised to $\beta_i\{V_{1i}\}$. Adding the rotational DOF terms together gives the final approximation of the change in node director.

$$(4.10) \quad \{v_{3i}\} - \{V_{3i}\} = -\alpha_i\{V_{2i}\} + \beta_i\{V_{1i}\}$$

This is used to achieve interpolation of the displacements through the 5 DOFs.

$$(4.11) \quad \{u\} = \sum_{i=1}^4 N_i^{2D} \{u_i\} + \sum_{i=1}^4 \frac{t}{2} N_i^{2D} h_i (-\alpha_i\{V_{2i}\} + \beta_i\{V_{1i}\})$$

This can be expressed using an interpolation matrix $[N]$ and the nodal DOFs $\{d\}$.

$$(4.12) \quad \{u\} = [N]\{d\}$$

$$(4.13) \quad [N] = \left[\begin{array}{ccc|cc} N_i^{2D} & 0 & 0 & -\frac{t}{2} N_i^{2D} h_i \{V_{2i}\} & \frac{t}{2} N_i^{2D} h_i \{V_{1i}\} \\ \dots & 0 & N_i^{2D} & -\frac{t}{2} N_i^{2D} h_i \{V_{2i}\} & \frac{t}{2} N_i^{2D} h_i \{V_{1i}\} \\ \dots & 0 & 0 & N_i^{2D} & -\frac{t}{2} N_i^{2D} h_i \{V_{2i}\} & \frac{t}{2} N_i^{2D} h_i \{V_{1i}\} \end{array} \right]$$

$$(4.14) \quad \{d\} = \{\dots | u_i, v_i, w_i, \alpha_i, \beta_i | \dots\}$$

The rotation around $\{V_{3i}\}$ is the drilling rotation that is not initially considered in the displacement interpolation, as it will not contribute to the displacements and therefore should not be expected to carry any load. The drilling DOF will later be investigated and added in chapter 5 with a stiffness penalty.

4.2 Green-Lagrange Strain

Before the Green-Lagrange strain can be introduced, covariant and contravariant bases will be introduced as a useful base to represent the strain definition and the deformation gradient will be introduced as a concept used to define the strain tensor. Then the Green-Lagrange strains are introduced and used to derive the strain-displacement matrix relating the strains to the nodal DOFs.

4.2.1 Covariant and Contravariant Bases

For the interpolation of position and displacement, the natural coordinates are used due to a number of beneficial properties in the definition of the natural coordinates. However, the definition results in natural coordinates being defined in a generally curvilinear coordinate system, which are normally related to global Cartesian coordinates by the use of co- and contravariant bases.

In the element formulation as presented by Vu-Quoc and Tan (2003), the covariant base $\{G_i\}$ is defined by tangent vectors to the curvilinear coordinate axes R, S, T defined from the positional vector $\{X\}$ in a global orthonormal coordinate system, as illustrated in Fig. 4.4. For the strain definition, a distinction is made between the undeformed state denoted by uppercase letters and the deformed state denoted by lower case letters.

$$(4.15) \quad \{G_i\} = \frac{\partial\{X\}}{\partial R_i} \quad i = 1, 2, 3 \quad R_i = R, S, T$$

$$(4.16) \quad \{g_i\} = \frac{\partial\{x\}}{\partial r_i} \quad i = 1, 2, 3 \quad r_i = r, s, t$$

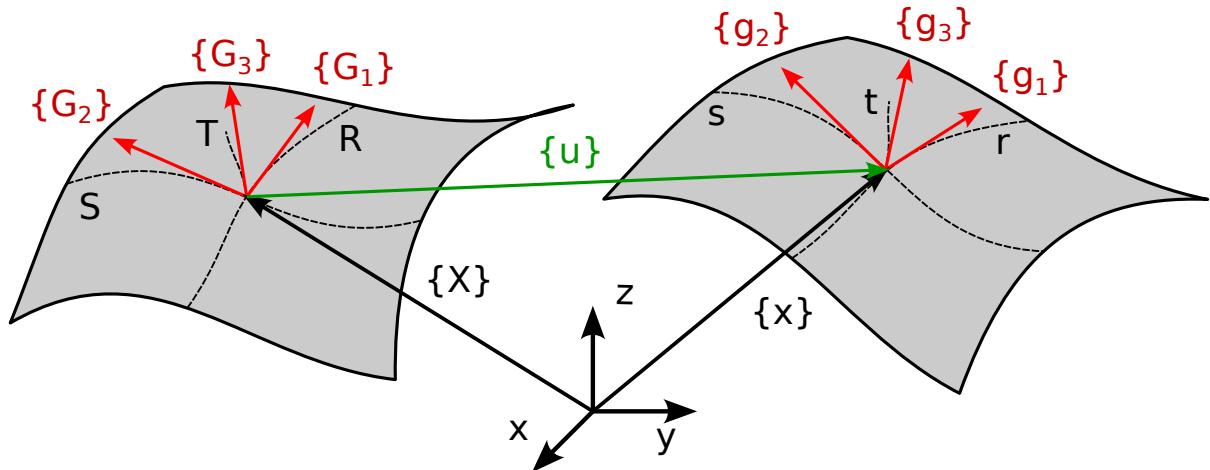


Figure 4.4. Covariant base and natural coordinates with positional vectors and displacements on undeformed shell surface to the left and deformed shell surface to the right.

The definition of the covariant base makes it non-orthogonal and not of unit length, as may be seen from Fig. 4.4. Due to the non-orthogonality, it is necessary to consider how quantities such as vectors and tensors are represented in the base. For example, a vector can be expressed by projections onto the base vectors of a coordinate system as illustrated in Fig. 4.5a. However, parallel and perpendicular projections are distinct with non-orthogonal bases and only the parallel projections add up to give the represented vector as illustrated by Fig. 4.5b. The vector components of the parallel projection are known as contravariant and denoted by a superscripted index v^i , while the components of the perpendicular projection are known as covariant and denoted by a subscripted index v_i . The two projections are equal in orthogonal coordinates denoted by the bar over the component as \bar{v}_i (Heinbockel, 1996; Fleisch, 2012).

$$(4.17) \quad \{v\} = \bar{v}_1\{e^1\} + \bar{v}_2\{e^2\} = v^1\{g_1\} + v^2\{g_2\} \neq v_1\{g_1\} + v_2\{g_2\}$$

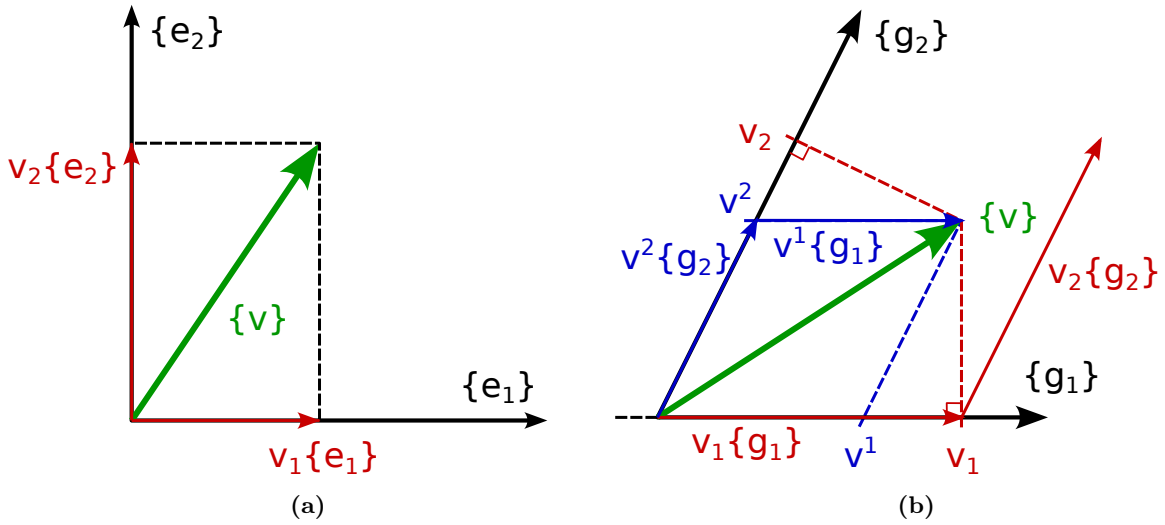


Figure 4.5. Parallel and perpendicular projections of vector $\{v\}$ onto orthonormal base $\{e_i\}$ in (a) and non-orthogonal and not of unit length base $\{g_i\}$ in (b).

To allow for the use of the perpendicular projection, a contravariant base $\{g^i\}$ is defined as the reciprocal base to the covariant base. For the contravariant base, the projections of covariant and contravariant components are switched, meaning the covariant components are projected parallel onto the base. This allows for a dual base representation of the vector using contravariant components v^i with the covariant base $\{g_i\}$ and vice versa as illustrated in Fig. 4.6 (Fleisch, 2012).

$$(4.18) \quad \{v\} = v_1\{g^1\} + v_2\{g^2\} = v^1\{g_1\} + v^2\{g_2\}$$

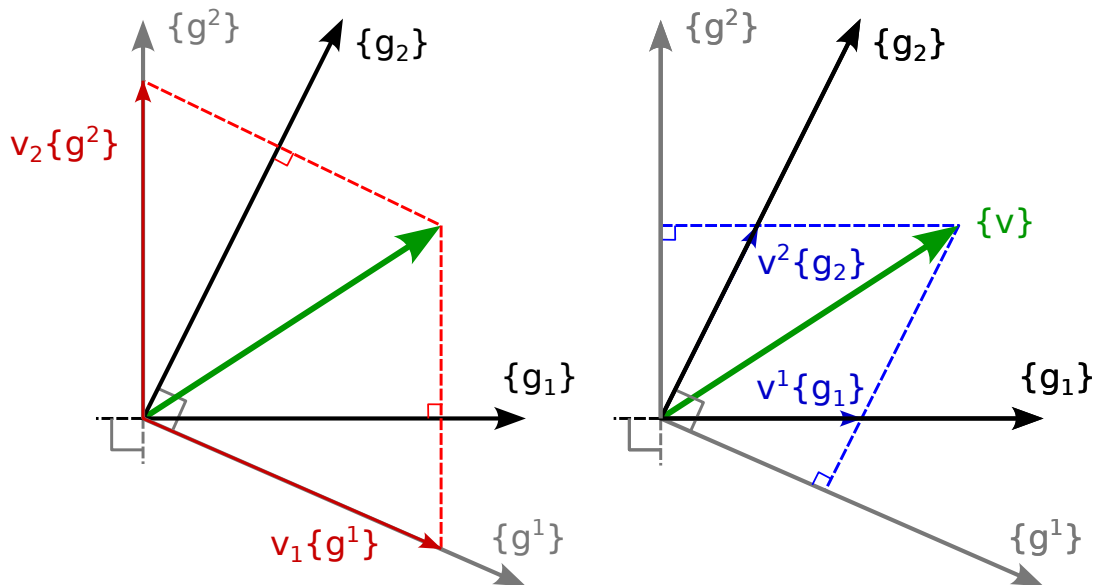


Figure 4.6. Parallel projection of the vector $\{v\}$ onto covariant $\{g_i\}$ and contravariant $\{g^i\}$ bases with perpendicular projections marked on corresponding reciprocal bases.

The definition of the contravariant base means, it can be calculated as the inverse of the covariant base and these bases satisfy a useful relation.

$$(4.19) \quad \{g^i\} = \{g_i\}^{-1}$$

$$(4.20) \quad \{g_i\} \cdot \{g^j\} = \delta_i^j$$

The (\cdot) operator denotes the inner product of the two vectors. δ_i^j is known as the mixed Kronecker's delta which switches the index of a tensor. In matrix-vector notation it is equivalent to multiplying with the identity matrix. This means a transformation from contravariant components to covariant components can be made with the following.

$$(4.21) \quad v_i \{g^i\} = v^j \{g_j\}$$

$$(4.22) \quad v_i \{g^i\} \cdot \{g_k\} = v_i \delta_k^i = v_k = v^j \{g_j\} \cdot \{g_k\}$$

The relationship between the co- and contravariant bases provides a useful property, when multiplying two quantities expressed in the co- and contravariant bases. This is shown below with the multiplication of strains $[\varepsilon]$ and stresses $[\sigma]$ (Fleisch, 2012). The strains and stresses are written in matrices below to conform with the indices used for the components ε_{ij} and σ^{ij} . In later derivations the strains and stresses are reordered into vectors for simplicity.

$$(4.23) \quad [\sigma] \cdot [\varepsilon] = \sigma^{ij} \{G_i\} \otimes \{G_j\} \varepsilon_{kl} \{G^k\} \otimes \{G^l\}$$

$$(4.24) \quad = \sigma^{ij} \varepsilon_{kl} (\{G_i\} \cdot \{G^k\}) (\{G_j\} \cdot \{G^l\}) = \sigma^{ij} \varepsilon_{kl} \delta_i^k \delta_j^l = \sigma^{ij} \varepsilon_{ij}$$

The (\otimes) operator denotes an outer product of the vectors. By using contravariant stress components and covariant strain components, the base vectors cancel out and the representation of the product is invariant. This is used in the evaluation of the governing equations and is the reason behind the definitions of covariant Green-Lagrange strain components and contravariant constitutive components derived in the following sections (Vu-Quoc and Tan, 2003).

In the derivation of the covariant components of the Green-Lagrange strains, a special tensor known as the metric tensor (g_{ij}, g^{ij}) is used. This tensor is defined from the co- and contravariant bases and can be used to switch between the bases (Vu-Quoc and Tan, 2003).

$$(4.25) \quad g_{ij} = \{g_i\} \cdot \{g_j\} \qquad g^{ij} = \{g^i\} \cdot \{g^j\}$$

$$(4.26) \quad \{g_i\} = g_{ij} \{g^j\} \qquad \{g^i\} = g^{ij} \{g_j\}$$

4.2.2 Green-Lagrange Strain Tensor

The definition of the Green-Lagrange strains $[E]$ follows from the difference in length between two points in the deformed and undeformed configurations relative to the initial length. This can be expressed in convective coordinates from the co- and contravariant bases with the deformation gradient $[F]$ and the identity matrix $[I]$.

$$(4.27) \quad [E] = \frac{1}{2} ([F]^T [F] - [I])$$

The deformation gradient describes a change in position in the deformed state relative to a positional change in the undeformed state. This can be expressed by the outer product of the

covariant base in the deformed state $\{g_i\}$ and the contravariant base in the undeformed state $\{G^i\}$.

$$(4.28) \quad [F] = \frac{\partial\{x\}}{\partial\{X\}} = \{g_i\} \otimes \{G^i\} = \begin{bmatrix} \frac{\partial x_1}{\partial X_1} & \frac{\partial x_1}{\partial X_2} & \frac{\partial x_1}{\partial X_3} \\ \frac{\partial x_2}{\partial X_1} & \frac{\partial x_2}{\partial X_2} & \frac{\partial x_2}{\partial X_3} \\ \frac{\partial x_3}{\partial X_1} & \frac{\partial x_3}{\partial X_2} & \frac{\partial x_3}{\partial X_3} \end{bmatrix}$$

The identity matrix can also be described with respect to convective coordinates.

$$(4.29) \quad [I] = G_{ij}\{G^i\} \otimes \{G^j\}$$

The Green-Lagrange strain tensor may then be expressed by the covariant components in the contravariant base.

$$(4.30) \quad [E] = \frac{1}{2}(g_{ij} - G_{ij})\{G^i\} \otimes \{G^j\}$$

It is only the covariant components E_{ij} of the strain tensor that is needed and these are described by

$$(4.31) \quad E_{ij} = \frac{1}{2}(g_{ij} - G_{ij})$$

The definition of the metric tensor in the deformed state g_{ij} can be expanded using the displacements $\{u\}$ and covariant base in the undeformed state $\{G_i\}$ as shown in Vu-Quoc and Tan (2003).

$$(4.32) \quad \begin{aligned} g_{ij} &= \{g_i\} \cdot \{g_j\} = \left(\{G_i\} + \frac{\partial\{u\}}{\partial r^i} \right) \cdot \left(\{G_j\} + \frac{\partial\{u\}}{\partial r^j} \right) \\ &= G_{ij} + \{G_i\} \cdot \frac{\partial\{u\}}{\partial r^j} + \frac{\partial\{u\}}{\partial r^i} \cdot \{G_j\} + \frac{\partial\{u\}}{\partial r^i} \cdot \frac{\partial\{u\}}{\partial r^j} \end{aligned}$$

With the expanded definition of the metric tensor in the undeformed state, it is possible to express the covariant components of the Green-Lagrange strain tensor in terms of the displacements.

$$(4.33) \quad E_{ij} = \frac{1}{2} \left(\{G_i\} \cdot \frac{\partial\{u\}}{\partial r^j} + \frac{\partial\{u\}}{\partial r^i} \cdot \{G_j\} + \frac{\partial\{u\}}{\partial r^i} \cdot \frac{\partial\{u\}}{\partial r^j} \right)$$

The Green-Lagrange strain tensor expressed in covariant components must then be used with the 2nd Piola-Kirchoff stress tensor in contravariant components S^{ij} .

$$(4.34) \quad [S] = S^{ij}\{G_i\} \otimes \{G_j\}$$

The 2nd Piola-Kirchoff stress tensor is used to ensure work consistency for the governing equations in section 4.4. The contravariant components are used due to the useful relation between covariant and contravariant components shown in Eq. (4.24). The contravariant stress tensor can be described with the contravariant components of the constitutive relation and covariant strain components as explained in section 4.3.

$$(4.35) \quad S^{ij} = C^{ijkl}E_{kl}$$

4.2.3 Strain-Displacement Relation

In order to setup governing equations that can be solved for the nodal DOFs $\{d\}$, these must be used to describe the strains $\{E_{ij}\}$. This is generally done through the use of a strain-displacement matrix $[B]$, which is dependent on the nodal DOFs when using the Green-Lagrange strain definition. The strain displacement matrix is defined from increments and variations made in the DOFs when deriving of the governing FE equations, which relate to increments and variations in strains through the chain rule.

$$(4.36) \quad \Delta\{E_{ij}\} = \frac{\partial\{E_{ij}\}}{\partial\{d\}} \Delta\{d\} = [B(\{d\})] \Delta\{d\}$$

where $\{E_{ij}\}$ is the covariant components of the Green-Lagrange strain rearranged as a 6×1 vector.

$$(4.37) \quad \{E_{ij}\} = \{E_{11}, E_{22}, E_{33}, 2E_{12}, 2E_{23}, 2E_{13}\}^T$$

The strain-displacement matrix can be split into a linear B_0 and nonlinear B_L part from the Green-Lagrange strain from Eq. (4.33), where the Green-Lagrange strain may be described from the strain-displacements matrices.

$$(4.38) \quad [B(\{d\})] = [B_0] + [B_L(\{d\})]$$

$$(4.39) \quad [B_0]\{d\} = \frac{1}{2} \left(\{G_i\} \cdot \frac{\partial\{u\}}{\partial r^j} + \frac{\partial\{u\}}{\partial r^i} \cdot \{G_j\} \right)$$

$$(4.40) \quad [B_L(\{d\})]\{d\} = \frac{\partial\{u\}}{\partial r^i} \cdot \frac{\partial\{u\}}{\partial r^j}$$

$$(4.41) \quad \{E_{ij}\} = ([B_0] + \frac{1}{2}[B_L(\{d\})])\{d\}$$

The displacement field $\{u\}$ from Eq. (4.12) is used and repeated again below. Since the nodal DOFs are independent from the natural coordinates the derivatives can be taken as shown below.

$$(4.42) \quad \{u\} = [N]\{d\}$$

$$(4.43) \quad \frac{\partial\{u\}}{\partial r_i} = \frac{\partial[N]}{\partial r_i} \{d\}$$

Inserting the displacement field derivatives into Eq. (4.39) and (4.40) allows for covariant components of the Green-Lagrange strain to be determined from the nodal displacement in a linear and nonlinear contribution, which is stated respectively.

$$(4.44) \quad [B_0]\{d\} = \frac{1}{2} \left(\{G_i\} \cdot \frac{\partial[N]}{\partial r_j} + \{G_j\} \cdot \frac{\partial[N]}{\partial r_i} \right) \{d\}$$

$$(4.45) \quad [B_L]\{d\} = \{d\} \cdot \frac{\partial[N]}{\partial r_i} \cdot \frac{\partial[N]}{\partial r_j} \cdot \{d\}$$

$$(4.46) \quad \{E_{kl}\} = \{E_{11}, E_{22}, E_{33}, 2E_{12}, 2E_{23}, 2E_{13}\}^T = [B_0]\{d\} + \frac{1}{2}[B_L(\{d\})]\{d\}$$

In FE implementation it is required to construct the strain-displacement relation with a strain-displacement matrix. The construction with derivations, is given in appendix A.

4.2.4 Mixed Interpolation of Tensorial Components

To improve the stability and representation of transverse shear strains, the MITC method is utilised. The MITC method is an assumed natural strain or \bar{B} -method, which is applied through alterations to the strain-displacement matrix $[B]$. This is done by re-interpolating transverse shear strains from the points that provide the correct strains for the isoparametric formulation in the case of pure bending. The points are called tying points A, B, C, D and for a 4-node shell element the points are located at the centre of the element edges (Dvorkin and Bathe, 1984), as illustrated in Fig. 4.7a.

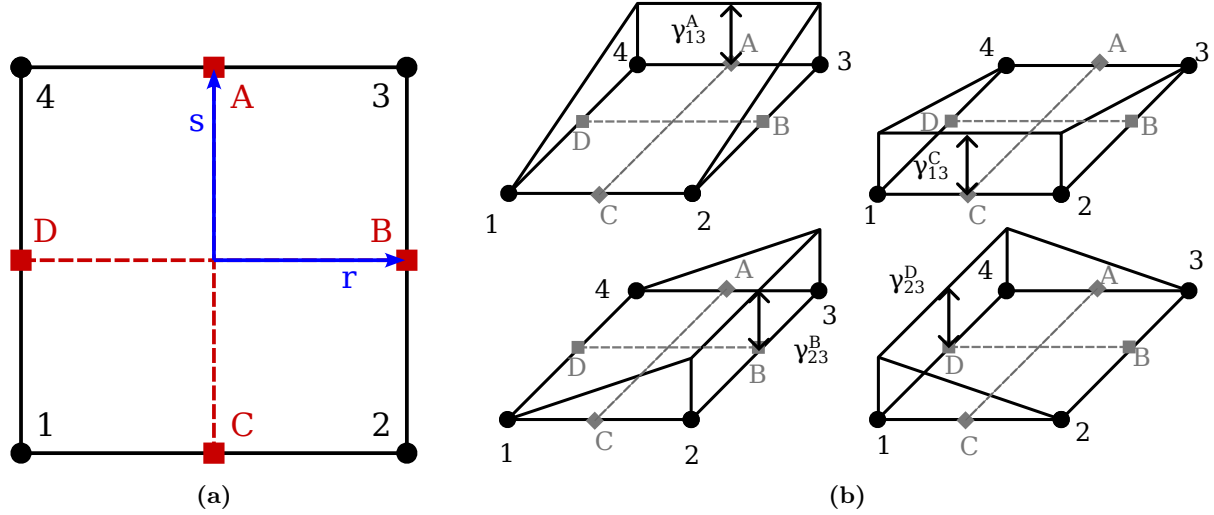


Figure 4.7. Tying points located on element in natural coordinates and transverse shear strain interpolation from tying points.

The re-interpolation of the strains is achieved by a change in the last two rows of the strain-displacement matrix.

$$(4.47) \quad [B] = \begin{bmatrix} [B_{11}] \\ [B_{22}] \\ [B_{33}] \\ [B_{12}] \\ [B_{23}] \\ [B_{13}] \end{bmatrix} \rightarrow \begin{bmatrix} [B_{11}] \\ [B_{22}] \\ [B_{33}] \\ [B_{12}] \\ [B_{23}^{MITC}] \\ [B_{13}^{MITC}] \end{bmatrix}$$

The new two last rows consist of new interpolation functions, which are related to a tying point and linearly varying from a value of 1 at the tying point to 0 at the opposing tying point, as illustrated in Fig. 4.7b with the corresponding shear strains at the tying points γ_{13} and γ_{23} .

$$(4.48) \quad N_A^{13} = \frac{1}{2}(1+s) \quad N_C^{13} = \frac{1}{2}(1-s) \quad N_B^{23} = \frac{1}{2}(1+r) \quad N_D^{23} = \frac{1}{2}(1-r)$$

$$(4.49) \quad \gamma_{13} = N_A^{13} \gamma_{13}^A + N_C^{13} \gamma_{13}^C \quad \gamma_{23} = N_B^{23} \gamma_{23}^B + N_D^{23} \gamma_{23}^D$$

The MITC strain-displacement rows consists of the strain interpolation with the corresponding strain-displacements matrix rows evaluated at the tying points.

$$(4.50) \quad [B_{23}^{MITC}] = N_B^{23} [B_{23}]|_B + N_D^{23} [B_{23}]|_D$$

$$(4.51) \quad [B_{13}^{MITC}] = N_A^{13} [B_{13}]|_A + N_C^{13} [B_{13}]|_C$$

4.3 Constitutive Relations

With the use of Green-Lagrange strain and the 2nd Piola Kirchoff stress tensors in convective terms in Eq. (4.35), the constitutive relation with the constitutive matrix must align with these used, which follows the derivation in Vu-Quoc and Tan (2003).

With the use of laminated composite materials, the constitutive matrix can be expressed through orthotropic material behaviour. Furthermore, the Reissner-Mindlin shell assumption of inextensible transverse normals means a plane strain assumption with $\epsilon_{33} = 0$ is applied. However, this results in transverse normal stresses which are not present in thin shell structures. To mitigate this, a plane stress reduced constitutive relation is applied and is explained in more detail by Jones (1999).

The other assumptions result in transverse shear strains that are allowed to be non-zero, but will be constant in structures. The transverse shear strains will provide piece-wise constant shear stresses, which should be parabolic in flat plates and higher order in double curved shells. The assumptions will thus provide wrong shear strain energy for the system. To correct this behaviour, a shear correction factor κ is multiplied on the transverse shear stiffness C_{55} and C_{66} in the constitutive matrix in material coordinates $[\hat{C}]$. For simplicity and given the shear correction factor is not an area of interest in this thesis, the factor of 5/6 from isotropic materials is used.

$$(4.52) \quad [\hat{C}] = \begin{bmatrix} \frac{E_1}{1-\nu_{12}\nu_{21}} & \frac{\nu_{21}E_1}{1-\nu_{12}\nu_{21}} & 0 & 0 & 0 & 0 \\ & \frac{E_2}{1-\nu_{12}\nu_{21}} & 0 & 0 & 0 & 0 \\ & & 0 & 0 & 0 & 0 \\ & & & G_{12} & 0 & 0 \\ & \text{Sym.} & & & \kappa G_{23} & 0 \\ & & & & & \kappa G_{13} \end{bmatrix}$$

Here, E are the Young's moduli in the respective directions, ν is the Poisson's ratio and G are the respective shear moduli. The constitutive matrix in material coordinates system $\{\{a_1\}, \{a_2\}, \{a_3\}\}$ can be related to a local orthonormal element coordinate system $\{\{d_1\}, \{d_2\}, \{d_3\}\}$ with the fibre orientation θ by

$$(4.53) \quad \{a_1\} = \cos(\theta)\{d_1\} + \sin(\theta)\{d_2\}$$

$$(4.54) \quad \{a_2\} = -\sin(\theta)\{d_1\} + \cos(\theta)\{d_2\}$$

$$(4.55) \quad \{a_3\} = \{d_3\}$$

The local orthonormal element coordinate system is used as a reference system for the lamina orientations with $\{d_1\}$ being the fibre direction when $\theta = 0$, which was illustrated in Fig. 2.11. The system is defined from the normal to the structure surface to ensure fibre directions are tangent to the surface with the exact definition given from the covariant base and $\{G_i\}$ and global Cartesian base $\{e_i\}$.

$$(4.56) \quad \{d_3\} = \frac{\{G_1\} \times \{G_2\}}{\|\{G_1\} \times \{G_2\}\|}$$

$$(4.57) \quad \{d_1\} = \frac{\{e_2\} \times \{d_3\}}{\|\{e_2\} \times \{d_3\}\|}$$

$$(4.58) \quad \{d_2\} = \frac{\{d_3\} \times \{d_1\}}{\|\{d_3\} \times \{d_1\}\|}$$

The constitutive matrix is equal when using the contravariant components $[\tilde{C}]$ in the covariant base $\{G_i\}$ as using the components in the material coordinate system $[\hat{C}]$ with the material coordinate bases $\{a_i\}$.

$$(4.59) \quad [\hat{C}^{abcd}]\{a_a\} \otimes \{a_b\} \otimes \{a_c\} \otimes \{a_d\} = [\tilde{C}^{ijkl}]\{G_i\} \otimes \{G_j\} \otimes \{G_k\} \otimes \{G_l\}$$

Through dot products with the contravariant bases $\{G^i\}$, the contravariant components of constitutive matrix $[C^{ijkl}]$ can be expressed from a transformation of the components in the material coordinate system $[\hat{C}^{abcd}]$.

$$(4.60) \quad [C^{ijkl}] = (\{G^i\} \cdot \{a_a\})(\{G^j\} \cdot \{a_b\})(\{G^k\} \cdot \{a_c\})(\{G^l\} \cdot \{a_d\})[\hat{C}^{abcd}]$$

This may also be expressed in matrix form and also relate the constitutive matrix with the strain definition in Eq. (4.37) with the transformation matrix $[T_G]$.

$$(4.61) \quad [C^{ijkl}] = [T_G]^T[\hat{C}^{abcd}][T_G]$$

The transformation matrix is defined from the inner product between the contravariant and the laminate bases following the transformation matrix presented in Cook et al. (2001).

$$(4.62) \quad t_i^j = \{G^j\} \cdot \{a_i\}$$

$$(4.63) \quad [T_G] = \begin{bmatrix} (t_1^1)^2 & (t_1^2)^2 & (t_1^3)^2 & t_1^1 t_1^2 & t_1^2 t_1^3 & t_1^1 t_1^3 \\ (t_2^1)^2 & (t_2^2)^2 & (t_2^3)^2 & t_2^1 t_2^2 & t_2^2 t_2^3 & t_2^1 t_2^3 \\ (t_3^1)^2 & (t_3^2)^2 & (t_3^3)^2 & t_3^1 t_3^2 & t_3^2 t_3^3 & t_3^1 t_3^3 \\ 2t_1^1 t_1^2 & 2t_1^2 t_1^2 & 2t_1^3 t_1^2 & t_1^1 t_2^2 + t_1^2 t_1^2 & t_1^2 t_2^3 + t_2^2 t_1^3 & t_1^1 t_2^3 + t_2^2 t_1^3 \\ 2t_2^1 t_1^3 & 2t_2^2 t_2^3 & 2t_2^3 t_2^3 & t_2^1 t_2^3 + t_3^1 t_2^2 & t_2^2 t_3^3 + t_3^2 t_2^3 & t_2^1 t_3^3 + t_3^1 t_2^3 \\ 2t_1^1 t_1^3 & 2t_1^2 t_1^3 & 2t_1^3 t_1^3 & t_1^1 t_3^2 + t_3^1 t_1^2 & t_1^2 t_3^3 + t_3^2 t_1^3 & t_1^1 t_3^3 + t_3^1 t_1^3 \end{bmatrix}$$

4.4 Derivation of Governing FE Equations

The shell assumptions has led to the strain-displacement and constitutive relations needed to apply FEA with a 4-node shell element. These definitions from the earlier sections are used in the general governing FE equations derived in this section with stabilisation from the EAS method.

The tangent stiffness matrix follows from the derivation of the governing FE equations for non-linear FE problems. The derivation takes offset in the arbitrary continuum body illustrated in Fig. 4.8 for which Washizu (1975) uses the total elastic potential Π to describe the total potential

work from all forces involved and derive the deformation state. These include the energy stored in the body $W(\varepsilon_{ij})$, body forces B_i and boundary conditions imposed by prescribed tractions T_i or displacements u_i .

$$(4.64) \quad \Pi = \int_V W(\varepsilon_{ij})dV - \int_V B_i u_i dV - \int_S T_i u_i dS$$

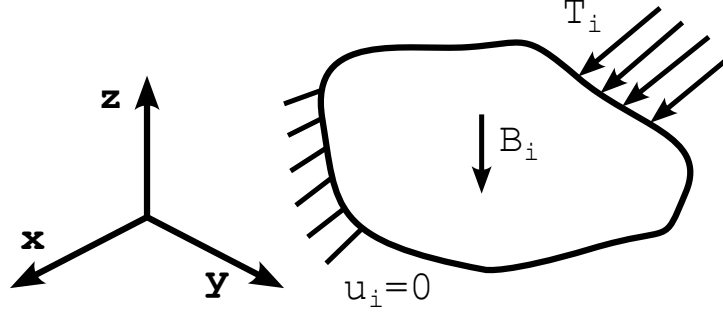


Figure 4.8. Arbitrary 2D continuum body with boundary conditions imposed through prescribed displacements u_i and tractions T_i . The body forces are denoted by B_i .

4.4.1 First Variation in Total Elastic Potential with EAS

Washizu (1975) generalised the expression for the total elastic potential by enforcing strain compatibility conditions and boundary conditions using Lagrange multipliers σ_{ij} . In a FE context it is only necessary to enforce the strain compatibility, since the boundary conditions are enforced by prescribing nodal DOFs. The strain compatibility is enforced in the second term of Eq. (4.65) by ensuring any difference in the strain field ε_{ij} compared with a compatible strain definition ε_{ij}^c does not contribute to the total elastic potential.

$$(4.65) \quad \Pi = \int_V W(\varepsilon_{ij})dV - \int_V (\varepsilon_{ij} - \varepsilon_{ij}^c)\sigma_{ij}dV - \int_V B_i u_i dV - \int_S T_i u_i dS$$

This expression is used by Washizu (1975) to drive the strain field to be equal to the compatible strain field. However, Simo and Rifai (1990) instead introduces enhanced strains,

$$(4.66) \quad \varepsilon_{ij}^e = \varepsilon_{ij} - \varepsilon_{ij}^c$$

as part of the EAS method that is used to mitigate shear locking problems and stabilise the element. Shear locking occurs due to an inability of low-order elements to represent pure bending and is explained in more detail by Cook et al. (2001). For the 4-node shell element used in this thesis, the EAS method is used for in-plane shear locking and the MITC method is used for out-of-plane shear locking.

With the enhanced strain definition from Simo and Rifai (1990), the total elastic potential presented by Washizu (1975) can be expressed as a three-field variational functional $\Pi(u_i, \varepsilon_{ij}^e, \sigma_{ij})$.

$$(4.67) \quad \Pi(u_i, \varepsilon_{ij}^e, \sigma_{ij}) = \int_V W(\varepsilon_{ij}^c + \varepsilon_{ij}^e)dV - \int_V \varepsilon_{ij}^e \sigma_{ij} dV - \int_V B_i u_i dV - \int_S T_i u_i dS$$

The total elastic potential is useful for determining the deformation state, since the minimum total elastic potential describes the stationary deformation state. Stationarity in a multi-field functional is found by taking the first variation of the functional as the sum of the first variation with respect to each independent field $(u_i, \varepsilon_{ij}^e, \sigma_{ij})$ and equating the expression to 0.

$$(4.68) \quad \delta\Pi(u_i, \varepsilon_{ij}^e, \sigma_{ij}) = \delta_{u_i}\Pi(u_i, \varepsilon_{ij}^e, \sigma_{ij}) + \delta_{\varepsilon_{ij}}\Pi(u_i, \varepsilon_{ij}^e, \sigma_{ij}) + \delta_{\sigma_{ij}}\Pi(u_i, \varepsilon_{ij}^e, \sigma_{ij}) = 0$$

This follows the variational principles described by Dym and Shames (2013) resulting in the three-field variational problem that is solved to obtain the stationary deformation state. Since the three fields are independent each term should also be 0 individually.

$$(4.69) \quad \delta_{u_i}\Pi(u_i, \varepsilon_{ij}^e, \sigma_{ij}) = \int_V \frac{\partial W}{\partial \varepsilon_{ij}^e} \delta \varepsilon_{ij}^e dV - \int_V B_i \delta u_i dV - \int_S T_i \delta u_i dS = 0$$

$$(4.70) \quad \delta_{\varepsilon_{ij}}\Pi(u_i, \varepsilon_{ij}^e, \sigma_{ij}) = \int_V \left(\frac{\partial W}{\partial \varepsilon_{ij}^e} - \sigma_{ij} \right) \delta \varepsilon_{ij}^e dV = 0$$

$$(4.71) \quad \delta_{\sigma_{ij}}\Pi(u_i, \varepsilon_{ij}^e, \sigma_{ij}) = \int_V \varepsilon_{ij}^e \delta \sigma_{ij} dV = 0$$

In the notation, a preceding δ denotes the first variation with the subscript detailing which field is varied. $\delta_{u_i}\Pi$ is thus to be understood as the first variation of the total elastic potential Π with respect to the displacement field u_i . It is worth noting that $\delta \varepsilon_{ij}^e$ is present since the compatible strains are dependent on the displacements $\varepsilon_{ij}^e(u_i)$.

Fundamental to the Lagrange multiplier method is the addition of a term which should equate to zero and the use of Lagrange multipliers to enforce this. The following is therefore required for any variations in either enhanced strains or the Lagrange multipliers.

$$(4.72) \quad \int_V \varepsilon_{ij}^e \sigma_{ij} dV = 0$$

This is also the orthogonality condition introduced by Simo and Rifai (1990). The Lagrange multipliers act as internal forces to enforce compatibility, meaning they express the stress in the structure. Multiplying the stresses with the strains expresses the work done by the internal forces. The orthogonality condition can thus be understood as a requirement that the enhanced strains should not contribute any work to the total elastic potential. The condition is convenient since it reduces the three-field variational problem to only contain two fields, displacements u_i and enhanced strains ε_{ij}^e .

$$(4.73) \quad \delta\Pi(u_i, \varepsilon_{ij}^e) = \delta_{u_i}\Pi(u_i, \varepsilon_{ij}^e) + \delta_{\varepsilon_{ij}}\Pi(u_i, \varepsilon_{ij}^e) = 0$$

$$(4.74) \quad \delta_{u_i}\Pi(u_i, \varepsilon_{ij}^e) = \int_V \frac{\partial W}{\partial \varepsilon_{ij}^e} \delta \varepsilon_{ij}^e dV - \int_V B_i \delta u_i dV - \int_S T_i \delta u_i dS = 0$$

$$(4.75) \quad \delta_{\varepsilon_{ij}}\Pi(u_i, \varepsilon_{ij}^e) = \int_V \frac{\partial W}{\partial \varepsilon_{ij}^e} \delta \varepsilon_{ij}^e dV = 0$$

The resulting two equations can be interpreted as Eq. (4.74) describing equilibrium between work done by external and internal forces over arbitrary variations in displacements, while Eq. (4.75) ensures the enhanced strains does not contribute to the internal forces.

4.4.2 Linearisation of Governing Equations

In order to solve the governing equations, non-linear solvers use linearisation of the governing equations and solves the linear equations iteratively for the iterations k . The linearisation is made by performing a first order Taylor series expansion of Eq. (4.73) and equating it to 0. The Taylor series expansion introduces increments in the DOFs, which are denoted by Δ and are different from the variations denoted by δ . The increments are quantifiable changes to the displacements and enhanced strains, while the variations are arbitrary changes to the displacements and enhanced strains.

$$(4.76) \quad 0 = \delta\Pi({}_{(k+1)}u_i, {}_{(k+1)}\varepsilon_{ij}^e) = \delta\Pi({}_{(k)}u_i, {}_{(k)}\varepsilon_{ij}^e) + \left. \frac{\partial\delta\Pi(u_i, \varepsilon_{ij}^e)}{\partial(u_i, \varepsilon_{ij}^e)} \right|_{u_i={}_{(k)}u_i, \varepsilon_{ij}^e={}_{(k)}\varepsilon_{ij}^e} (\Delta u_i, \Delta \varepsilon_{ij}^e)$$

Inserting known values of displacements ${}_{(k)}u_i$ and enhanced strains ${}_{(k)}\varepsilon_{ij}^e$ at iteration k allows for the calculation of increments Δu_i and $\Delta \varepsilon_{ij}^e$. Adding these increments to ${}_{(k)}u_i$ and ${}_{(k)}\varepsilon_{ij}^e$ results in displacements ${}_{(k+1)}u_i$ and enhanced strains ${}_{(k+1)}\varepsilon_{ij}^e$ that will more closely approximate the solution to Eq. (4.73).

$$(4.77) \quad {}_{(k+1)}u_i = {}_{(k)}u_i + \Delta u_i$$

$$(4.78) \quad {}_{(k+1)}\varepsilon_{ij}^e = {}_{(k)}\varepsilon_{ij}^e + \Delta \varepsilon_{ij}^e$$

The updated approximation of displacements and enhanced strains is then used to calculate new increments and an even closer approximation in an iterative procedure converging towards the solution of the non-linear problem in Eq. (4.73). The procedure explained here is more commonly known as the Newton-Raphson method (Cook et al., 2001).

Inserting the expression for $\delta\Pi$ as given by Eq. (4.73), (4.74) and (4.75) into Eq. (4.76) yields the following linearised governing equation. The subscripted k denoting iteration is omitted in the following, since all displacements and enhanced strains are at iteration k (Klinkel et al., 1999; Vu-Quoc and Tan, 2003).

$$(4.79) \quad \begin{aligned} 0 = & \int_V \frac{\partial W}{\partial \varepsilon_{ij}^c} \delta \varepsilon_{ij}^c dV - \int_V B_i \delta u_i dV - \int_S T_i \delta u_i dS \\ & + \int_V \left(\frac{\partial^2 W}{\partial \varepsilon_{ij}^c \partial \varepsilon_{kl}^c} \delta \varepsilon_{ij}^c \Delta \varepsilon_{kl}^c + \frac{\partial W}{\partial \varepsilon_{ij}^c} (\Delta \delta \varepsilon_{ij}^c) \right) dV + \int_V \frac{\partial^2 W}{\partial \varepsilon_{ij}^c \partial \varepsilon_{kl}^e} \delta \varepsilon_{ij}^c \Delta \varepsilon_{kl}^e dV \\ & + \int_V \frac{\partial W}{\partial \varepsilon_{ij}^e} \delta \varepsilon_{ij}^e dV + \int_V \frac{\partial^2 W}{\partial \varepsilon_{ij}^e \partial \varepsilon_{kl}^e} \delta \varepsilon_{ij}^e \Delta \varepsilon_{kl}^e dV + \int_V \frac{\partial^2 W}{\partial \varepsilon_{ij}^e \partial \varepsilon_{kl}^c} \delta \varepsilon_{ij}^e \Delta \varepsilon_{kl}^c dV \end{aligned}$$

In deriving the expression above, δu_i is an independent and arbitrary variation in u_i . As such, the derivative of δu_i with respect to u_i evaluates to 0. The same applies to the enhanced strains. However, the compatible strains are a function of displacements, meaning the variation in compatible strains ε_{ij}^c is dependent on the displacements. For now this is defined with the following notation.

$$(4.80) \quad \frac{d(\delta u_i)}{du_i} \Delta u_i = 0 \quad \frac{d(\delta \varepsilon_{ij}^e)}{d\varepsilon_{ij}^e} \Delta \varepsilon_{ij}^e = 0 \quad \frac{d(\delta \varepsilon_{ij}^c)}{du_i} \Delta u_i = \Delta \delta \varepsilon_{ij}^c$$

Thus the term in the parentheses of Eq. (4.79) emanates from the use of the product rule, when differentiating the first term in Eq. (4.74) with respect to the displacements.

Using the Euler equation emanating from Eq. (4.70), the stored energy function W can be related to the stresses σ_{ij} which can be expressed by the constitutive relation with the constitutive tensor and strains. It is worth noting that these stresses are dependent on the strains unlike the Lagrange multipliers used previously (Klinkel et al., 1999; Vu-Quoc and Tan, 2003).

$$(4.81) \quad \sigma_{ij} = \frac{\partial W}{\partial \varepsilon_{ij}} = C_{ijkl} \varepsilon_{kl}$$

From the above the following is true of the constitutive tensor.

$$(4.82) \quad C_{ijkl} = \frac{\partial^2 W}{\partial \varepsilon_{ij} \partial \varepsilon_{kl}}$$

The constitutive expressions can be inserted into the linearised governing equation in Eq. (4.79). Since the displacement and enhanced strain fields are independent, the equation can be split into the variations with respect to each field, which must equal 0 on its own.

$$(4.83) \quad 0 = \int_V \sigma_{ij} \delta \varepsilon_{ij}^c dV - \int_V B_i \delta u_i dV - \int_S T_i \delta u_i dS$$

$$+ \int_V (C_{ijkl} \delta \varepsilon_{ij}^c \Delta \varepsilon_{kl}^c + \sigma_{ij} (\Delta \delta \varepsilon_{ij}^c)) dV + \int_V C_{ijkl} \delta \varepsilon_{ij}^c \Delta \varepsilon_{kl}^e dV$$

$$(4.84) \quad 0 = \int_V \sigma_{ij} \delta \varepsilon_{ij}^e dV + \int_V C_{ijkl} \delta \varepsilon_{ij}^e \Delta \varepsilon_{ij}^c dV + \int_V C_{ijkl} \delta \varepsilon_{ij}^e \Delta \varepsilon_{kl}^e dV$$

4.4.3 Interpolation of Governing Equations

The linearised governing equations in Eq. (4.83) and (4.84) need to be expressed in terms of the DOFs. For this to be done, the equations are first rewritten in matrix-vector form.

$$(4.85) \quad 0 = \int_V \delta \{\varepsilon^c\}^T \{\sigma\} dV - \int_V \delta \{u\}^T \{B\} dV - \int_S \delta \{u\}^T \{T\} dS$$

$$+ \int_V (\delta \{\varepsilon^c\}^T [C] \Delta \{\varepsilon^c\} + (\Delta \delta \{\varepsilon^c\})^T \{\sigma\}) dV + \int_V \delta \{\varepsilon^c\}^T [C] \Delta \{\varepsilon^e\} dV$$

$$(4.86) \quad 0 = \int_V \delta \{\varepsilon^e\}^T \{\sigma\} dV + \int_V \delta \{\varepsilon^e\}^T [C] \Delta \{\varepsilon^c\} dV + \int_V \delta \{\varepsilon^e\}^T [C] \Delta \{\varepsilon^e\} dV$$

The equations are expressed in terms of the DOFs by using the interpolations derived in section 4.1.3, 4.2.3 and 4.4.4 respectively for the 4-node shell element with the general forms repeated below.

$$(4.87) \quad \{u\} = [N] \{d\}$$

$$(4.88) \quad \{\varepsilon^e\} = [\tilde{M}] \{\alpha\}$$

In terms of the compatible strains, the interpolations are defined based on the relationship between increments in strains and nodal DOFs. The variations and increments denoted by the δ and Δ operators respectively, pertains to the variables, which are the DOFs.

$$(4.89) \quad \delta \{u\} = [N] \delta \{d\} \quad \Delta \{u\} = [N] \Delta \{d\}$$

$$(4.90) \quad \delta \{\varepsilon^e\} = [B] \delta \{d\} \quad \Delta \{\varepsilon^e\} = [B] \Delta \{d\}$$

$$(4.91) \quad \delta \{\varepsilon^e\} = [\tilde{M}] \delta \{\alpha\} \quad \Delta \{\varepsilon^e\} = [\tilde{M}] \Delta \{\alpha\}$$

The increment in the variation of compatible strains $\Delta\delta\{\varepsilon^c\}$ defined in Eq. (4.80) can be expanded with the interpolations.

$$(4.92) \quad \Delta\delta\{\varepsilon^c\} = \frac{d(\delta\{\varepsilon^c\})}{d\{d\}} \Delta\{d\} = \delta\{d\}^T \frac{d[B]^T}{d\{d\}} \Delta\{d\}$$

The interpolations of displacements and strains can be inserted in the governing equations Eq. (4.85) and (4.86) to yield the interpolated governing equations.

$$(4.93) \quad 0 = \int_V \delta\{d\}^T [B]^T \{\sigma\} dV - \int_V \delta\{d\}^T [N]^T \{B\} dV - \int_S \delta\{d\}^T [N]^T \{T\} dS \\ + \int_V \left(\delta\{d\}^T [B]^T [C] [B] \Delta\{d\} + \delta\{d\}^T \frac{d[B]^T}{d\{d\}} \{\sigma\} \Delta\{d\} \right) dV$$

$$(4.94) \quad + \int_V \delta\{d\}^T [B]^T [C] [\tilde{M}] \Delta\{\alpha\} dV \\ 0 = \int_V \delta\{\alpha\}^T [\tilde{M}]^T \{\sigma\} dV + \int_V \delta\{\alpha\}^T [\tilde{M}]^T [C] [B] \Delta\{d\} dV \\ + \int_V \delta\{\alpha\}^T [\tilde{M}]^T [C] [\tilde{M}] \Delta\{\alpha\} dV$$

By applying the basic concept of variational methods that the equations must hold for arbitrary variations $\delta\{d\}$ and $\delta\{\alpha\}$, the following must hold (Vu-Quoc and Tan, 2003; Dym and Shames, 2013).

$$(4.95) \quad \{0\} = \int_V [B]^T \{\sigma\} dV - \int_V [N]^T \{B\} dV - \int_S [N]^T \{T\} dS \\ + \int_V \left([B]^T [C] [B] \Delta\{d\} + \frac{d[B]^T}{d\{d\}} \{\sigma\} \Delta\{d\} \right) dV + \int_V [B]^T [C] [\tilde{M}] \Delta\{\alpha\} dV$$

$$(4.96) \quad \{0\} = \int_V [\tilde{M}]^T \{\sigma\} dV + \int_V [\tilde{M}]^T [C] [B] \Delta\{d\} dV + \int_V [\tilde{M}]^T [C] [\tilde{M}] \Delta\{\alpha\} dV$$

These equations can be rearranged to yield a set of linear algebraic equations that can be solved for the increments $\Delta\{d\}$ and $\Delta\{\alpha\}$.

$$(4.97) \quad \begin{bmatrix} [k_{uu}] & [k_{u\alpha}] \\ [k_{\alpha u}] & [k_{\alpha\alpha}] \end{bmatrix} \begin{Bmatrix} \Delta\{d\} \\ \Delta\{\alpha\} \end{Bmatrix} = - \begin{Bmatrix} \{f_{int}\} - \{f_{ext}\} \\ \{f_{eas}\} \end{Bmatrix}$$

Here the stiffness matrices are given by

$$(4.98) \quad [k_{uu}] = \int_V \left([B]^T [C] [B] + \frac{d[B]^T}{d\{d\}} \{\sigma\} \right) dV$$

$$(4.99) \quad [k_{u\alpha}] = [k_{\alpha u}]^T = \int_V [B]^T [C] [\tilde{M}] dV$$

$$(4.100) \quad [k_{\alpha u}] = [k_{u\alpha}]^T = \int_V [\tilde{M}]^T [C] [B] dV$$

$$(4.101) \quad [k_{\alpha\alpha}] = \int_V [\tilde{M}]^T [C] [\tilde{M}] dV$$

and the forces are designated as external $\{f_{ext}\}$, internal $\{f_{int}\}$ and EAS related $\{f_{eas}\}$.

$$(4.102) \quad \{f_{ext}\} = \int_V [N]^T \{B\} dV + \int_S [N]^T \{T\} dS$$

$$(4.103) \quad \{f_{int}\} = \int_V [B]^T \{\sigma\} dV$$

$$(4.104) \quad \{f_{eas}\} = \int_V [\tilde{M}]^T \{\sigma\} dV$$

Since the enhanced strains were included as independent and the internal DOFs are not required to be continuous across elements, the linear system of equations can be reduced using static condensation (Simo and Rifai, 1990). This results in the following set of equations also found in Vu-Quoc and Tan (2003).

$$(4.105) \quad [k_T] \Delta\{d\} = -\{r\}$$

The tangent stiffness matrix $[k_T]$ and residual force vector $\{r\}$ for the element can be derived from the set of linear algebraic equations in Eq. (4.97) by expressing the increment in internal DOFs $\Delta\{\alpha\}$ from the increment in nodal DOFs $\Delta\{d\}$.

$$(4.106) \quad \Delta\{\alpha\} = -[k_{\alpha\alpha}]^{-1}(\{f_{eas}\} + [k_{\alpha u}] \Delta\{d\})$$

$$(4.107) \quad [k_T] = [k_{uu}] - [k_{\alpha u}]^T [k_{\alpha\alpha}]^{-1} [k_{\alpha u}]$$

$$(4.108) \quad \{r\} = \{f_{int}\} - [k_{\alpha u}]^T [k_{\alpha\alpha}]^{-1} \{f_{eas}\} - \{f_{ext}\}$$

The governing equations and the expressions presented throughout the derivation of the governing equations in this section are general for any type of element modelled using FE with the EAS method. The equations derived here are the same as those derived in Klinkel and Wagner (1997), Klinkel et al. (1999) and Vu-Quoc and Tan (2003) for the non-linear 8-node solid and solid-shell formulations with EAS. This is due to the specifics of the chosen element being implemented through the definition of the interpolations presented in section 4.1.3, 4.2.3 and 4.4.4. Furthermore, the governing equations allow for the displacements, strains and other parameters to be expressed in any base as long as the bases used are consistent. It is implied by the dependency of the strain displacement relationship $[B]$ on the nodal DOFs $\{d\}$ that the Green-Lagrange strains are used. However, this is not strictly necessary and using Cauchy strains will simply make the problem linear with the use of the total Lagrangian formulation and thus only require one iteration to find a solution. In terms of the stress and strain definitions, it is important that the relationship is described by Eq. (4.81) to be work consistent.

4.4.4 Enhanced Strain Interpolation

The enhanced strain interpolation is derived for the EAS formulation by Simo and Rifai (1990) from the incompatible modes element presented by Wilson et al. (1973). The interpolation is between internal DOFs $\{\alpha\}$ using an interpolation matrix $[M]$ to obtain the covariant enhanced strain components $\{E^e\}$ in the contravariant base at the element centre $\{G_i(0)\}$.

$$(4.109) \quad \{E_{kl}^e\} \{G^k(0)\} \otimes \{G^l(0)\} = [M] \{\alpha\} \{G^k(0)\} \otimes \{G^l(0)\}$$

The interpolation matrix $[M]$ is given by the following as derived by Simo and Rifai (1990).

$$(4.110) \quad [M] = \begin{bmatrix} r & 0 & 0 & 0 \\ 0 & s & 0 & 0 \\ 0 & 0 & 0 & 0 \\ 0 & 0 & r & s \\ 0 & 0 & 0 & 0 \\ 0 & 0 & 0 & 0 \\ 0 & 0 & 0 & 0 \end{bmatrix}$$

In order for the enhanced strain interpolation to be applied, the base must be consistent with those used for the compatible Green-Lagrange strains. These are expressed using the covariant components $\{\tilde{E}^e\}$ in the contravariant base $\{G^i(r_i)\}$, which is not explicitly evaluated in the element centre. The interpolated enhanced strains are obtained in the correct base through a basis transformation as described by Vu-Quoc and Tan (2003).

$$(4.111) \quad \{\tilde{E}_{ij}^e\}\{G^i(r_i)\} \otimes \{G^j(r_i)\} = \{E_{kl}^e\}\{G^k(0)\} \otimes \{G^l(0)\} = [M]\{\alpha\}\{G^k(0)\} \otimes \{G^l(0)\}$$

$$(4.112) \quad \{\tilde{E}_{ij}^e\} = (\{G_i(r_i)\} \cdot \{G^k(0)\})(\{G^l(0)\} \cdot \{G_j(r_i)\})\{E_{ij}^e\} = [T_0][M]\{\alpha\}$$

$$(4.113) \quad [T_0] = (\{G_i(r_i)\} \cdot \{G^k(0)\})(\{G^l(0)\} \cdot \{G_j(r_i)\})$$

The transformation matrix is obtained by Eq. (4.62) and (4.63), which can be derived from the transformation of the strain vector as described above and in Cook et al. (2001). For the strain interpolation, the covariant strain components $\{\tilde{E}_{ij}^e\}$ are needed and these can be described from the internal DOFs $\{\alpha\}$ by the transformed enhanced strain interpolation matrix.

$$(4.114) \quad \{\tilde{E}_{ij}^e\} = [T_0][M]\{\alpha\} = [\tilde{M}]\{\alpha\}$$

4.5 Numerical Integration of Governing Equations

By introducing the interpolations, the governing equations have been expressed in terms of nodal DOFs. However, the volume integrals in each stiffness matrix need to be solved. Generally, these integrals are solved numerically using Gauss quadrature as explained by Cook et al. (2001).

Gauss quadrature approximates the integral by a weighted sum of the integrand evaluated at specific points. These points are most easily specified using the natural coordinates (r, s, t) . Therefore, the integral is converted to the natural coordinates using the Jacobian determinant $|J|$ as exemplified for $[k_{uu}]$.

$$(4.115) \quad \begin{aligned} [k_{uu}] &= \int_V \left([B]^T [C] [B] + \frac{d[B]^T}{d\{d\}} \{\sigma\} \right) dV \\ &= \int_{-1}^1 \int_{-1}^1 \int_{-1}^1 \left([B]^T [C] [B] + \frac{d[B]^T}{d\{d\}} \{\sigma\} \right) |J| dr ds dt \end{aligned}$$

For the other stiffness matrices $[k_{u\alpha}]$, $[k_{\alpha u}]$, $[k_{\alpha\alpha}]$, a similar procedure applies. However, as explained by Taylor et al. (1986) and Simo and Rifai (1990) it is necessary to pass the patch test to ensure convergence of the element when the EAS method is applied. Passing the patch test can be ensured by conversions of the volume integrals to the natural coordinates following

those presented in Vu-Quoc and Tan (2003).

$$(4.116) \quad [k_{\alpha u}] = [k_{u\alpha}]^T = \int_V [\tilde{M}]^T [C] [B] dV \approx \int_{-1}^1 \int_{-1}^1 \int_{-1}^1 [\tilde{M}]^T [C] [B] dr ds dt$$

$$(4.117) \quad [k_{\alpha\alpha}] = \int_V [\tilde{M}]^T [C] [\tilde{M}] dV \approx \int_{-1}^1 \int_{-1}^1 \int_{-1}^1 [\tilde{M}]^T [C] [\tilde{M}] \frac{1}{|J|} dr ds dt$$

After the appropriate conversions of the integrals to the natural coordinates, the integrals are then evaluated as a weighted sum of the integrand in specific points, as illustrated in Fig. 4.9 and exemplified with $[k_{uu}]$.

$$(4.118) \quad [k_{uu}] = \sum_{i=1}^2 \sum_{j=1}^2 \sum_{k=1}^2 w_i w_j w_k \phi(r_{ijk}, s_{ijk}, t_{ijk})$$

$$(4.119) \quad \phi(r, s, t) = [B(r, s, t)]^T [C(r, s, t)] [B(r, s, t)] |J(r, s, t)|$$

$$(4.120) \quad w_i, w_j, w_k = 1 \quad , \quad r, s, t = \pm \frac{1}{\sqrt{3}}$$

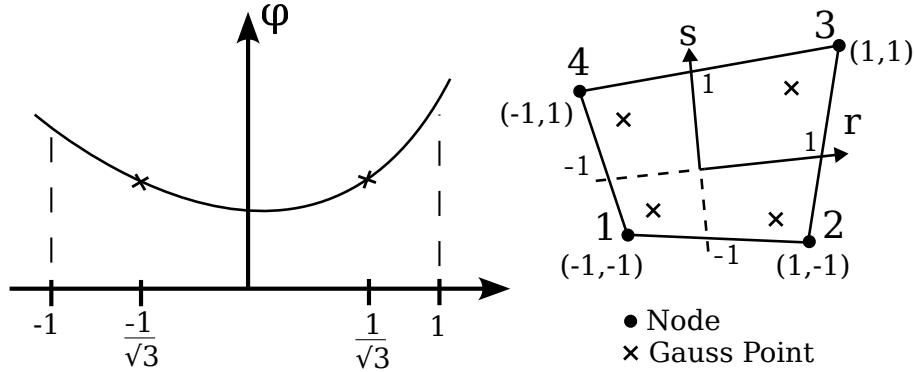


Figure 4.9. Gauss quadrature exemplified with a 1D curve on the left and location in natural coordinates of in-plane Gauss points for full integration in a 4-node shell element on the right.

The number of points and value of weights used for the integrations correspond to a full integration, as the integration order needed for exact evaluation of rectangular elements. Higher integration orders are typically not used for computational efficiency and lower integration orders are not used here to avoid spurious modes. For more detail on the concept of numerical integration order in FE, the authors will refer to Cook et al. (2001).

If the shell element is used to model laminates as it is intended in this thesis, considerations must be made towards how the influence of each lamina is taken into account. Here an equivalent single layer approach is used and the effects of each lamina will be included in the integration through the thickness (Jones, 1999). By applying the Gauss quadrature at each lamina of the laminate, the stiffness contribution from each lamina can be included as illustrated by Fig. 4.10. This is done by scaling the stiffness from the Gauss quadrature of each lamina to the relative height of the lamina compared with the laminate. The scaled stiffness of each lamina are then summed. To keep the limits on the integrals at ± 1 , a lamina thickness variable t_l is used, which goes from -1 to 1 within each lamina. To evaluate the integrands at the correct thickness position, the lamina thickness variable t_l is related to the natural thickness coordinate t . This

is expressed in the equation below, where N_{lamina} is the number of laminae and h is the height of the laminate with the subscript denoting the height of a specific lamina.

$$(4.121) \quad [k_{uu}] = \sum_{l=1}^{N_{lamina}} \sum_{i=1}^2 \sum_{j=1}^2 \sum_{k=1}^2 w_i w_j w_k \phi(r_{ijk}, s_{ijk}, t_{ijk}) \frac{h_l}{h}$$

$$(4.122) \quad \phi(r, s, t) = [B(r, s, t)]^T [C(r, s, t)] [B(r, s, t)] J(r, s, t)$$

$$(4.123) \quad w_i, w_j, w_k = 1 \quad , \quad r, s, t_l = \pm \frac{1}{\sqrt{3}}$$

$$(4.124) \quad t = -1 + \frac{1}{h} \left(2 \sum_{i=1}^l h_i - h_l (1 - t_l) \right)$$

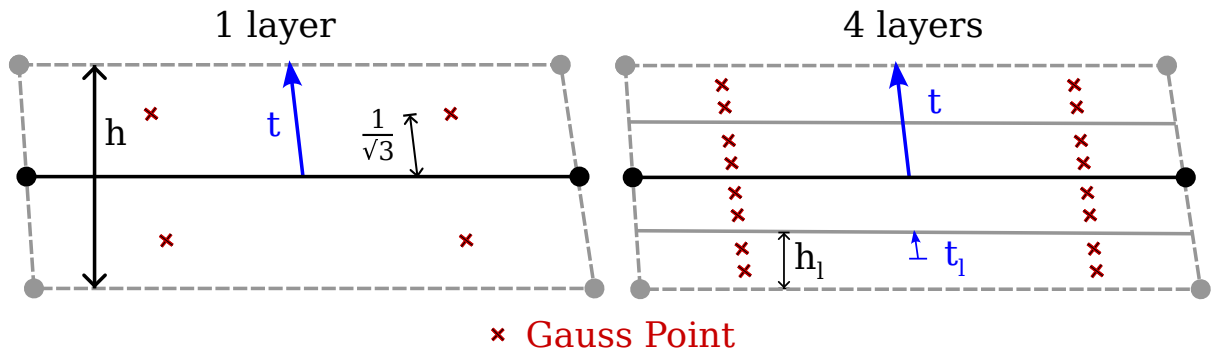


Figure 4.10. Definitions of variables and location of points through the thickness in a Gauss quadrature of a one layer laminate and a multi-layer laminate.

4.6 Linearised Buckling Analysis

The buckling analysis is a stability analysis with the intent to find the critical loads that causes instability through compressive membrane loads. This type of behaviour is most accurately modelled with a non-linear element such as the shell element derived in this chapter, in FEAs with large displacements. However, a linearised buckling analysis provides a much more computationally efficient alternative, in situations where a lower accuracy can be accepted. Thus linearised buckling analyses can allow for efficient optimisation with regards to stability in the early design phase.

The linearised buckling analysis is conducted with the incremental equilibrium equation in Eq. (4.105). Given the linearisation, only the linear part of the strain-displacement matrix $[B_0]$ is used.

$$(4.125) \quad [k_T] \Delta \{d\} = -\{r\}$$

$$(4.126) \quad ([k_{uu}] - [k_{\alpha u}]^T [k_{\alpha \alpha}]^{-1} [k_{\alpha u}]) \Delta \{d\} = -\{r\}$$

Acknowledging the two terms in $[k_{uu}]$ from Eq. (4.98), the tangent stiffness matrix $[k_T]$ can be split into two parts, a stabilised linear part $[k_0]$ and a stress stiffening part $[k_\sigma]$. Since it is the appearance of instability that is analysed, large displacements can be neglected, which is the

reason only the linear and stress stiffening parts are present.

$$(4.127) \quad [k_T] = [k_0] + [k_\sigma]$$

$$(4.128) \quad [k_0] = \int_V [B_0]^T [C] [B_0] dV - [k_{\alpha u}]^T [k_{\alpha\alpha}]^{-1} [k_{\alpha u}]$$

$$(4.129) \quad [k_\sigma] = \int_V \frac{d[B]^T}{d\{d\}} \{\sigma\} dV$$

$$(4.130) \quad ([k_0] + [k_\sigma]) \Delta\{d\} = -\{r\}$$

From the linearised incremental equilibrium equation used for linearised buckling analysis, the well known linear Euler stability problem can be derived as presented in Cook et al. (2001). This results in the following eigenvalue problem, which can be solved for the eigenvalues λ and eigenmodes $\delta\{d\}$ as buckling displacements illustrated in Fig. 4.11.

$$(4.131) \quad ([K_0] + \lambda[K_\sigma])\{\delta D\} = \{0\}$$

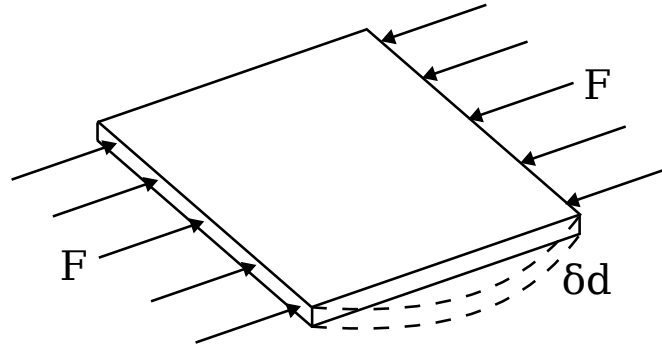


Figure 4.11. Compressive membrane forces F on thin plate that will experience buckling deformations $\delta\{d\}$ at critical values $\lambda_{crit}F$.

The critical force may be determined from a reference force $\{F_{ref}\}$ used to determine $\{\sigma\}$ in the analysis and the critical eigenvalue λ_{crit} as

$$(4.132) \quad \{F_{crit}\} = \lambda_{crit}\{F_{ref}\}$$

In order to perform a linear buckling analysis the procedure used is:

1. Complete a linear static analysis to compute the stresses, strains and the linear stiffness matrix.
2. From the stresses, the stiffness term with the stresses $\{\sigma\}$ in Eq. (4.131) is then computed.
3. Solve the eigenvalue problem from Eq. (4.131) to achieve critical loads and deformation modes.

Drilling Degree of Freedom 5

It was established in section 2.3.3 that the inclusion of a drilling DOF in shell elements based on the 5 DOF approach by Ahmad et al. (1970) is necessary. This is mainly to allow for definition of boundary conditions in a global coordinate system rather than the individual director coordinate systems defined at each node as explained in section 4.1.2. Both the commercial elements from Abaqus and ANSYS have included the drilling DOF in their respective formulations, however the methods used are either undisclosed or not very well described. Therefore, this chapter aims to provide knowledge on the topic as well as propose a generally available method for including the drilling DOF, as this is something the authors have been missing during the implementation of both the linear and non-linear stabilised 4-node shell element.

This chapter will describe the inclusion of a drilling DOF through an expansion of the element stiffness matrix with the addition of a fictitious penalty stiffness. With the implementation explained, a number of tests using the stabilised 4-node shell element from ANSYS Inc. (2018), will be performed and analysed to determine the effect of varying the penalty stiffness. Based on these analyses, a method for including the drilling DOF is proposed and subsequently tested to learn more about the drilling DOF inclusion.

5.1 Inclusion of the Drilling DOF

The inclusion of drilling through a penalty stiffness takes offset in the set of linear algebraic equations solved in FEAs given by Eq. (4.105) for a non-linear 4-node shell element repeated in Eq. (5.1). This equation describes the relationship between the DOFs in a node and corresponding loads in a node, given by the three translations with three corresponding forces and two rotations with two corresponding moments as illustrated by blue arrows in Fig. 2.9.

For the linear 4-node shell element the same principles apply in regards to the inclusion of drilling by expanding the element stiffness matrix. Therefore Δ denoting the increment is omitted in the following. Along with an expansion of the element stiffness matrix, a transformation is also necessary to obtain rotations in the global coordinate system and allow for boundary conditions to be applied to rotations around the axes of the global coordinate system.

5.1.1 Expansion of Stiffness Matrix

The element stiffness matrix expressed in Eq. (4.107) can be ordered in blocks $[k]_{lm}$ that express the stiffness between DOFs $\{d\}_m$ in node m and the loads $\{r\}_l$ in node l .

$$(5.1) \quad [k_T]\{d\} = -\{r\}$$

$$(5.2) \quad \begin{bmatrix} [k]_{11} & [k]_{12} & [k]_{13} & [k]_{14} \\ [k]_{21} & [k]_{22} & [k]_{23} & [k]_{24} \\ [k]_{31} & [k]_{32} & [k]_{33} & [k]_{34} \\ [k]_{41} & [k]_{42} & [k]_{43} & [k]_{44} \end{bmatrix} \begin{Bmatrix} \{d\}_1 \\ \{d\}_2 \\ \{d\}_3 \\ \{d\}_4 \end{Bmatrix} = - \begin{Bmatrix} \{r\}_1 \\ \{r\}_2 \\ \{r\}_3 \\ \{r\}_4 \end{Bmatrix}$$

Each block $[k]_{lm}$ is a 5×5 matrix for the 5 DOF shell element with individual scalar components k_{ij} describing the stiffness relation between the DOF denoted by i in node m and the load denoted by j in node l . The relation between loads $\{r_u, r_v, r_w, r_\alpha, r_\beta\}_l$ at node l and DOFs $\{u, v, w, \alpha, \beta\}_m$ at node m are thus given.

$$(5.3) \quad \sum_{m=1}^4 [k]_{lm}\{d\}_m = -\{r\}_l, \quad l = 1, \dots, 4$$

$$(5.4) \quad \sum_{m=1}^4 \begin{bmatrix} k_{11} & k_{12} & k_{13} & k_{14} & k_{15} \\ k_{21} & k_{22} & k_{23} & k_{24} & k_{25} \\ k_{31} & k_{32} & k_{33} & k_{34} & k_{35} \\ k_{41} & k_{42} & k_{43} & k_{44} & k_{45} \\ k_{51} & k_{52} & k_{53} & k_{54} & k_{55} \end{bmatrix}_{lm} \begin{Bmatrix} u \\ v \\ w \\ \alpha \\ \beta \end{Bmatrix}_m = - \begin{Bmatrix} r_u \\ r_v \\ r_w \\ r_\alpha \\ r_\beta \end{Bmatrix}_l$$

The drilling DOF is included with a penalty stiffness in the condensed element stiffness matrix in Eq. (4.107) by expanding a row and column corresponding to the addition of a DOF and load at each node as marked by the bold font.

$$(5.5) \quad \sum_{m=1}^4 \begin{bmatrix} k_{11} & k_{12} & k_{13} & k_{14} & k_{15} & \mathbf{k}_{16} \\ k_{21} & k_{22} & k_{23} & k_{24} & k_{25} & \mathbf{k}_{26} \\ k_{31} & k_{32} & k_{33} & k_{34} & k_{35} & \mathbf{k}_{36} \\ k_{41} & k_{42} & k_{43} & k_{44} & k_{45} & \mathbf{k}_{46} \\ k_{51} & k_{52} & k_{53} & k_{54} & k_{55} & \mathbf{k}_{56} \\ \mathbf{k}_{61} & \mathbf{k}_{62} & \mathbf{k}_{63} & \mathbf{k}_{64} & \mathbf{k}_{65} & \mathbf{k}_{66} \end{bmatrix}_{lm} \begin{Bmatrix} u \\ v \\ w \\ \alpha \\ \beta \\ \mathbf{drill} \end{Bmatrix}_m = - \begin{Bmatrix} r_u \\ r_v \\ r_w \\ r_\alpha \\ r_\beta \\ \mathbf{r}_{drill} \end{Bmatrix}_l$$

The stiffness components written in bold are the added stiffnesses with a chosen penalty for each. Intuitively, k_{66} should be the only non-zero component and should only be applied along the diagonal terms of the element stiffness matrix where $l = m$ to reduce the influence from the added penalty stiffness through couplings between other DOFs and nodes.

Literature on the choice of penalty stiffness for curved shell elements in commercial codes is sparse, with the explanation of the Abaqus penalty stiffness by Tavares et al. (2022) and Dassault Systemes (2023) being the only sources found by the authors. Here, the drilling stiffness k_{drill} is calculated from the transverse shear stiffnesses k_{44} and k_{55} , the shell area associated with a given node A_s and thickness t_s . However, it is not explained how it is included in the element stiffness matrix or how A_s is defined.

$$(5.6) \quad k_{drill} = 0.05 \frac{k_{44} + k_{55}}{2} \frac{1}{1 + \frac{A_s}{10t_s^2}}$$

Tavares et al. (2022) explains how it is possible to adjust the drilling stiffness using a scaling factor. ANSYS Inc. (2018) also allows for the adjustment of the drilling stiffness, however the penalty stiffness calculation is not disclosed. It is only mentioned by both Dassault Systemes (2023) and ANSYS Inc. (2018) that the drilling stiffness is added around the surface normal. By increasing and decreasing the drilling stiffness factor in ANSYS, the effect of different drilling stiffness can be examined in a set of standard test examples.

5.1.2 Transformation of Expanded Stiffness Matrix to Global Coordinates

In the process of including the drilling stiffness, it is important to consider the coordinate system in which the drilling DOF is included, since the stiffness matrix should relate DOFs in the global coordinate system to loads in the global coordinate system. As explained in section 4.1.3, the two in-plane rotations α and β are defined as rotations in the director coordinate system at each node through the use of the base vectors of the director coordinate systems $\{V_{1i}\}$, $\{V_{2i}\}$ and $\{V_{3i}\}$. In the derivation of the shell element, the rotation around the node director is the third rotational DOF which is omitted, as it does not contribute any relative displacements. With the other two rotations being defined as in-plane rotations, the drilling stiffness should be included for rotation around the surface normal corresponding to the definition of the node directors. This section presents current knowledge on this transformation. A novel method proposed by the authors is presented in section 5.3.

Most existing methods to achieve rotations in global coordinates utilises the local orthonormal coordinate system defined by Eq. (4.56), (4.57) and (4.58) and shown in the element centre of Fig. 5.1. A transformation from global to the local orthonormal coordinate system is used on the nodal coordinates $\{X\}$ and the node directors $\{V_{3i}\}$. These are the vectors that define the element stiffness matrix and DOFs through the interpolations in section 4.1.3. This results in an element stiffness matrix defined in the local orthonormal base relating DOFs and loads in this base.

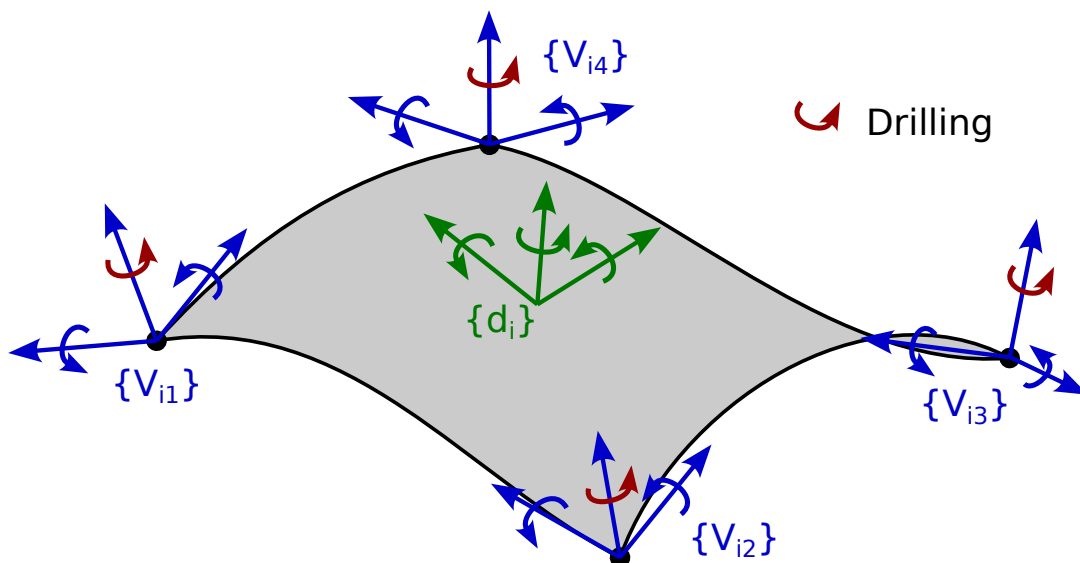


Figure 5.1. Director coordinate system at each node $\{V_{ij}\}$ with the drilling DOF marked in red and local orthonormal base $\{d_i\}$ at the element centre of a curved shell element.

The local orthonormal base is used, since the third base vector $\{d_3\}$ is defined as the normal to the curved shell surface in the element centre. Therefore, a rotation around $\{d_3\}$ will correspond to a rotation around the node directors $\{V_{3i}\}$ in flat elements, as the node directors are normal to the shell surface at the nodes. For curved surfaces, the surface normals will differ throughout the element and the node directors will be different from $\{d_3\}$ as seen in Fig. 5.1. However, a refinement of the mesh will reduce the amount of curvature in each element and the difference between $\{V_{3i}\}$ and $\{d_3\}$ will converge to 0 as the mesh is refined. Thus, the rotations defined in the director coordinate systems can be approximated by rotations in the local orthonormal base. A stiffness matrix in global coordinates can then be obtained after including the drilling stiffness, as described in section 5.1.1. Achieved by a transformation from the local orthonormal base, approximating the rotational DOFs to describe rotations in the local orthonormal base. The transformation of the stiffness matrix is made in the same way as described in Cook et al. (2001), which is expanded upon further in section 5.3 with the description of the method used in this thesis.

It is not known how the global element stiffness matrix is obtained in commercial elements such as those used by ANSYS Inc. (2018) and Dassault Systemes (2023). However, it is expected that the local orthonormal base or something similar is utilised in these elements based on similarities between preliminary tests using this method and tests with the ANSYS Inc. (2018) element.

5.2 Effect of Varying Drilling Stiffness

In order to understand the influence of the drilling stiffness, the shell element in ANSYS Inc. (2018) is used to model the set of standard FE test problems presented by MacNeal and Harder (1985) with different values of the drilling stiffness factor. Specifically, the ANSYS Inc. (2018) linear 4-node shell element with EAS and MITC stabilisation is used with drill stiffness factors set to 0.01, 1 and 100. For brevity, only the tests which showed a difference in results when varying the drilling stiffness, are included in this section.

By characterising the difference between tests that show an influence from the drilling stiffness and tests that do not show this influence, an understanding of how the results are influenced by the drilling stiffness can be achieved. Additionally, by characterising the difference between tests showing improvements with high drilling stiffness and tests that show the opposite, an understanding of parameters that indicate the required drilling stiffness can be identified. Based on this understanding, a method can be developed to achieve the desired drilling stiffness depending on the situation as done in section 5.3.

5.2.1 Tests and Results with Altered Drilling Stiffness

The tests include the straight cantilever beams with different mesh shown in Fig. 5.2, the curved cantilever beam in Fig. 5.3, the Scordelis-Lo roof in Fig. 5.4, the spherical shell in Fig. 5.5 and the twisted cantilever beam shown in Fig. 5.6. Each test is supported and loaded as shown in the figures with associated tables for geometric and material values.

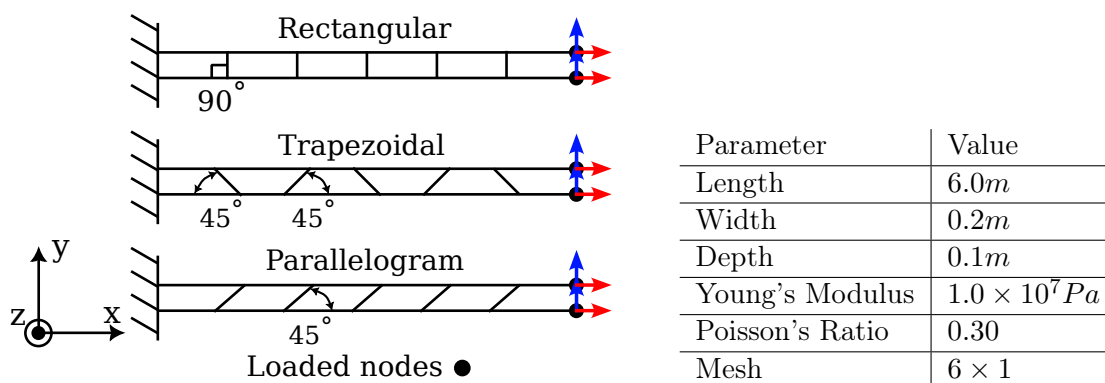


Figure 5.2 & Table 5.1. Geometry, mesh, supports and location of loading with parameters used for the straight cantilever beam. Loads are applied as a unit load split evenly between the marked nodes in the positive x direction for the extension case and the positive y direction for the in-plane shear case.

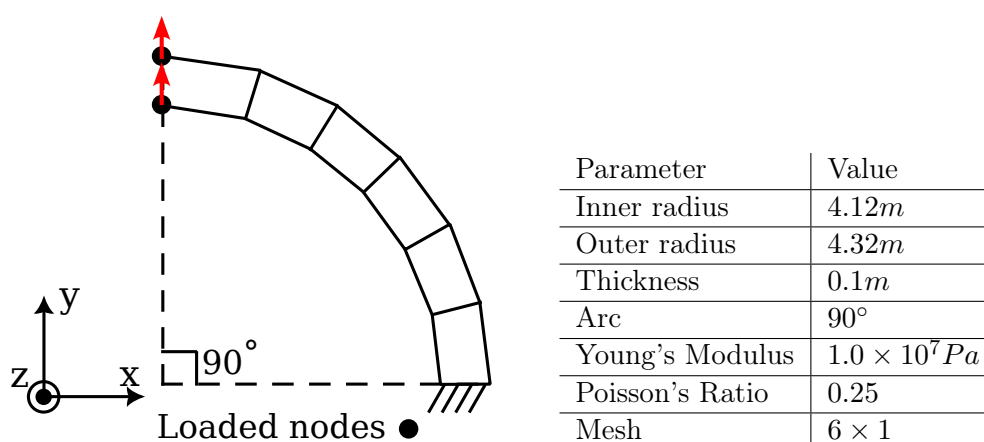


Figure 5.3 & Table 5.2. Geometry, mesh, supports and location of loading with parameters used for the curved cantilever beam. Loads are applied as a unit load split evenly between the marked nodes in the positive y direction denoted as an in-plane shear load.

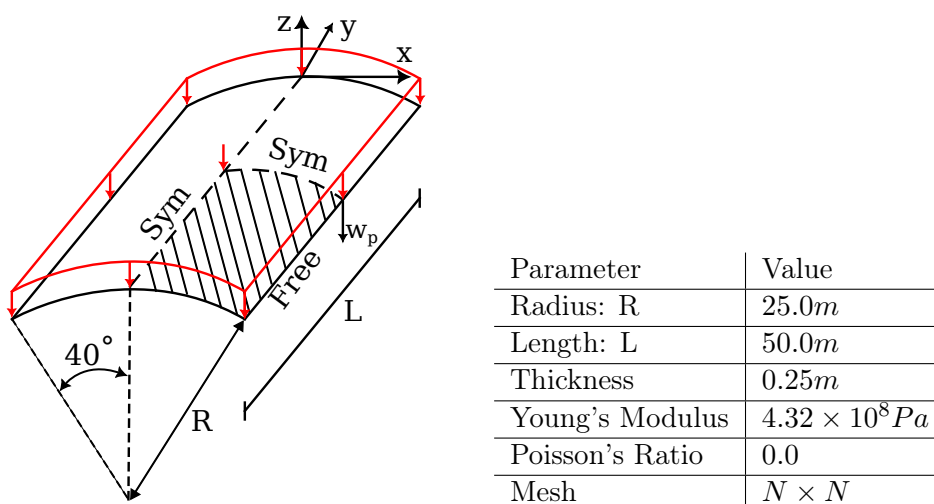
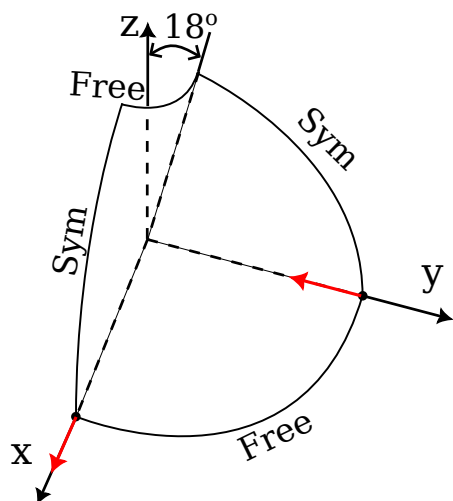


Figure 5.4 & Table 5.3. Scordelis-Lo roof geometry, supports and parameters. The roof is supported at the curved edges, where $u = 0$ and $w = 0$. The mesh is $N \times N$ on the hatched part. The load is applied as a constant pressure in the negative z direction of $90Pa$.



Parameter	Value
Radius	10.0m
Thickness	0.04m
Young's Modulus	$6.825 \times 10^7 Pa$
Poisson's Ratio	0.30
Mesh	$N \times N$

Figure 5.5 & Table 5.4. Spherical shell geometry and parameters modelled using symmetry conditions as illustrated. The mesh is $N \times N$ on the shown part and unit loads are applied as indicated by red arrows.

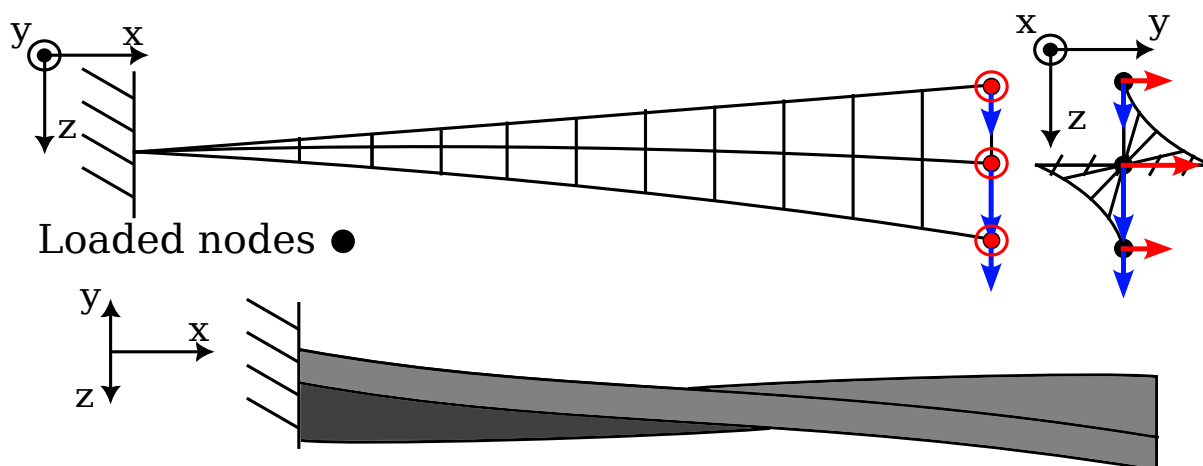


Figure 5.6. Geometry, mesh, supports and location of loading for the twisted cantilever beam. The beam is made as a 90° turn from the fixed to the free end with a linearly increasing angle along the beam length. Beam is loaded by a unit load distributed along the edge of the free end with a load of $0.5N$ at the center node and $0.25N$ at the corner nodes. The load is in the positive y direction for the in-plane shear case and the positive z direction for the out-of-plane shear case.

Parameter	Value
Length	12.0m
Width	1.10m
Depth	0.32m
Twist	90° (root to tip)
Young's Modulus	$29.0 \times 10^6 Pa$
Poisson's Ratio	0.22
Mesh	12×2

Table 5.5. Twisted beam test parameters.

The results showed a difference between using the different drilling stiffness factors for in-plane shear deformation in the straight and curved cantilever beams, as shown in table 5.6. All tests containing curved surfaces showed an influence from the drilling stiffness as shown in table 5.7.

Beam Mesh Load	Straight		Straight		Straight		Curved
	Rectangular Shear	Trapez Extension	Shear	Extension	Shear	Extension	Shear
Analytical Solution	0.1081m	0.03mm	0.1081m	0.03mm	0.1081m	0.03mm	0.08734m
Drill factor 0.01	0.993	1.011	0.052	1.012	0.632	1.012	0.888
Drill factor 1	0.982	1.011	0.052	1.012	0.627	1.012	0.878
Drill factor 100	0.488	1.009	0.045	1.009	0.340	1.009	0.417

Table 5.6. Analytical solution to test problems and normalised maximum displacement from ANSYS in load direction with different drilling stiffness factors. Thus a value of 1 means perfect agreement with the analytical solution.

Geometry Mesh/Load	Scordelis-Lo roof		Spherical shell		Twisted beam	
	$N = 2$	$N = 10$	$N = 2$	$N = 10$	In-plane	Out-of-plane
Analytical Solution	0.3024m	0.3024m	0.0940m	0.0940m	1.754mm	5.424mm
Drill factor 0.01	1.375	1.008	0.893	0.989	4.990	5.238
Drill factor 1	1.375	1.002	0.727	0.988	1.040	1.043
Drill factor 100	1.346	0.999	0.098	0.914	0.987	0.994

Table 5.7. Analytical solution to test problems and normalised displacements from ANSYS with different drilling stiffness factors. For the Scordelis-Lo roof, displacements are the w component at the centre of the free edge in the direction of loading. For the spherical shell and twisted beam, displacements are the maximum displacement in the load direction.

5.2.2 Analysis of Drilling Stiffness Effect

It can be seen from the tests included in table 5.6 that only the in-plane shear and bending deformation is affected by the drilling stiffness. This is also the case with the trapezoidal and parallelogram mesh loaded in extension as the distorted mesh cause spurious displacements in the y direction of about 2/3 the displacement seen in the loading direction. This v displacement increases as the drilling stiffness decreases and the in-plane bending deformation causes the slight differences in the extensional displacement. The influence from the drilling stiffness can be explained for the in-plane shear loaded beams as the presence of deformation corresponding to a rotation around the surface normal. An investigation of the stiffness matrix in a plane shell element in ANSYS Inc. (2018) found that it contained non-zero drilling stiffness for in-plane translational DOFs ($k_{16}, k_{26}, k_{61}, k_{62}$) relating the drilling DOF to in-plane translations u and v . It is likely this penalty on the coupling terms that cause the influence seen from the drilling stiffness on the shell elements with flat geometry. The investigation also showed that the penalty stiffness was added to ($k_{16}, k_{26}, k_{61}, k_{62}, k_{66}$) in all stiffness blocks $[k]_{lm}$ not just the stiffness blocks along the diagonal, meaning coupling between nodes is also applied in the ANSYS Inc. (2018) element.

The surface normal also describes a difference between the curved surface tests in table 5.7 and

the tests showing no influence from change in drilling stiffness. As the shell surface becomes curved, the surface normal begins to differ depending on where in the element it is located. This means both the in-plane rotational DOFs and rotation around the surface normal are around different axes in one node compared to the other nodes. The results in table 5.7 show that the nature of the curvature also has an influence on how the drilling stiffness affects the element accuracy. It can be seen from the table that the single curvature of the Scordelis-Lo roof and saddle-like curvature of the twisted beam both have improved accuracy with increased drilling stiffness, while the spherical shell is improved by a lower drilling stiffness. This effect is very significant with the twisted beam.

From this analysis, it is clear that the surface normal is an important factor in characterising the influence from the drilling stiffness. This corresponds with the intention of including the drilling stiffness as a replacement for the stiffness lost by omitting the DOF for rotation around the node director. Based on this knowledge, a method can be proposed to take advantage of the direction of the node directors to obtain the desired drilling stiffness in different situations.

5.3 Novel Method for Including Drilling in Curved Shell Elements

The expansion of the element stiffness matrix should add a drilling stiffness to avoid singularities, when including a drilling DOF and moment. However, the addition of the drilling stiffness is primarily motivated by the desired ability to apply boundary conditions in global coordinates. The analysis of the ANSYS Inc. (2018) shell element indicated a need to account for the different shell surface normals at the nodes in curved shell elements.

To achieve an element stiffness matrix with drilling in global coordinates, it is proposed to transform stiffness components related to rotational DOFs at each node from the corresponding director coordinate system to the global coordinate system. This transformation removes the approximation in the coordinate transformation that shell surface normals are equal in small elements and transforms the rotational stiffness terms according to the director coordinate systems in which the rotational DOFs and moments are defined. The resulting element stiffness matrix in global coordinates takes into account the difference between node directors in curved shell elements in a manner that is independent from the chosen drilling penalty stiffness.

The transformation approach uses the element stiffness matrix as defined in chapter 4, which uses global nodal coordinates and node directors defined in the global coordinate system. Subsequent to the expansion of the element stiffness matrix described in section 5.1.1, the resulting matrix is composed of blocks $[k]_{lm}$ relating DOFs $\{d\}_m$ in node m to loads $\{r\}_l$ in node l as shown by Eq. (5.2). Each of these blocks contains a 6×6 matrix $[k]_{lm}$ as shown in Eq. (5.5), which relates 3 translations in global coordinates and 3 rotations in director coordinates to corresponding forces and moments.

$$(5.7) \quad \sum_{m=1}^4 \begin{array}{c} \text{Translation} \\ \\ \\ \\ \text{Rotation} \end{array} \begin{array}{c} \text{Translation} \\ \\ \\ \\ \text{Rotation} \end{array} \begin{array}{c} k_{11} \quad k_{12} \quad k_{13} \\ k_{21} \quad k_{22} \quad k_{23} \\ k_{31} \quad k_{32} \quad k_{33} \\ - \quad - \quad - \\ k_{41} \quad k_{42} \quad k_{43} \\ k_{51} \quad k_{52} \quad k_{53} \\ k_{61} \quad k_{62} \quad k_{63} \end{array} \begin{array}{c} | \\ | \\ | \\ + \\ | \\ | \\ | \end{array} \begin{array}{c} k_{14} \quad k_{15} \quad k_{16} \\ k_{24} \quad k_{25} \quad k_{26} \\ k_{34} \quad k_{35} \quad k_{36} \\ - \quad - \quad - \\ k_{44} \quad k_{45} \quad k_{46} \\ k_{54} \quad k_{55} \quad k_{56} \\ k_{64} \quad k_{65} \quad k_{66} \end{array} \begin{array}{c} \left(\begin{array}{c} \Delta u \\ \Delta v \\ \Delta w \\ - \\ \Delta \alpha \\ \Delta \beta \\ \Delta \text{drill} \end{array} \right)_m \\ \\ \\ \\ \\ \\ \\ \end{array} = - \begin{array}{c} \left(\begin{array}{c} r_u \\ r_v \\ r_w \\ - \\ r_\alpha \\ r_\beta \\ r_{\text{drill}} \end{array} \right)_l \\ \\ \\ \\ \\ \\ \\ \end{array}$$

In order to obtain rotations in the global coordinate system, a transformation is applied to the load and DOF vectors. These vectors each contain 8 smaller vectors with 3 components, each describing the 3 translations or 3 rotations of a node. Cook et al. (2001) describes the transformation for each vector containing 3 translational DOFs at a node. Where in this case, a transformation is not necessary as the translations are defined in the global coordinates. However, each of the vectors containing the 3 rotational DOFs at a node α , β and drill are defined by components in the director coordinate system of the node and can be transformed the same way when assuming small rotations. The global components of these vectors denoted by the subscript e can be obtained by multiplication of the components in the director coordinates denoted by subscripted V , with the base vectors of the director coordinate system $\{V_{1i}\}$, $\{V_{2i}\}$ and $\{V_{3i}\}$.

$$(5.8) \quad \begin{Bmatrix} \alpha_i \\ \beta_i \\ \text{drill}_i \end{Bmatrix}_e = \alpha_{iV} \{V_{1i}\} + \beta_{iV} \{V_{2i}\} + \text{drill}_{iV} \{V_{3i}\} = \begin{bmatrix} \{V_{1i}\} & \{V_{2i}\} & \{V_{3i}\} \end{bmatrix} \begin{Bmatrix} \alpha_i \\ \beta_i \\ \text{drill}_i \end{Bmatrix}_V$$

The matrix is composed of the orthonormal director base at node i , meaning the transpose and inverse are the same. The components in the director coordinates can thus be found from the global components by multiplication with the transpose of the matrix. Applying this transformation to the DOF and load vectors, along with the trivial transformation of the translations with the identity matrix, yields the following transformation matrix $[T]$.

$$(5.9) \quad [I_3] = \begin{bmatrix} 1 & 0 & 0 \\ 0 & 1 & 0 \\ 0 & 0 & 1 \end{bmatrix}_{3 \times 3} \quad [V_{\text{base}}]_i = \begin{bmatrix} \{V_{1i}\}^T \\ \{V_{2i}\}^T \\ \{V_{3i}\}^T \end{bmatrix}_{3 \times 3}$$

$$(5.10) \quad [T] = \begin{bmatrix} [I_3] & [0] & [0] & [0] & [0] & [0] & [0] & [0] \\ [0] & [V_{\text{base}}]_1 & [0] & [0] & [0] & [0] & [0] & [0] \\ [0] & [0] & [I_3] & [0] & [0] & [0] & [0] & [0] \\ [0] & [0] & [0] & [V_{\text{base}}]_2 & [0] & [0] & [0] & [0] \\ [0] & [0] & [0] & [0] & [I_3] & [0] & [0] & [0] \\ [0] & [0] & [0] & [0] & [0] & [V_{\text{base}}]_3 & [0] & [0] \\ [0] & [0] & [0] & [0] & [0] & [0] & [I_3] & [0] \\ [0] & [0] & [0] & [0] & [0] & [0] & [0] & [V_{\text{base}}]_4 \end{bmatrix}_{24 \times 24}$$

This matrix transforms the DOF and load vectors from having rotations defined in the global coordinate systems at each node to having rotations in the director coordinate system.

$$(5.11) \quad \{d\}_V = [T]\{d\}_e \quad \{r\}_V = [T]\{r\}_e$$

This transformation is applied to the stiffness matrix as shown in Cook et al. (2001), by considering the governing equation in global coordinates and with rotations in director coordinates.

$$(5.12) \quad [k]_e\{d\}_e = -\{r\}_e \quad [k]_V\{d\}_V = -\{r\}_V$$

Using the above transformations, this expression can be rewritten to express the relation between global loads and DOFs by a transformed director stiffness matrix.

$$(5.13) \quad [k]_e\{d\}_e = -\{r\}_e = -[T]^T\{r\}_V = [T]^T[k]_V\{d\}_V = [T]^T[k]_V[T]\{d\}_e$$

$$(5.14) \quad [k]_e = [T]^T[k]_V[T]$$

With 24 DOFs, the vectors in the above expression have 24 components and the matrices have 24 rows and columns. This transforms the rotational DOFs according to their definition as rotations in the director coordinate system defined uniquely at each node. Consequently, the transformation provides a global stiffness matrix allowing for boundary conditions to be defined in the global coordinate system.

Using this transformation of the rotations from the director coordinate system at each node means the surface normal at each node is taken into account, regardless of the penalty stiffness applied to the drilling. The difference between the node directors in curved shell elements is therefore accounted for and the dependence of the element on the chosen penalty stiffness is reduced, as will be shown through testing with different drilling stiffness in the following section.

The method proposed here is intended to reduce the dependency on the drilling stiffness used. However, it is still necessary to apply a fictitious penalty stiffness to ensure singularities are avoided. The best value for the penalty stiffness is likely problem dependent and defining a physically based drilling stiffness would likely entail alterations to the existing shell formulation and require more extensive derivations which will not be carried out in this thesis. Therefore, the drilling penalty stiffness used in this thesis will be defined based on the stiffness terms k_{44} and k_{55} relating the two in-plane rotations to the corresponding moments. The stiffness penalty is applied to the added stiffness terms k_{66} along the diagonals of the stiffness matrix. Thus only relating the drilling DOF and moment at the same node to each other. This is done for reasons of computational efficiency and to avoid any unwanted effects from applying penalty stiffness to terms coupling other DOFs or nodes. A penalty factor p is used to manually adjust the size of the drilling stiffness and will be specified in the following section.

$$(5.15) \quad k_{66} = \frac{k_{44} + k_{55}}{p}$$

5.4 Testing of Drilling Method

With a new implementation for the drilling DOF, the tests made for the ANSYS implementation in table 5.6 and 5.7 are repeated with the new implementation. Additionally, the method is

tested with the non-linear formulation on a linear and non-linear test example to determine the influence of the method when accounting for non-linearity. To ensure that the novel method does not cause problems with the EAS stabilisation, the presented element with the novel drilling method was tested using the membrane and bending patch tests from MacNeal and Harder (1985). Both tests were passed, ensuring convergence of the element with the new drilling method.

5.4.1 Linear Drilling Tests

In the linear tests which are the same as tested with the ANSYS Inc. (2018) element in section 5.2, the influence of the drilling stiffness penalty is investigated. This is done by evaluating the linear problems with penalty factors p of 10, 10^3 and 10^5 . The tests are made both with the drilling penalty stiffness only on the diagonals of the stiffness matrix and with the drilling penalty stiffness in all blocks of Eq. (5.2).

Beam Mesh Load	Straight Rectangular Shear	Straight Trapezium Extension	Shear	Straight Parallelogram Extension	Shear
Analytical Solution	0.1081m	0.03mm	0.1081m	0.03mm	0.1081m
5 and 6 DOF results	0.993	1.011	0.052	1.012	0.632
ANSYS	0.982	1.011	0.052	1.012	0.627

Table 5.8. Normalised results for tests that do not change with different drilling penalty stiffness or 5 DOF formulation. A value of 1 means perfect agreement with analytical solution. ANSYS results are for the standard drilling factor in ANSYS of 1.

Geometry Mesh/Load	Curved Beam Shear	Scordelis-Lo roof		Twisted Beam	
		$N = 2$	$N = 10$	In-plane	Out-of-plane
Analytical Solution	0.08734m	0.3024m	0.3024m	1.754mm	5.424mm
5 and 6 DOF results	0.888	1.442	1.003	0.988	0.997
ANSYS	0.878	1.375	1.002	1.040	1.043

Table 5.9. Normalised results for tests that do not change with different drilling penalty stiffness or 5 DOF formulation. A value of 1 means perfect agreement with analytical solution. ANSYS results are for the standard drilling factor in ANSYS of 1.

With the linear shell formulation, the results of the tests did not change regardless of the usage of the drilling DOF and the penalty constant used, as expressed in table 5.8 and 5.9, with the exception of the spherical shell, as expressed in table 5.10. Compared with ANSYS using the standard drilling factor of 1, the 4-node shell element with the presented drilling method is as accurate or more in all tests except for the Scordelis-Lo roof, where it is less accurate with a coarse mesh. However, a rapid convergence is seen as the difference with ANSYS and the analytical solution is very small at a discretisation of $N = 10$.

	Results $N = 2$	Results $N = 10$
Analytical Solution	0.0940m	0.0940m
5 DOF	6.645e-4	0.075
$p = 10$	0.010	0.221
$p = 10^3$	0.304	0.970
$p = 10^5$	1.003	1.005
$p = 10$ at diagonal	0.005	0.255
$p = 10^3$ at diagonal	0.240	0.976
$p = 10^5$ at diagonal	0.994	1.005
ANSYS	0.727	0.988

Table 5.10. Normalised results for Spherical Shell with varying drilling stiffness and with 5 DOF formulation. A value of 1 means perfect agreement with analytical solution

The spherical shell test is the only one of the tests which is double curved and has boundary conditions with the drilling DOF on a curved edge. It can be seen how the 5 DOF formulation is far from the analytical solution, which is a consequence of the boundary conditions on the rotation around the surface normal having no load or DOF to be applied through. The results are different with inclusion or exclusion of the sixth DOF and the value of the penalty factor also has an influence, as the results in table 5.10 show. The spherical shell was also tested without symmetry conditions to remove the boundary conditions on the drilling DOF at a curved edge. This test showed no influence from changes to the drilling penalty stiffness.

Another test where boundary conditions are applied to the drilling DOF on a curved edge is the Scordelis-Lo roof test illustrated in Fig. 5.4, if symmetry conditions are utilised. The symmetry conditions were originally not used, but the test has been remade with the symmetry conditions applied that among others impose a fixed drilling rotational DOF, where one of the symmetry conditions are on a curved edge. The results stated in table 5.11, show that the inclusion or exclusion of the sixth DOF has a large influence, but the change in penalty factor has less of an influence at the different values that were investigated. This could be attributed to a smaller curvature on the curved edge with symmetry conditions applied or only having the symmetry conditions applied to one curved edge.

	Results $N = 2$	Results $N = 10$
Analytical Solution	0.3024m	0.3024m
5 DOF	0.941	0.788
$p = 10$	1.372	1.003
$p = 10^3$	1.417	1.003
$p = 10^5$	1.417	1.003
$p = 10$ at diagonal	1.372	1.003
$p = 10^3$ at diagonal	1.417	1.003
$p = 10^5$ at diagonal	1.417	1.003

Table 5.11. Normalised results for Scordelis-Lo roof with and without drilling. A value of 1 means perfect agreement with analytical solution.

From the tests, it stands clear that the inclusion of the sixth DOF is necessary in situations with curved surfaces that are used in the boundary conditions. At the discretisation of $N = 2$ for Scordelis-Lo roof test in 5.11, the results with the 5 DOF formulation are closer to the analytical solution. However, this is more likely the error of excluding the sixth DOF which counters the error of a rough discretisation. The test with the sixth DOF are deemed more favorable, as they

are closer to the solutions with the full model in table 5.9.

In terms of the penalty factor with the novel method presented, only the results from the spherical shell were highly dependent on the value of the penalty factor. In that case a high penalty factor, meaning a low drilling stiffness, resulted in the more accurate response. The results did not show a clear best method of implementing drilling stiffness. It is therefore only applied to the diagonal terms, relating the drilling DOF to the drilling moment at the same node. Based on the results for the spherical shell, a value of $p = 10^5$ and $p = 10^3$ is used on the spherical shell test with additional mesh discretisations and ANSYS for comparison in table 5.12.

Spherical Shell	$N = 2$	$N = 6$	$N = 10$	$N = 50$
Analytical Solution	0.0940m	0.0940m	0.0940m	0.0940m
$p = 10^5$	0.994	1.031	1.005	0.995
$p = 10^3$	0.240	0.904	0.976	0.995
ANSYS	0.727	0.983	0.988	0.995

Table 5.12. Normalised results for spherical shell with different drilling penalty methods. A value of 1 means perfect agreement with analytical solution.

From the spherical shell test, the effects of the novel method can be seen to have a clear effect for the results with few elements, as there will be a greater effect of taking the direction of the node directors into account. The novel method with $p = 10^5$ converges in an odd way, with an overshoot at $N = 6$ and $N = 10$, which could be attributed to the penalty stiffness. However, it is also a known problem dependent side effect of the incompatible modes used with EAS stabilisation. By increasing the drilling stiffness with $p = 10^3$, the overshoot does not happen but the results are heavily affected at rough discretisations. The element formulation from ANSYS achieves inferior but reasonable results without the overshoot seen in the novel method with $p = 10^5$. The novel method with $p = 10^5$ achieves the results closest to the analytical solution and can be used for the most accurate results at all discretisations. Therefore, a value of $p = 10^5$ is used in chapter 7.

5.4.2 Non-Linear Drilling Tests

The inclusion of drilling in the non-linear element formulation was tested using the linear spherical shell test with $N = 10$ and two non-linear problems. The non-linear problems consisted of one with and one without a boundary condition applied to the drilling DOF on a curved edge. The results presented here are only those used to analyse drilling with further results from testing the non-linear element formulation presented in chapter 7.

For the non-linear formulation, the inclusion or exclusion of the sixth DOF does have an influence in situations where information is lost without it, as in the spherical shell from Fig. 5.5. The results for the test completed with and without the sixth DOF are listed in table 5.13.

Spherical Shell $N = 10$	X Displacement	Z Displacement
Analytical Solution	0.0940m	0.0940m
5 DOF	0.0425	0.000
6 DOF	1.010	0.998

Table 5.13. Results for linear spherical shell test example using the non-linear element formulation. A value of 1 means perfect agreement with analytical solution.

For the results with the sixth DOF, the value of the stiffness penalty factor does not change the end result of the non-linear analysis. Rather, the value of the stiffness penalty factor changes the convergence of the non-linear solver through slightly different changes to the displacement in each step. This is caused by the use of the residual as the convergence criteria in the non-linear solver. The residual is calculated as expressed in Eq. (4.108), without using the stiffness matrix and is therefore unaffected by the drilling stiffness penalty. Instead, the 5 DOF residual is calculated and expanded to 6 DOF by inserting 0 as the drilling moment residual, since the element should not carry a load on the drilling DOF. The results with 5 DOF are very off due to the application of boundary conditions with no DOFs or loads to be applied to.

The spherical shell test in Fig. 5.5 can be changed by reducing the thickness to one fourth and doubling the loads to model more non-linear behaviour. This provides a non-linear test problem with boundary conditions applied to the drilling DOF on curved edges. Here, it can be shown how the number of iterations necessary to solve the problem changes with 25 load steps with different penalty factors, as shown for each load step in Fig. 5.7 with a penalty factor p of 10, 10^3 and 10^5 respectively.

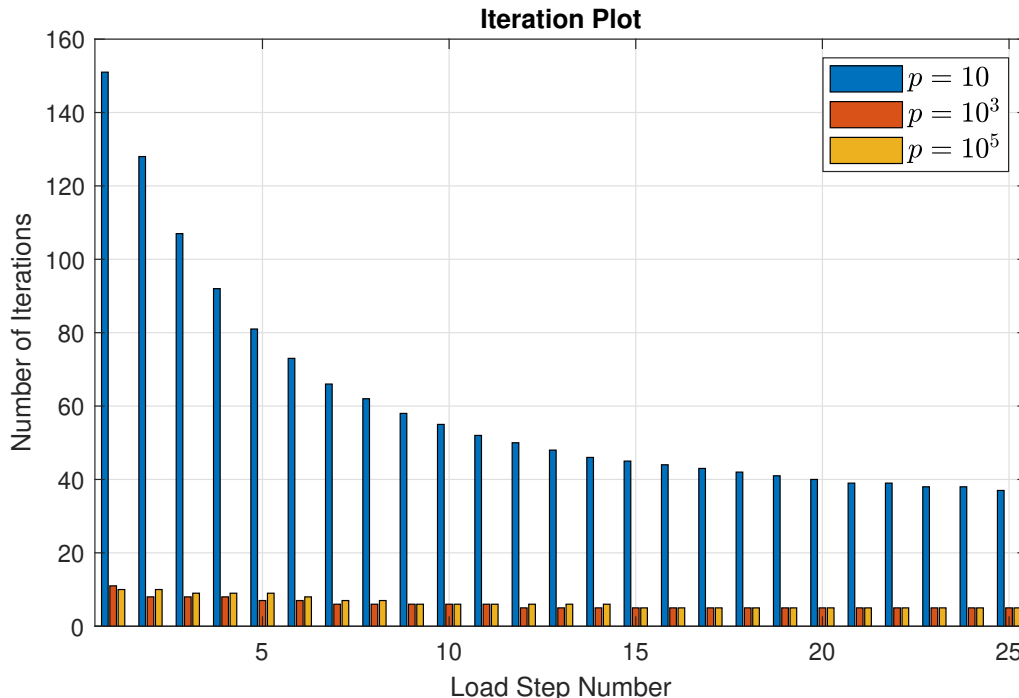


Figure 5.7. Bar plot of number of iterations used for each load step to converge in the non-linear spherical shell problem.

The graph in Fig. 5.7 shows how the small penalty factor corresponding to a large drilling penalty stiffness, significantly increases the amount of iterations needed to converge at each load

step. It should also be noted that a value of $p = 10^3$ converged with fewest iterations in most load steps. However, both $p = 10^3$ and $p = 10^5$ showed comparatively fast convergence with little difference between the two. How the residual changed over the iterations in the first load step can be seen in appendix B.1.

Just as the value of stiffness penalty factor only changes the results for linear problems with curved edges used for boundary conditions, so does it only change the convergence for non-linear problems if curved edges used for boundary conditions are present in the problem. This was tested using the non-linear clamped angle test example used for non-linear testing in section 7.1.2 with the corresponding iteration plot in appendix B.2.

5.4.3 Remarks on Proposed Method for Drilling

The method proposed for inclusion of the drilling DOF in curved shell elements has been shown to be independent from the drilling penalty stiffness in problems without a boundary condition applied to the drilling DOF on curved edges. In these problems, improved results compared to ANSYS Inc. (2018) were achieved with a penalty factor of $p = 10^5$ applied only to the diagonal terms, showing high accuracy in the linear spherical shell problem and fast convergence in the non-linear spherical shell. However, the required drilling penalty stiffness in these problems is likely problem dependent. Therefore, tests should be performed to determine an appropriate penalty stiffness in problems, where it has an influence on the results. For this purpose, the proposed method for including the drilling DOF provides a simple framework for expanding the 5 DOF degenerated 4-node shell formulation to include drilling without the need to alter the 5 DOF formulation.

Draped Discrete Material Optimisation 6

The DMO method was chosen in section 2.4, given its robustness and computational efficiency from being a gradient based method and the immediate presumption that draping could be included in a simple decoupled manner. With the shell element formulation derived, this chapter will contain the derivation of the DMO method, followed by a proposed method to include the draping process. The derivations are based on the articles from when the method was originally proposed (Lund and Stegmann, 2005; Stegmann and Lund, 2005).

6.1 Derivation of the DMO Method

The DMO method allows for the use of gradient based methods as mentioned in section 2.4. Common between the gradient based methods is the necessary evaluation of objectives and constraints with the sensitivities from a design sensitivity analysis as the respective derivatives with respect to the design variables. There exists many different gradient based methods, which will not be covered in this thesis. However, the derivation of terms needed to apply these methods and the parameterisation of the DMO method will be presented in this section.

6.1.1 Objectives and Constraints

Several structural parameters have been derived and implemented with the DMO method. The type of objective and constraints used, depend on the desired capability of the designed structure. This thesis will cover the use of DMO with compliance modelled using linear and non-linear stabilised 4-node shell elements, and linear buckling as an objective or constraint.

Compliance Optimisation

Compliance is often used as an objective in structural optimisation of elastic structures in order to achieve maximum stiffness designs as presented initially for DMO without EAS stabilisation in Lund and Stegmann (2005); Stegmann and Lund (2005). This is both to reduce displacements and in some cases increase the strength. The compliance C is defined as the work W done by the applied loads $\{R\}$ at the state of equilibrium.

$$(6.1) \quad C(\{D\}) = W(\{D\}) = \{D\}^T \{R\}$$

Using the equilibrium equations a nested analysis and design approach can be used, where displacements $\{D\}$ are calculated before solving each iteration of the optimisation problem. This removes the need to use the equilibrium equations as a constraint in the optimisation.

$$(6.2) \quad [K]\{D\} = \{R\}$$

Using Clayperon's work theorem relating the total potential energy Π , total elastic strain energy U and work done by external loads $W = C$, it can be shown that the total elastic strain energy is related to the compliance.

$$(6.3) \quad \Pi = U - W = -\frac{1}{2}W \Leftrightarrow C = W = 2U$$

The maximum stiffness designs found are characterised by uniform strain energy density if constraints are not reached. If the strength is defined from the strain energy density, the maximum stiffness design will also have optimal strength. The total elastic strain energy can be computed for finite elements using the stiffness matrix $[K]$ and displacements $\{D\}$. An equivalent expression can be stated using stiffness $[k_e]$ and displacements $\{d_e\}$ on an element level summed over the number of elements n . Here $[k_e]$ corresponds to the element stiffness matrix derived in chapter 4.

$$(6.4) \quad U = \frac{1}{2}\{D\}^T[K]\{D\} = \frac{1}{2}\sum_{e=1}^n\{d_e\}^T[k_e]\{d_e\}$$

The expression for the elastic strain energy can then be evaluated as the objective or as a constraint in an optimisation problem exemplified here with upper and lower bounds on the design variables x_i .

$$(6.5) \quad \begin{aligned} \text{Objective : } & \min_x U \\ \text{Subject to : } & x_i^{\min} \leq x_i \leq x_i^{\max} \end{aligned}$$

The sensitivity of the objective can be evaluated analytically.

$$(6.6) \quad \frac{\partial U}{\partial x_i} = \frac{1}{2}\{D\}^T \frac{\partial [K]}{\partial x_i} \{D\} + \{D\}^T [K] \frac{\partial \{D\}}{\partial x_i}$$

The expression can be simplified by using the derivative of the equilibrium equations in Eq. (6.2) to remove the need to calculate $\partial\{D\}/\partial x_i$.

$$(6.7) \quad \frac{\partial [K]}{\partial x_i} \{D\} + [K] \frac{\partial \{D\}}{\partial x_i} = \frac{\partial \{R\}}{\partial x_i}$$

By utilising design independent loads meaning $\partial\{R\}/\partial x_i = 0$, the term with the derivative of the displacement wrt. the design variables can be expressed from the derivative of the stiffness matrix.

$$(6.8) \quad [K] \frac{\partial \{D\}}{\partial x_i} = -\frac{\partial [K]}{\partial x_i} \{D\}$$

Inserting this into Eq. (6.6) yields a simplified expression for the sensitivity which can be also be written in terms of stiffness and displacement on an element level.

$$(6.9) \quad \frac{\partial U}{\partial x_i} = -\frac{1}{2}\{D\}^T \frac{\partial [K]}{\partial x_i} \{D\} = -\frac{1}{2}\sum_{e=1}^n\{d_e\}^T \frac{\partial [k_e]}{\partial x_i} \{d_e\}$$

Using stabilised elements, the derivative of the element stiffness matrix $[k_e]$ with respect to the design variable can be calculated as the derivative of the expression in Eq. (4.107) repeated below, which is the same in both linear and non-linear problems.

$$(6.10) \quad [k_e] = [k_{uu}] - [k_{u\alpha}][k_{\alpha\alpha}]^{-1}[k_{\alpha u}]$$

Each matrix is dependent on the design variables used with the DMO parameterisation and the derivative follows from the standard rules of matrix differentiation.

$$(6.11) \quad \begin{aligned} \frac{\partial [k_e]}{\partial x_i} = & \frac{\partial [k_{uu}]}{\partial x_i} - \frac{\partial [k_{u\alpha}]}{\partial x_i} [k_{\alpha\alpha}]^{-1} [k_{\alpha u}] \\ & + [k_{u\alpha}] [k_{\alpha\alpha}]^{-1} \frac{\partial [k_{\alpha\alpha}]}{\partial x_i} [k_{\alpha\alpha}]^{-1} [k_{\alpha u}] - [k_{u\alpha}] [k_{\alpha\alpha}]^{-1} \frac{\partial [k_{\alpha u}]}{\partial x_i} \end{aligned}$$

The derivatives of $[k_{uu}]$, $[k_{u\alpha}]$, $[k_{\alpha u}]$ and $[k_{\alpha\alpha}]$ are dependent on the parameterisation, which is explained further in section 6.1.2.

The non-linear compliance optimisation used in this thesis, is defined from the work done by applied loads at the state of equilibrium found at the final load step denoted by n .

$$(6.12) \quad C(\{D_n\}) = W_n(\{D_n\}) = \{D_n\}^T \{R_n\}$$

This means, the displacements used to evaluate the compliance are calculated from a non-linear analysis. The sensitivity is calculated in the same way as for the linear compliance optimisation. However, the stiffness matrix and its derivatives are calculated using the non-linear matrices derived in chapter 4, for the deformed configuration at the final load step.

Buckling Optimisation

The buckling loads from a linear buckling analysis can be used in structural optimisation as either objective or constraint, to increase or enforce a minimum value for the first critical buckling load. This was first introduced to the DMO method by Lund (2009). The basis of the buckling optimisation is the linear buckling problem, which is solved for the eigenvalue λ_j .

$$(6.13) \quad ([K_0] + \lambda_j [K_\sigma]) \{\delta D_j\} = \{0\}, \quad j = 1, 2, \dots$$

Here $[K_\sigma]$ is the stress stiffening matrix, $\{\delta D_j\}$ is the j 'th eigenvector and $[K_0]$ is the linear part of the stiffness matrix, which is calculated from a condensation of the EAS stiffness matrices from the linear formulation on an element level.

$$(6.14) \quad [k_0] = [k_{uu}] - [k_{u\alpha}] [k_{\alpha\alpha}]^{-1} [k_{\alpha u}]$$

The sensitivity of a distinct eigenvalue λ_j with respect to the design variables x_i , can be calculated by taking the derivative of Eq. (6.13) with respect to the design variables and multiplying with the corresponding eigenvector.

$$(6.15) \quad \frac{d\lambda_j}{dx_i} = \{\delta D_j\}^T \left(\frac{d[K_0]}{dx_i} + \lambda_j \frac{d[K_\sigma]}{dx_i} \right) \{\delta D_j\}$$

The derivative of the linear stiffness matrix $[K_0]$ is exactly the same as in the linear compliance optimisation presented previously in Eq. (6.11). However, the stress stiffness matrix is an implicit function of the displacements $[K_\sigma(\{D(x_i)\}, x_i)]$. Therefore, the total derivative is used instead of the partial derivative. This extends the derivation beyond the scope of this thesis and the term is therefore calculated using finite differences.

$$(6.16) \quad \frac{d[K_\sigma(\{D(x_i)\}, x_i)]}{dx_i} \approx \frac{[K_\sigma(\{D(x_i)\}, x_i + \Delta x_i)] - [K_\sigma(\{D(x_i)\}, x_i)]}{\Delta x_i}$$

This approximation requires the sensitivity of the displacements to changes in the design variables $d\{D\}/dx_i$. These can be calculated from the derivative of the static equilibrium equation as in Eq. (6.8).

In order to avoid increasing one buckling load and decreasing others, it is necessary to consider the buckling optimisation problem as a maxmin problem. This stands for maximising the minimum buckling eigenvalue. Several methods exist for handling maxmin problems and in this case the bound method will be used on the lowest n_λ buckling eigenvalues (Arora, 2012).

$$(6.17) \quad \begin{aligned} \text{Objective : } & \max_{x, \beta} \beta \\ \text{Subject to : } & \lambda_i \geq \beta, \quad i = 1, \dots, n_\lambda \\ & x_i^{\min} \leq x_i \leq x_i^{\max} \end{aligned}$$

6.1.2 Methodology and Parameterisation

The method of DMO is to change the optimisation problem from continuous fibre angles to discrete fibre angles through predefined candidate materials as substitutes. These candidate materials are defined by the constitutive matrices and can thus differ in material, fibre angle of orthotropic materials or anything that changes the constitutive behaviour. The material used for a given layer in an element is determined from a weighted sum of the candidate materials expressed using the constitutive matrices $[C]_i$ with weights w_i summed over the number of candidates n_c .

$$(6.18) \quad [C] = \sum_{i=1}^{n_c} w_i [C]_i, \quad 0 \leq w_i \leq 1$$

The weight functions are defined to be from 0 to 1 and determine how much of the corresponding material is present in a given layer of an element. The optimisation should therefore minimise the objective function whilst driving the weight function to either 0 or 1 in order to avoid a mix of different candidates, which is unphysical. In order to correctly include mass as constraint or objective it is necessary that the sum of the weights should be 1 for the mass to be evaluated correctly. However, in this thesis the mass is not considered as the geometry is fixed and the candidates use the same material. This definition of the constitutive matrix works similarly to multi-material topology optimisation, which the DMO parameterisation is based upon.

Lund and Stegmann (2005); Stegmann and Lund (2005) presented several penalisation schemes to ensure weight functions reach their limits using a set of design variables that should also be between 0 and 1. The material with a corresponding design variable $x_i = 1$ is used. In this thesis the solid isotropic material with penalisation (SIMP) method is used, which penalises intermediate values of the design variables using a power p to push the design variable values towards the limits (Hvejsel and Lund, 2011).

$$(6.19) \quad [C] = \sum_{i=1}^{n_c} x_i^p [C]_i, \quad 0 \leq x_i \leq 1$$

$$(6.20) \quad \sum_{i=1}^{n_c} x_i = 1$$

Using the penalisation through the power p this parameterisation does not have the sum of weight functions equal to 1 and should therefore not be used with mass constraints or objectives. With the used parameterisation, the design variables x_i can be viewed as volume fractions of the candidate materials. However, it is still necessary that only a single candidate is chosen.

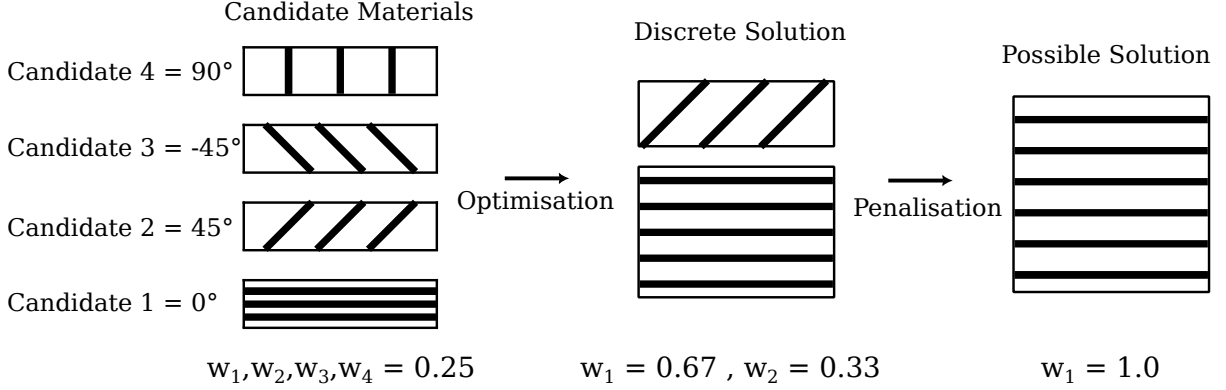


Figure 6.1. Illustration of the DMO process from initial point with a layer consisting of the four candidate materials through the process of optimising the weight function to a discrete solution and then utilising penalisation to achieve a discrete possible solution.

As the geometry is considered fixed, the weight functions and design variables only affect the constitutive matrix in the element stiffness matrices. Thus, the sensitivities of the element stiffness matrices needed in Eq. (6.11) are calculated by replacing the constitutive matrix by its sensitivity.

$$(6.21) \quad \frac{\partial [k_{uu}]}{\partial x_i} = \int [B]^T \frac{\partial [C]}{\partial x_i} [B] dV$$

$$(6.22) \quad \frac{\partial [k_{u\alpha}]}{\partial x_i} = \frac{\partial [k_{\alpha u}]^T}{\partial x_i} = \int_V [B]^T \frac{\partial [C]}{\partial x_i} [\tilde{M}] dV$$

$$(6.23) \quad \frac{\partial [k_{\alpha\alpha}]}{\partial x_i} = \int_V [\tilde{M}]^T \frac{\partial [C]}{\partial x_i} [\tilde{M}] dV$$

For non-linear compliance optimisation these expressions become more complex due to implicit dependencies on displacements as seen with the stress stiffness matrix for linear buckling optimisation. Therefore, a finite difference approximation is applied on the element level for evaluating the non-linear stiffness matrix derivative. This is done in the same way as for the stress stiffness matrix in Eq. (6.16).

The sensitivity of the constitutive matrix is calculated by taking the derivative of Eq. (6.19).

$$(6.24) \quad \frac{\partial [C]}{\partial x_i} = p x_i^{(p-1)} [C]_i$$

The gradient based optimisation requires an initial design from which to iterate toward the optimal solution. In the case of DMO, the initial point has the same value $x_{initial}$ for all design variables defined from the number of design variables n_{DV} to ensure the sum of design variables is 1.

$$(6.25) \quad x_{initial} = \frac{1}{n_{DV}}$$

This initial value is chosen to avoid favouring any candidate materials and increase the likelihood of finding the unbiased global discrete optimum. This works well in many cases, where the best candidates are found and the penalisation ensures each design variable reaches the limit and only the single best candidate is chosen. However, the DMO method can still end up with a local optimum, due to the non-convex nature of the optimisation problems with the use of gradient based optimisation schemes.

Convergence

With the redefined optimisation problem, it must also be defined when the optimisation is considered converged. This is achieved through a convergence tolerance ε which is typically set in a range of 95 – 99.5%. This convergence tolerance is utilised to evaluate if the weight factors are converged for an element through an inequality equation.

$$(6.26) \quad w_i \geq \varepsilon \sqrt{w_1^2 + w_2^2 + \dots + w_{nc}^2}$$

When the inequality equation is satisfied, the element is flagged as converged and counts toward the total number of converged elements N_c^e . The number of converged elements is used with the total number of elements N^e to determine the ratio of converged elements h_ε .

$$(6.27) \quad h_\varepsilon = \frac{N_c^e}{N^e}$$

The optimisation can be considered converged even with some elements not flagged as converged with a high enough convergence ratio at e.g. 99.5%. For the unconverged elements, the material with the largest weight factor can then be chosen for the element. However, it should be noted that the mix of different candidate materials present in unconverged elements is not physical and a reevaluation of the objective with fully specified materials would be advised.

Geometrical Association of Design Variables

The design variables are each associated with a candidate material and a part of the geometry, where the candidate can be placed. In Lund and Stegmann (2005); Stegmann and Lund (2005) each design variable is associated with a candidate and an element, such that each element can have a different material. The design variables can also be associated with patches using the same material for a larger part of the geometry. In both cases illustrated in Fig. 6.2, the design variable is also associated with a specific layer of the laminate. This better represents the process of placing fibre mats in a mould covering patches of the structure and corresponds to finding the solution to the problem of which orientation each fibre mat should have when placed. The use of patches is necessary to include draping, as the fibre angle of each element in the same patch is dependent on the draped fibre angles in addition to the nominal fibre angle. The inclusion of draped fibre angles in the optimisation might result in a different optimal candidate for a patch, as the fibre angles of each element in the patch will differ depending on the draping instead of being the same, as illustrated in Fig. 6.2.

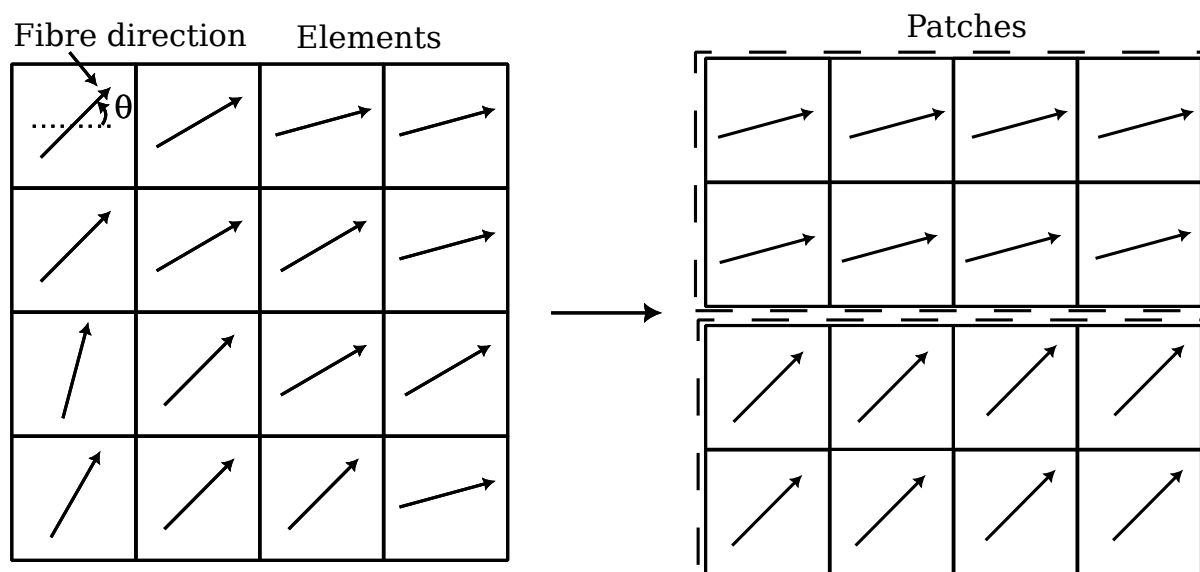


Figure 6.2. Illustration of element mesh with individual fibre directions being grouped into two patches with linked fibre directions.

6.2 Incorporating Draping Into DMO

The DMO method can be used to find the optimal discrete fibre angle for each element in a discretised structure. However, it is particularly useful for finding the optimal orientation of larger fibre mats covering patches of multiple elements. It is in the placement of these fibre mats that the draping process described in section 2.2, yields changes to the fibre angles throughout a structure. The changed fibre angles have an influence on the constitutive properties and could therefore result in different optimal orientations of each fibre mat, when placed in double curved moulds.

6.2.1 Accounting for Draped Fibre Angles in DMO

The draped fibre angles are taken into account in FEA as described in section 2.3.4, using the draped fibre angles to rotate the constitutive matrix, as described in section 4.3. This method of incorporating the draped fibre orientations translates well to the DMO parameterisation. By performing a draping analysis for each patch and each discrete orientation of the FRP candidate materials, the fibre angle deviations from draping corresponding to each element in a patch and candidate material can be added to the discrete orientations used for each candidate. As the orientation of the constitutive matrix is applied through rotations on an element level, it is necessary to determine the corresponding draped fibre angle for each element. With regards to DMO, it is necessary to utilise design variables associated with larger patches covering multiple elements corresponding to the fibre mats placed during manufacturing.

6.2.2 Inclusion of Draping Data

The draping analyses for this thesis are completed in the Composite Modeler add-on for Dassault Systemes (2022) utilising a kinematic draping model. However, any draping model that calculates fibre angle deviations may be used to accommodate for the different FRP materials

used. Most of the draping models including Composite Modeler, provide data sets containing discrete values for the fibre angle deviations in points throughout the structure. The kinematic models use cells that deform with the geometry to model the draping process. The discrete data of the kinematic draping models are provided at the vertices of the cells. Therefore, the provided fibre angle deviations do not correspond to the elements used in FEA, as shown with a model of a hemisphere from Dassault Systemes (2022) in Fig 6.3.

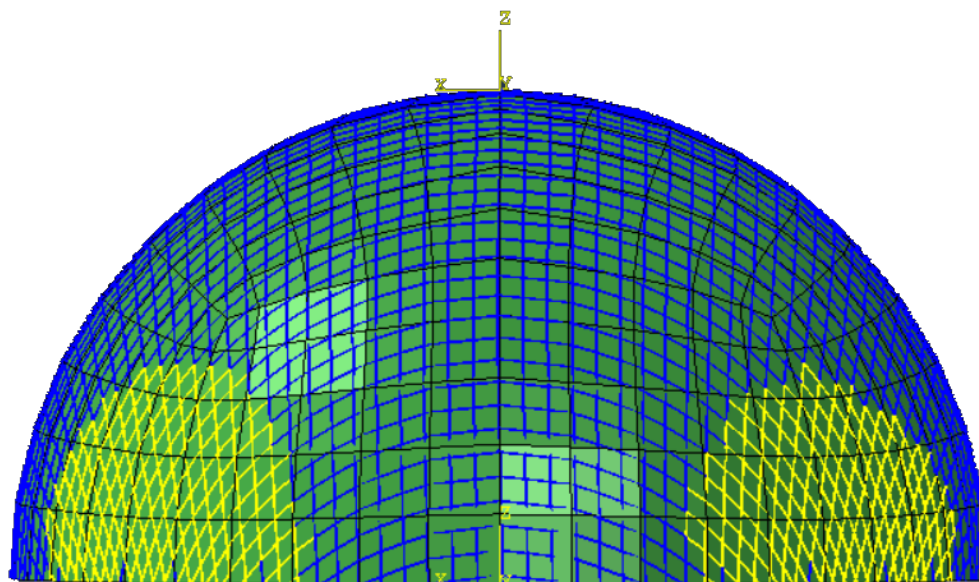


Figure 6.3. Kinematic model of hemisphere with finite element shells in green and kinematic cells that are coloured by the shear strain in blue and yellow, with yellow indicating high shear strains. The draping data is provided in the vertices of the kinematic draping cells.

On a previous semester, a method was developed for translating a data set with fibre angle deviations and corresponding positional coordinates into fibre angle deviations for each element in a FEA (Stagsted and Bertelsen, 2022). The method utilises the area of the element and location of the nodes to determine a tolerance describing if the point is inside the element or how close the point is to being inside the element. The fibre angle deviations from the kinematic draping analysis in Fig. 6.3 are shown in Fig. 6.4 with the corresponding fibre angle deviations determined for each element in a FEA shown in Fig. 6.5. This method has proved to be very robust and can be applied to any data set from a draping analysis containing positions and fibre angle deviations. The method has also been tested on the 9 node element in MUST and works for this element as well.

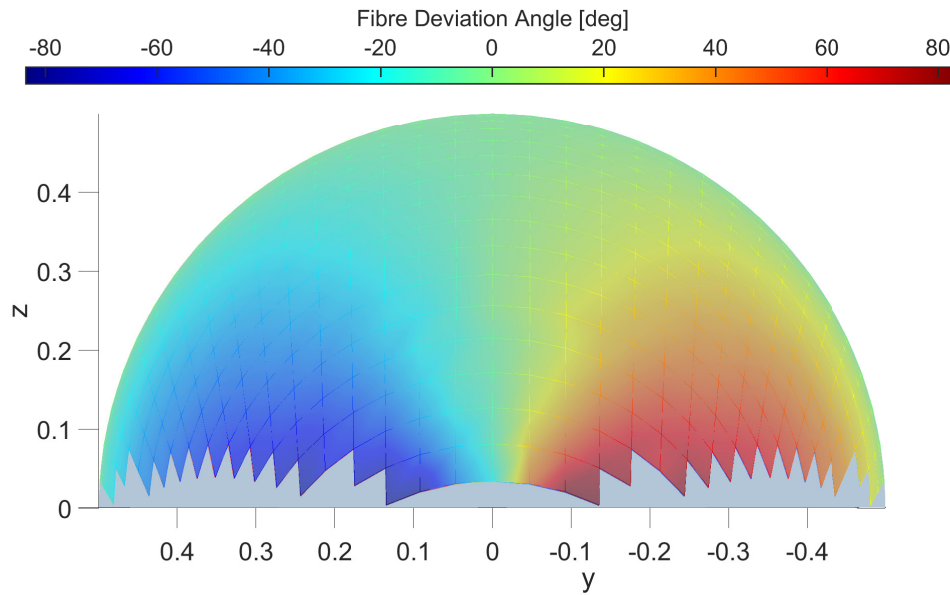


Figure 6.4. Model of hemisphere with draping data provided in cell vertices from a kinematic draping analysis.

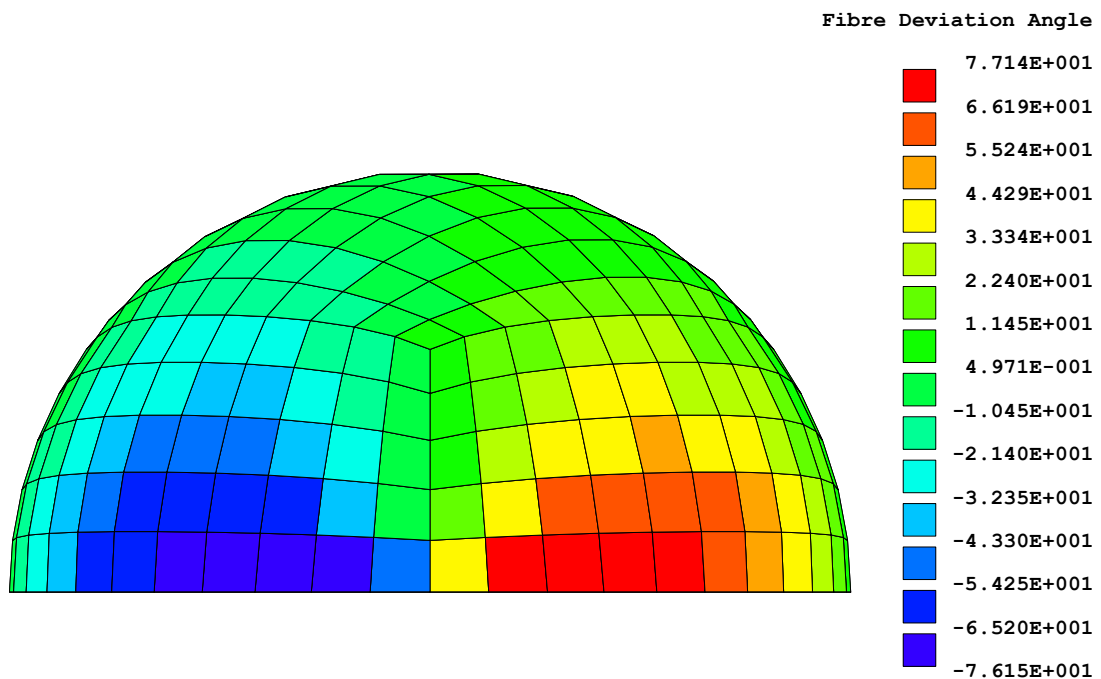


Figure 6.5. Finite element model of hemisphere with draping data for each element provided from a translation of the data shown in Fig. 6.4 from a kinematic draping analysis.

Structural Tests for the Element Formulation 7

As the objective of this thesis is to develop a finite element formulation with drilling and draping for structural optimisation, structural tests will be performed on the different parts individually and together. First, the element formulation will be tested and subsequently used for optimisation, where utilisation of draped fibre orientations will be added. During the tests, the developed stabilised 4-node shell element formulation in MUST will be compared to other available element formulations in MUST and ANSYS.

The shell element formulation has been derived in terms of both geometric non-linearity with large displacements and a novel method for inclusion of the drilling DOF. Therefore, the element formulation can be tested to achieve a comprehensible understanding of the abilities of the element and to gauge if the element formulation meets the requirements set in chapter 3.

To couple the optimisation with draping data to the shell element formulation, tests will be performed on double curved geometries with and without draping data to compare results. Additional optimisation tests will be performed on new geometries to test buckling eigenvalue and non-linear compliance optimisation without draping data.

7.1 Non-Linear Tests of 4-node Shell Element Formulation

The non-linear tests are a spherical shell for general geometrically non-linear (GNL) behaviour of a double curved structure, a clamped angle geometry that can test stability and a cylindrical shell under concentrated load for a GNL test caused mainly by large displacements. In the non-linear and buckling tests, the 4-node shell element presented in this thesis is compared to the 4-node shell element from ANSYS Inc. (2018) and the solid shell element from Johansen (2009).

7.1.1 GNL Spherical Shell Test

The GNL spherical shell geometry and parameters are given in Fig. 7.1 and table 7.1, which is the same setup as in Fig. 5.5 but with reduced thickness and increased load.

The tests are completed with large displacements taken into account through the element formulation described in chapter 4. The deformation of the structure is showcased in Fig. 7.2, where the undeformed and deformed structures are shown.

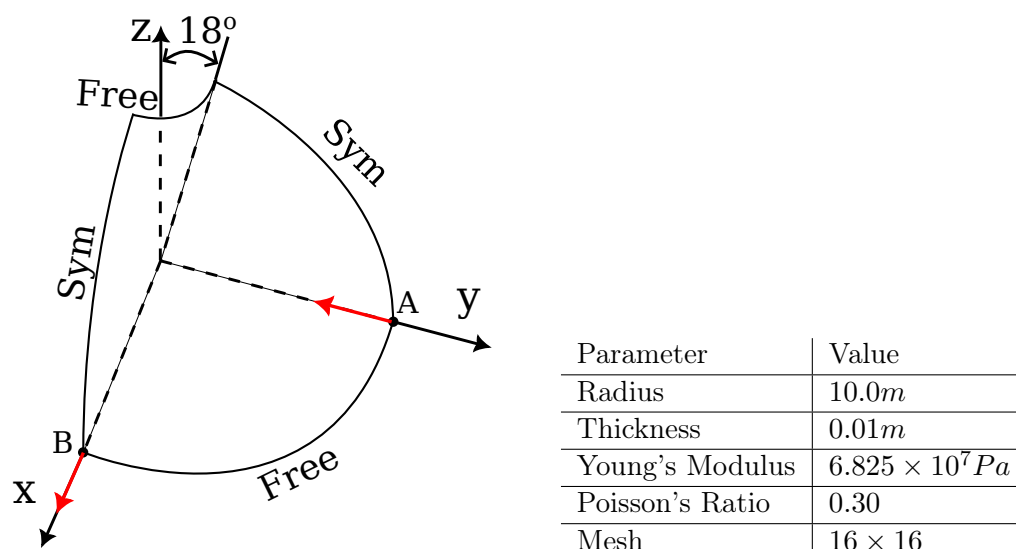


Figure 7.1 & Table 7.1. Spherical shell geometry and parameters modelled using symmetry conditions as illustrated. The mesh is 16×16 on the shown part and two $2N$ loads are applied as indicated by the red arrows.

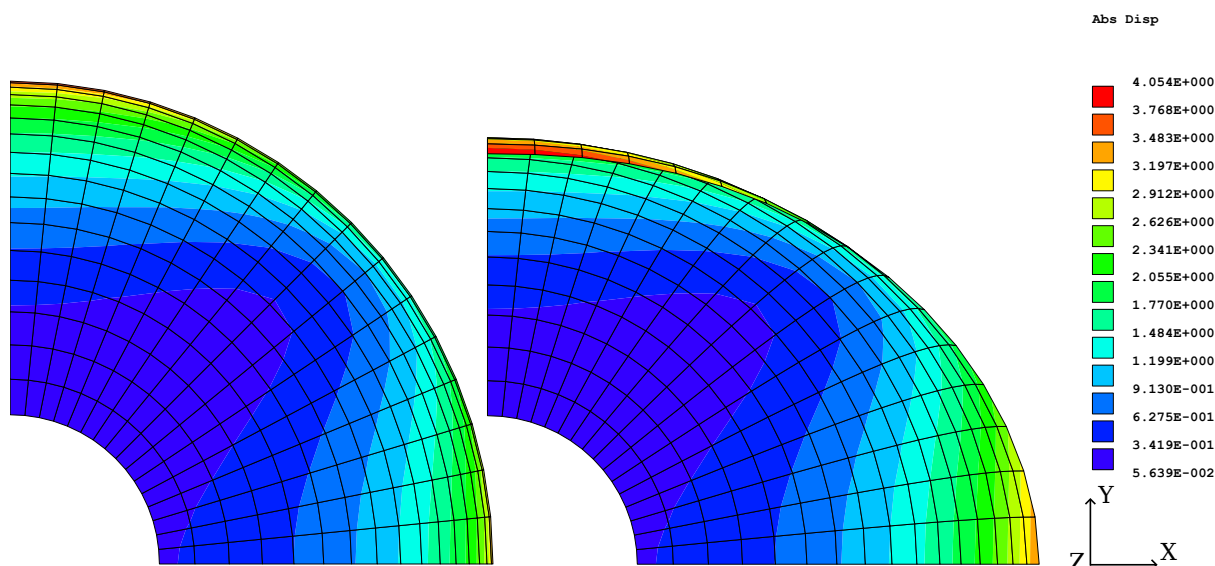


Figure 7.2. Undeformed geometry to the left and deformed geometry to the right of the spherical shell test. Displacements are expressed in meters.

The structural response is compared in terms of the displacements in the load direction at node A and B from Fig. 7.1. The force-displacement response at the two nodes from the implemented shell element formulation in MUST is plotted in Fig 7.3, with the ANSYS Inc. (2018) 4-node shell element and a solid shell formulation in MUST as comparison. In ANSYS large deformations are applied, which include large displacements and stress stiffening as in the implementation presented in this thesis, but also further includes large rotations (ANSYS, 2023). The inclusion of large rotations can explain the difference in the results from ANSYS and the 4-node shell implementation. Johansen (2009) also investigated the problem with a solid-shell formulation, where large rotations are not a consideration given the solid-shell only uses translational DOFs. Compared to the results from Johansen (2009), the results obtained with the shell formulation in this thesis seems to give a good representation, with still a noticeable difference which is likely given the assumption of small rotations.

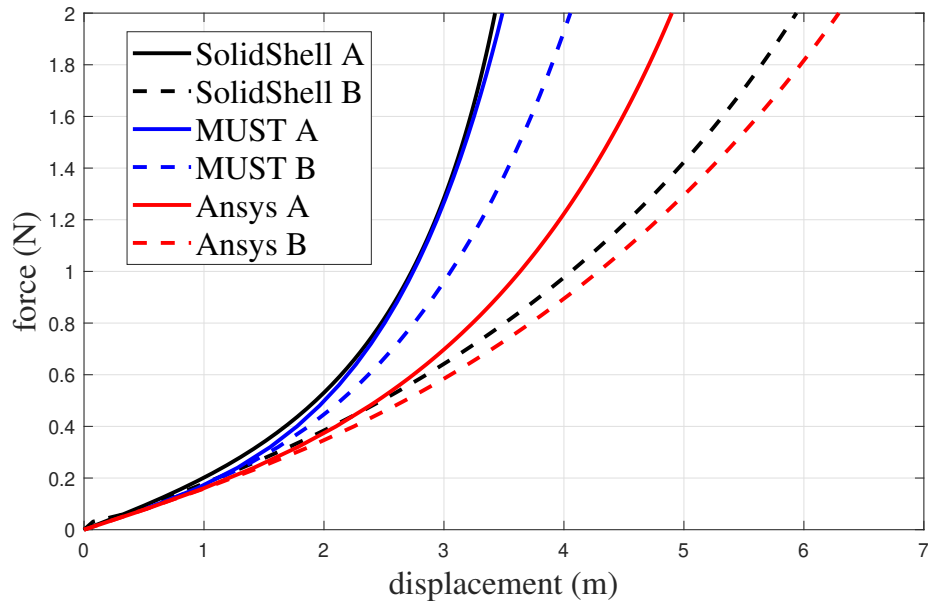


Figure 7.3. Force-Displacement graph of the spherical shell test at the nodes loaded. Displacement of point A is opposite the Y-axis direction and of point B in the X-axis direction.

The number of iterations taken to complete the given load steps are also given for the shell implementation in this thesis and ANSYS, which is shown in Fig. 7.4. Here, it can be observed that the number of iterations necessary is quite similar in the first six iterations. Afterwards, the ANSYS formulation heavily increases the number of iterations, whereas the implementation in this thesis continues to use fewer. This behaviour reinforces the hypothesis that the implementation in MUST accurately represents the large displacements, but as the force increases, large rotations become more dominating and causes the differences seen between ANSYS and MUST in terms of structural response and number of iterations.

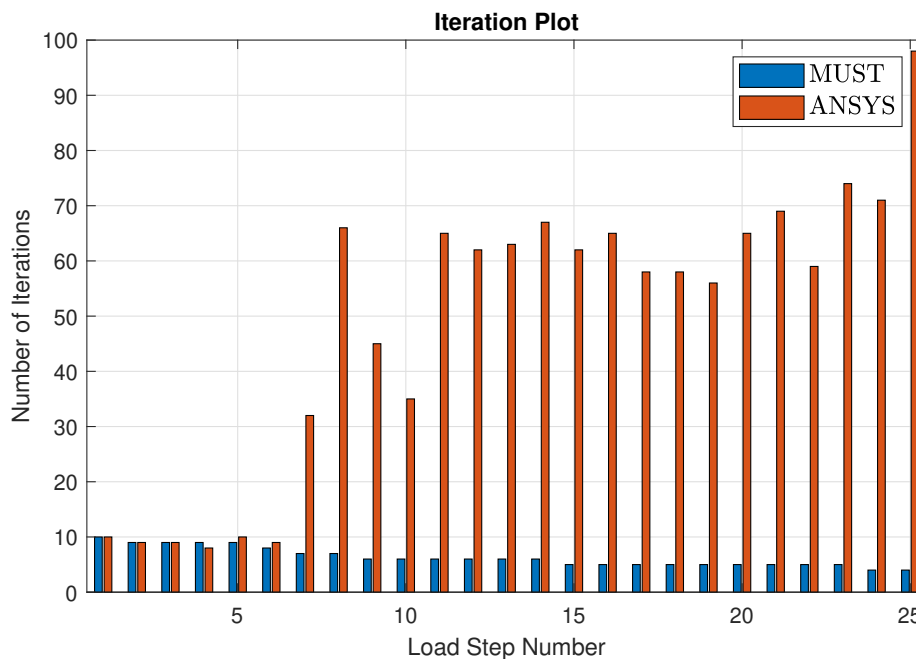


Figure 7.4. Iteration plot with the number of iterations used to converge each load step with the spherical shell test using a full Newton-Raphson solver with a force convergence criteria of $10^{-6}N$.

7.1.2 Clamped Angle Test

The stability test can be used to compare a GNL static analysis and a linear buckling analysis. The clamped angle geometry is a clamped 90 degree angle, which is loaded at point A as illustrated in Fig. 7.5.

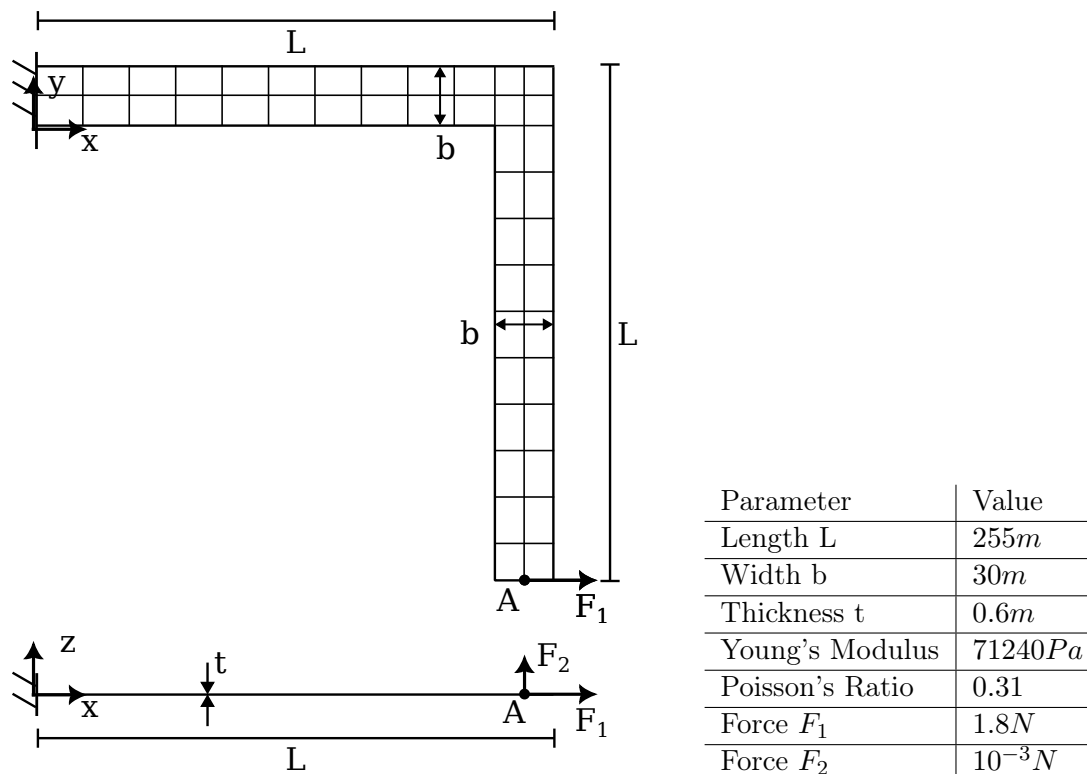


Figure 7.5 & Table 7.2. Clamped angle geometry, mesh, loads and parameters illustrated. The load F_2 is a disturbance load used to simulate imperfections and is only present in the GNL analyses.

The instability triggered in the GNL analysis is used as comparison with a linear buckling analysis. The buckling mode that is triggered is the lowest positive buckling mode and can be seen in Fig. 7.6, which is the deformation achieved with the GNL analysis.

The force-displacement curve for the point loaded in Fig. 7.5, is compared between the different implementations in Fig. 7.7. It can be observed that the shell implementation presented in this thesis has the smallest displacements, where the solid-shell implementation from Johansen (2009) and ANSYS have larger displacements and are quite similar. Again, the linear and initial non-linearity is quite similar for the shell implementation from this thesis and the other implementations until large rotations start to affect the problem. The given problem can be considered with a linear buckling analysis to investigate the discrepancy between a GNL analysis and a linear buckling analysis.

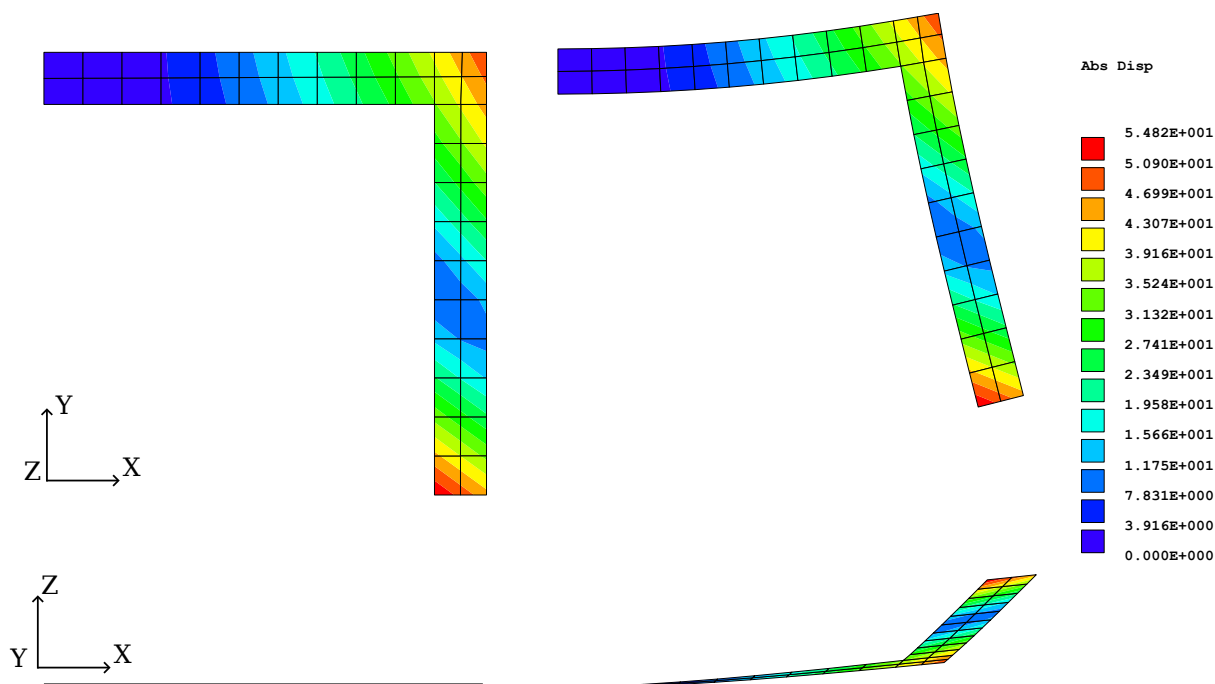


Figure 7.6. The undeformed geometry on the left and deformed geometry on the right of clamped angle with in-plane view at the top and out-of-plane view at the bottom. Displacements are expressed in meters.

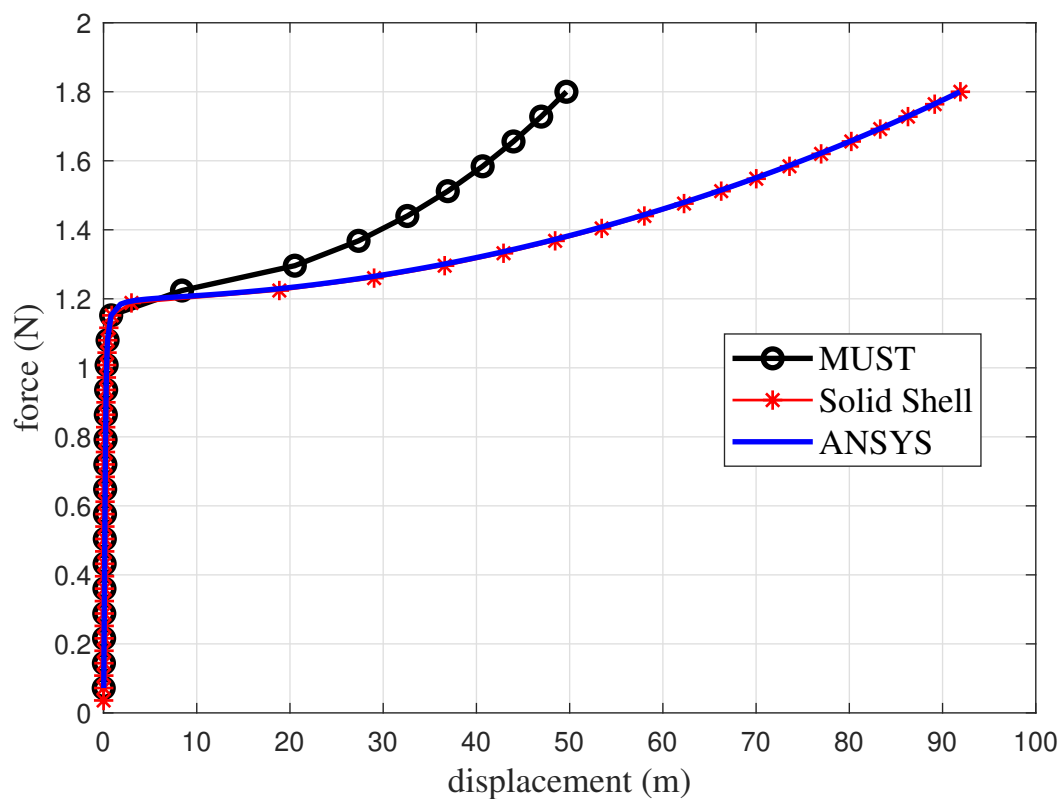


Figure 7.7. Force-displacement graph of the clamped angle test for point A.

Evaluating the stability of the problem through a linear buckling analysis, the critical buckling load is determined and stated in table 7.3. The results in the table are close between the

different elements tested. The results also match the GNL force-displacement behaviour in Fig. 7.7, where the curve flattens just below a force of $1.2N$. It is expected that the GNL force displacement relationship will begin following the bifurcated path before reaching the buckling load due to the disturbance force F_2 .

Method and program	Bifurcation Point
MUST Linear Buckling	1.204N
ANSYS Linear Buckling	1.199N

Table 7.3. Table of results of critical buckling load for the clamped angle tests with geometrically non-linear analyses and linear buckling analyses.

The number of iterations from the shell element implementation in MUST and ANSYS are given in Fig. 7.8. The figure shows that the number of iterations are similar in the linear part of the problem, but as instability and large displacements begin to occur, both formulations require an increased amount of iterations with ANSYS requiring considerably more. Given the small difference between the ANSYS shell formulation and the solid shell formulation, it again seems that large rotations are the main contributor to the difference between the shell implementations in MUST and ANSYS. As more non-linearity is included in the ANSYS formulation, a greater number of iterations are to be expected.

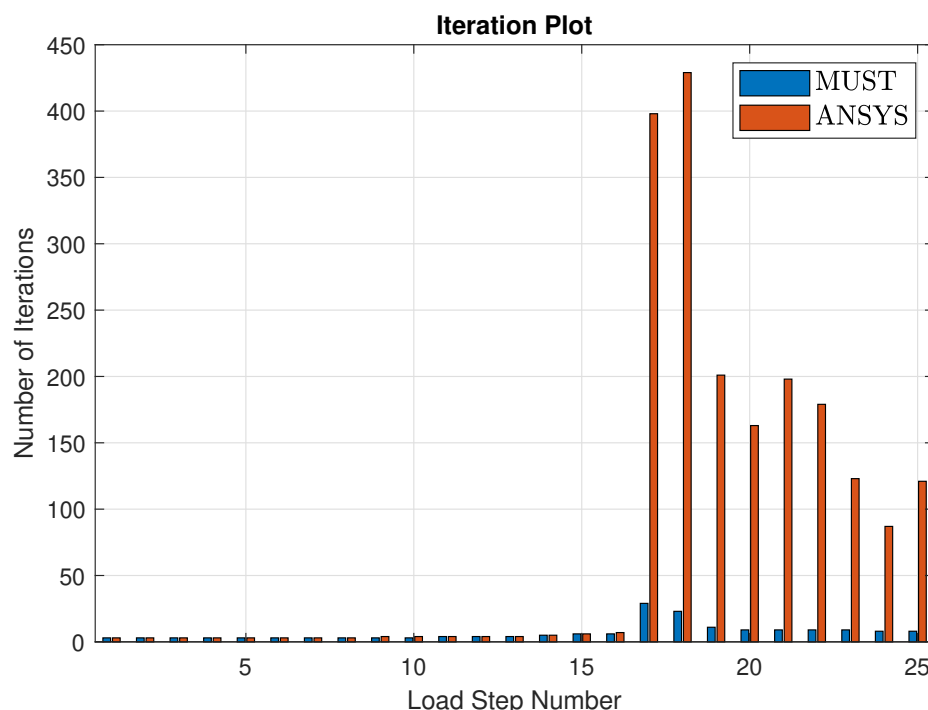


Figure 7.8. Iteration plot with the number of iterations used to converge each load step with the clamped test using a full Newton-Raphson solver with a force convergence criteria of $10^{-6}N$.

7.1.3 Cylindrical shell under concentrated load

The final non-linear test is a geometry in a similar shape as the Scordelis-Lo Roof in Fig. 5.4, but with different parameters, boundary conditions and load. The curved edges of the structure are now free, where the straight edges have fixed translational displacements and the structure is loaded with a concentrated load in the center, which is illustrated in Fig. 7.9 with parameters stated in table 7.4. The test is from Meek and Ristic (1997), and it is described that large displacements are the major contributor to the non-linearity. Furthermore, the geometry undergoes a limit and turning point, therefore applying the arc-length method is necessary to solve the problem (Cook et al., 2001). The structure and deformations are shown with the undeformed and scaled deformed geometry in Fig. 7.10.

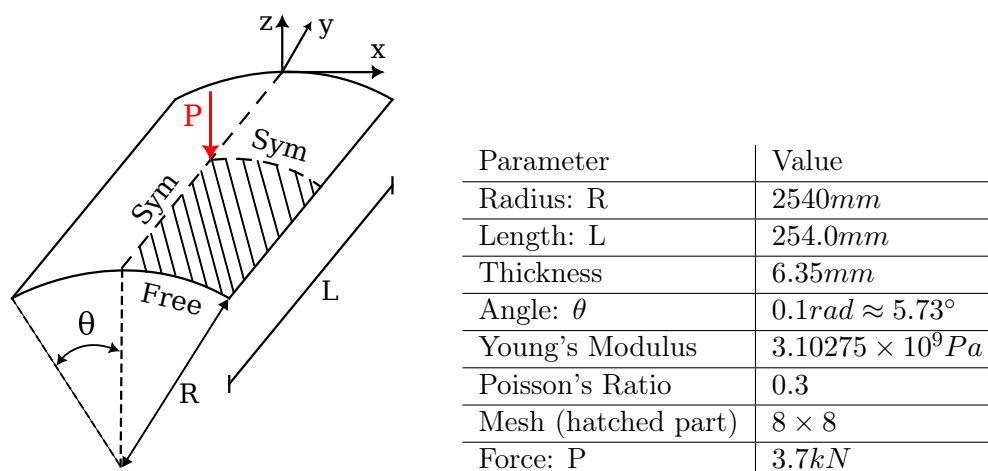


Figure 7.9 & Table 7.4. Geometry, supports and parameters of the cylindrical shell under concentrated load. The geometry is supported at the straight edges, where $u = 0$, $v = 0$ and $w = 0$.

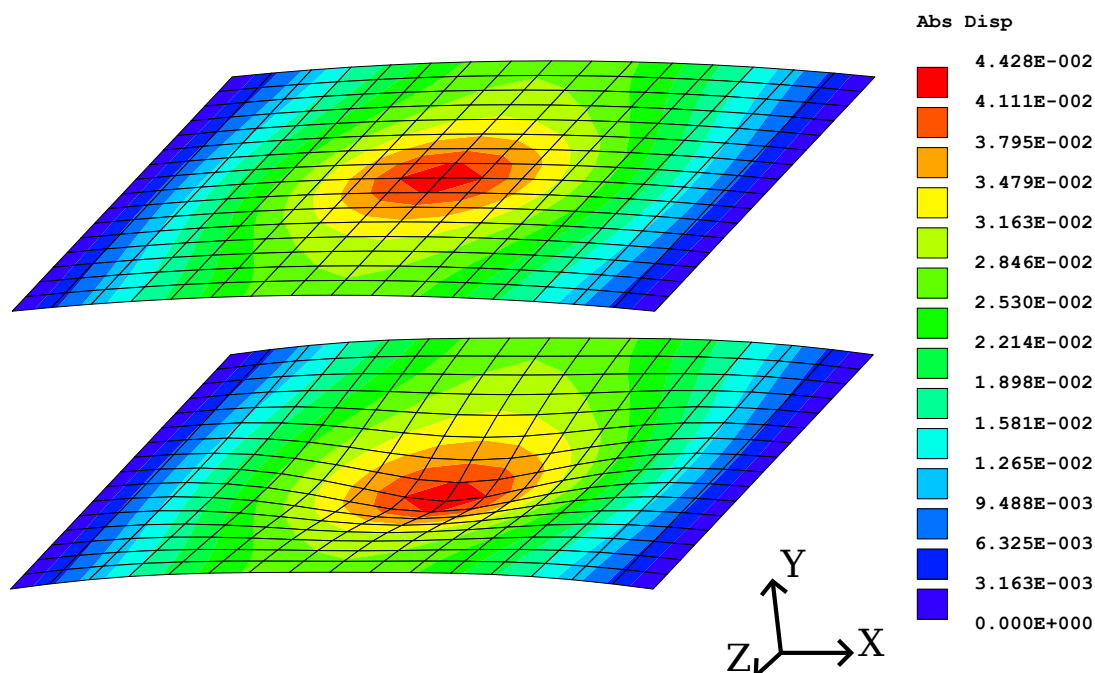


Figure 7.10. Undeformed geometry at the top and deformed geometry at the bottom of the figure, where the deformations in the deformed geometry have been scaled by a factor of 20 for clarity. Displacements are expressed in meters.

The test is analysed with the 4-node shell formulation implemented in MUST and compared to the 4-node shell formulation in ANSYS, using the force-displacement relation at the point where the structure is loaded, which is shown in Fig. 7.11.

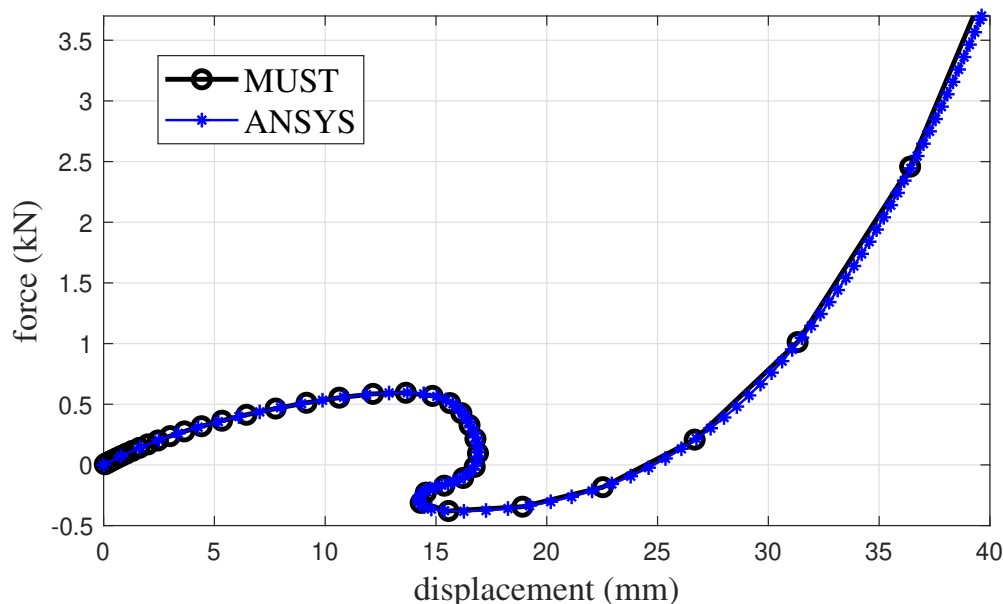


Figure 7.11. Force-displacement graph of the cylindrical shell test for point loaded with a concentrated force.

It can be observed that the force-displacement relation of the shell formulation in MUST and ANSYS are close to identical. Both of the shell formulations are solved with an arc-length solver and both experience the limit and turning points. Since the shell formulations are so identical in the one non-linear tests where large displacements are the major contributor to the non-linearity, it confirms that the shell formulation presented in this thesis correctly accounts for large displacements and the discrepancy observed in the other non-linear tests can be attributed to large rotations being present.

The number of iterations used to solve the problem is shown in Fig. 7.12, with the total number of iterations for the shell formulations in MUST and ANSYS begin 97 and 127 respectively. The lower number of iterations suggests that the implementation in MUST is more effective, as the same degree of non-linearity is being modelled.

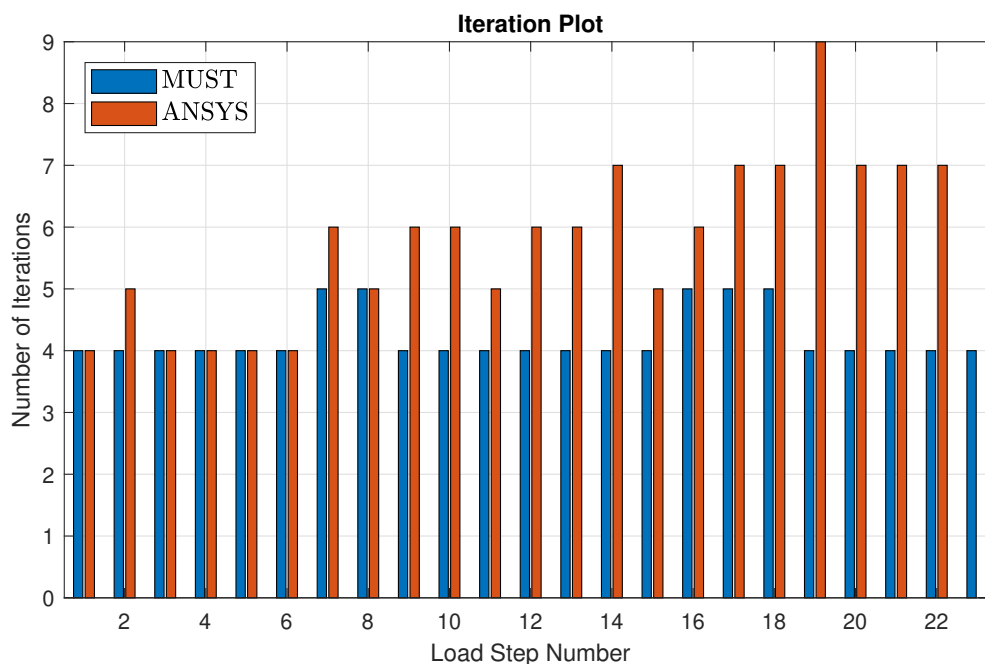


Figure 7.12. Iteration plot with the number of iterations used to converge each step with the cylindrical shell test using an arc-length solver with a force convergence criteria of $10^{-6}N$.

7.1.4 Validity of Non-Linear Shell Element Formulation

The non-linear tests were completed with the GNL formulation where large displacements are accounted for. In the tests, the developed element formulation was compared with the shell formulation in ANSYS and a solid shell formulation in MUST. The two first tests showed large discrepancies with the shell formulation, which are attributed to large rotations. The final non-linear test showed how well the shell formulation compared to ANSYS in tests where rotations can be considered small, where the structural response from the element formulations were similar. The clamped angle test, further showed how the GNL analysis compared to a linear buckling analysis, which was also similar to ANSYS. In all the tests, convergence of the non-linear solution using the presented 4-node shell element was achieved using fewer iterations with the cylindrical shell under concentrated load using only 76% of the iterations needed by ANSYS.

7.2 Tests of DMO Implementation

The DMO method is tested with each of the objectives derived in section 6.1; minimisation of linear and non-linear compliance and maximisation of the first critical buckling load. This is done to show the applicability of the 4-node stabilised shell element presented in this thesis with regards to optimisation of laminated composites. Each optimisation is performed using the 4-node element formulation presented in this thesis and the results are compared to optimisations performed using a 9-node quadratic element already present in MUST. The linear compliance optimisation will be applied to two different double curved geometries both with and without using draped fibre angles, to show the influence of draping on the optimal orientation to use when placing fibre mats in double curved moulds. The layup of the designs are specified using

the notation from Jones (1999) going up from the bottom layer as $(layer_1, layer_2, \dots)$ with fibre angles $(\theta_1, \theta_2, \dots)$.

7.2.1 Linear Compliance Minimisation with Draping

The linear compliance optimisation is performed on two different double curved geometries both with and without draped fibre angles. The geometries are referred to as the wave and the twisted roof respectively. Both tests have 2 layers of equal thickness with 12 candidates for each layer using nominal fibre angles of $(0^\circ, \pm 15^\circ, \pm 30^\circ, \pm 45^\circ, \pm 60^\circ, \pm 75^\circ, 90^\circ)$. Both tests utilise a single patch for each layer in the entire structure with the same nominal fibre angles in each element within the patch.

Wave Test

The wave is designed to have a large variation in curvatures which includes the types of curvature found in both the spherical shell and twisted beam. The structure also contains large curvatures and experiences large deviations from the nominal fibre directions when accounting for draping compared to the other geometry used. The wave geometry is illustrated with supports, applied loads, mesh and the draping deviation from a nominal fibre angle of 0° in Fig. 7.13. The material parameters of the laminate are listed in table 7.5.

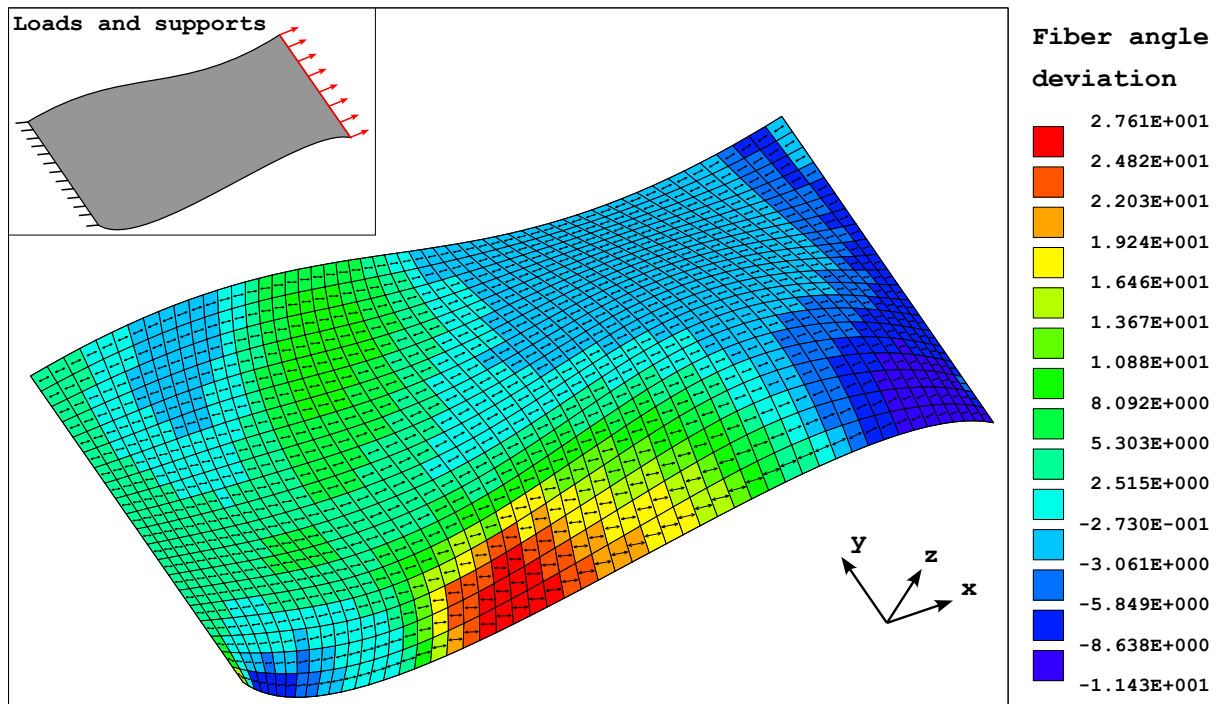


Figure 7.13. Draped fibre angle deviation in degrees from Abaqus Composites Modeler for a nominal fibre direction of 0° with black arrows illustrating the direction of fibres in each element. Loads and supports are illustrated in the upper left corner.

E_{11}	E_{22}	E_{33}	G_{12}	G_{23}	G_{13}	ν_{12}	ν_{23}	ν_{13}
137.9 GPa	9 GPa	9 GPa	9.1 GPa	6.2 GPa	9.1 GPa	0.3	0.3	0.3

Table 7.5. Material parameters of the FRP laminate used in wave test.

Twisted Roof

The twisted roof has smaller curvatures compared with the wave geometry. The structure is defined by twisting the Scordelis-Lo roof in Fig. 5.4 by 0.15 revolutions around the y-axis from one end of the structure to the other. This structure is included to have a geometry which has a more uniform curvature that is similar in size and shape to the curvatures found in wind turbine blades. The supports and loads on the twisted roof are illustrated with the draping deviation from a nominal fibre angle of 90° in Fig. 7.14. The material parameters of the laminate are listed in table 7.6.

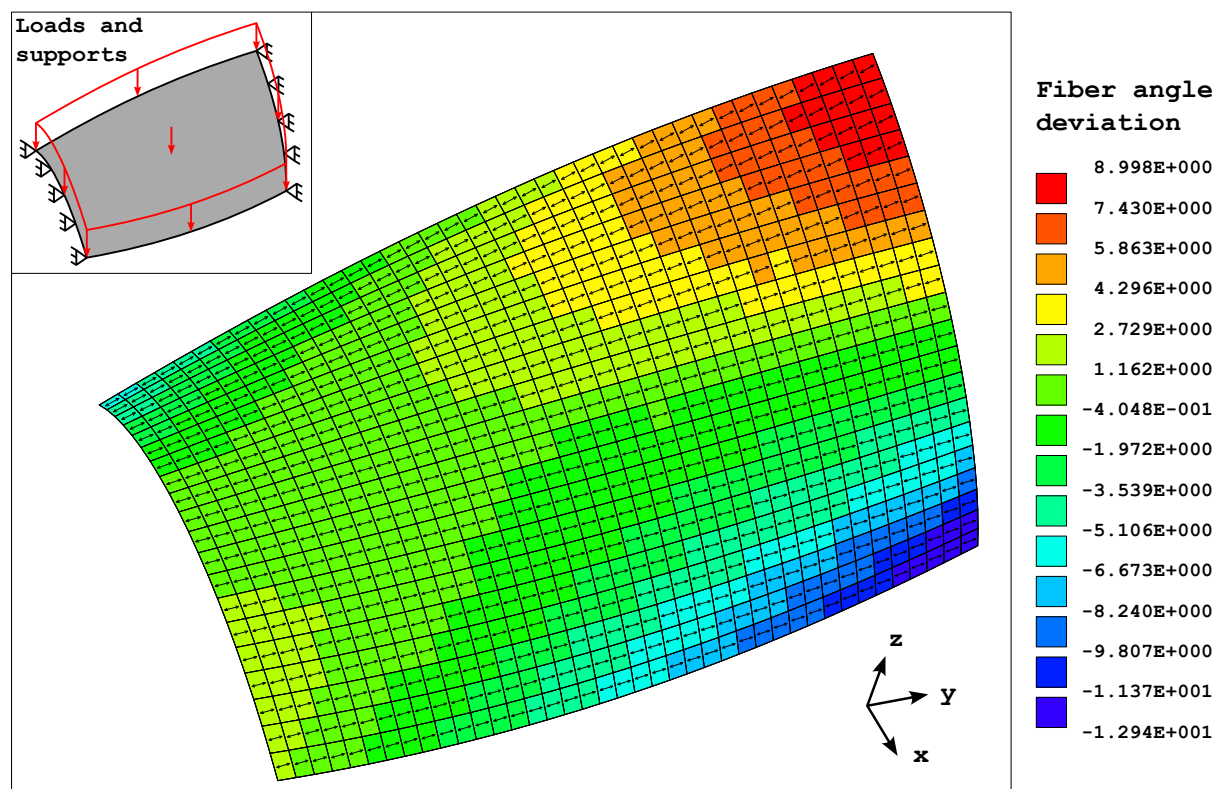


Figure 7.14. Draped fibre angle deviation in degrees from Abaqus Composites Modeler for a nominal fibre direction of 90° with black arrows illustrating the direction of fibres in each element. Loads and supports are illustrated in the upper left corner.

E_{11}	E_{22}	E_{33}	G_{12}	G_{23}	G_{13}	ν_{12}	ν_{23}	ν_{13}
45 GPa	10 GPa	10 GPa	5 GPa	3.84615 GPa	5 GPa	0.3	0.4	0.3

Table 7.6. Material parameters of the FRP laminate used in twisted roof test.

DMO Results of Linear Compliance Optimisation

The minimisation of compliance using the linear element formulations converged successfully in all optimisations performed. The results both with and without draped fibre directions are listed in table 7.7.

The optimal designs found using DMO with and without draping in table 7.7 show a clear change in the optimal design when taking draping into account. However, analysing the resulting compliance shows that only the wave modelled using the 4-node shell element finds a design

	4-node shell		9-node shell	
	Without draping	With draping	Without draping	With draping
Wave				
Optimal design	(15,15)	(0,0)	(15,15)	(0,0)
Min. compliance [J]	0.273 (0.301)	0.301 (0.293)	0.335 (0.358)	0.370 (0.361)
Twisted Roof				
Optimal design	(90,75)	(90,90)	(-75,60)	(-75,75)
Min. compliance [J]	3.00e5 (3.07e5)	3.26e5 (3.21e5)	4.12e5 (4.21e5)	4.20e5 (4.27e5)

Table 7.7. Optimal designs found using DMO with the final value of the compliance. Compliance values calculated with draping are in parentheses.

with lower compliance when accounting for draping. This indicates that accounting for draped fibre orientations can result in a different optimal design, but also indicates difficulties with converging to a global optimum. These difficulties extend to the difference between the designs found for the twisted roof using the 4-node and 9-node shells. An additional evaluation of the compliance with the $(-75, 60)$ design on the twisted roof using the 4-node shell element yielded a compliance of $2.94e5$. This is lower than the compliance of the design found using DMO with the 4-node shell, showing that the optimisation finds a local minimum. The difficulties with finding a global optimum is a consequence of using gradient based optimisation schemes on a non-convex optimisation problem and must be accepted as an uncertainty to the DMO results in this thesis.

It is worth noting the difference seen in the compliance between the 4-node and 9-node elements with the same fibre angles. With a fine mesh used for the structures as illustrated by Fig. 7.13 and 7.14, the difference in accuracy between the 4-node and 9-node elements should not be as profound. The difference is likely attributed to the novel method for including drilling, which is only used for the 4-node element as the 9-node element uses the method with the transformations in section 5.1.2. The method used for the 9-node element has been shown to yield inferior results to the novel method particularly in double curved structures such as the wave and twisted roof.

Verification of Linear Compliance DMO Implementation

In order to verify the implementation in linear compliance optimisation using DMO of the 4-node element presented in this thesis, the analytical sensitivity calculated from Eq. (6.9), is compared to a finite difference approximation of the sensitivity, which is calculated from the evaluated strain energy $U(x_i)$ at small increments in the design variables x_i . This is done to ensure the gradient based solver is supplied with the correct information needed to solve each iteration. The finite difference is calculated using the central difference method with a step length h .

$$(7.1) \quad \frac{\partial U(x_i)}{\partial x_i} \approx \frac{U(x_i + h) - U(x_i - h)}{2h}$$

The finite difference approximation can be used for verification since it is based on the evaluation of strain energy using displacements from a linear static analysis, which has been shown to be accurate for the 4-node shell in section 5.4.1. The analytical sensitivity S_a is compared to the

finite difference sensitivity S_{FD} by the percentage difference p_d .

$$(7.2) \quad p_d = 100 \left(\frac{S_a}{S_{FD}} - 1 \right) \%$$

For the wave geometry, the largest percentage difference between the analytical sensitivity and the finite difference approximation is $p_d = 0.032\%$. For the twisted roof, the largest percentage difference is $p_d = 0.022\%$. This verifies the implementation as it is within the accuracy of the finite difference approximation. Any difference in the results between the 4-node and 9-node elements can be attributed to the difference in accuracy, the use of a different method for including the drilling DOF in the 9-node element and the different minima found as a consequence of these differences.

The evaluation of strain energy for the finite difference approximation was made using post-processed strain and stress in order to verify the post-processing in addition to the sensitivities. The evaluation of strains and stresses subsequent to a linear static analysis is made using the displacements and internal DOFs to evaluate strains as the sum of compatible and enhanced strains.

$$(7.3) \quad \{\varepsilon\} = \{\varepsilon_c\} + \{\varepsilon_e\} = [B]\{d\} + [\tilde{M}]\{\alpha\}$$

The stresses are found from the strains using the constitutive relation in Eq. (4.35). The strain energy is evaluated as the inner product of stress and strain integrated over the volume.

$$(7.4) \quad U = \int_V \{\varepsilon\} \cdot \{\sigma\} dV$$

The strain energy U evaluated from the post-processed strains and stresses in the wave and twisted roof tests, was observed to satisfy Clayperon's work theorem $2U = C$ through comparison with the compliance C evaluated from Eq. (6.1). This verifies the postprocessing of strains, stresses and strain energy of the element in laminated composite analysis.

Draping Influence on Optimal Candidate Material

The difficulties with finding the global optimum makes it difficult to determine the influence of draped fibre orientations on the optimal design. Despite finding different designs using DMO in all the cases in table 7.7, the compliance is only improved by a small amount in one of the cases. In order to evaluate the influence of draping, an exhaustive search algorithm is used with the 4-node shell to calculate the compliance of all possible designs and determine the global optimum. The results from the exhaustive search can be seen in table 7.8.

4-node shell	Wave		Twisted Roof	
	Without draping	With draping	Without draping	With draping
Optimal design	(15,15)	(0,0)	(-75,60)	(-75,75)
Min. compliance [J]	0.273 (0.301)	0.301 (0.293)	2.94e5 (3.02e5)	2.98e5 (2.96e5)

Table 7.8. Optimal designs found using exhaustive search with the final value of the compliance. Compliance values calculated with draping are in parentheses.

The exhaustive search results in table 7.8 show that accounting for draped fibre angles does influence the optimal nominal fibre angle as both tests found different optimal designs. The percentage improvement in compliance when accounting for draping can be calculated.

$$(7.5) \quad p_d = 100 \left(1 - \frac{C_{drape}}{C_{nom}} \right) \%$$

This yields an improvement when accounting for draping of 2.66% for the wave and 1.99% for the twisted roof. It is clear that accounting for draping can have an influence on the optimal design. However, the difference in compliance between the optimal designs with and without draping is relatively small in the two test examples used. Additionally, the compliance with draping in table 7.7 using the 9-node element disagrees with the improvement in compliance seen with draping in table 7.8 using the 4-node element. However, in more complex optimisation problems, e.g. in optimisation with regards to other objectives or more design variables through more layers, accounting for draping might result in a more definite and significant improvement. It should also be noted that the 9-node element does not utilise the novel method presented in this thesis for the drilling DOF and might provide more questionable results as a consequence. It is difficult to determine if the inclusion of draping will lead to improvements in general, as the nature of the optimisation problems has a large effect on the influence from draped fibre angles. However, inclusion of draped fibre angles provides a more realistic model of the structural behaviour as the draping process is accounted for.

7.2.2 Buckling Optimisation

The buckling optimisation is performed on two test structures without double curvature as draping is not considered. For both structures DMO will be applied to determine the best design against buckling using both the 4-node element presented in this thesis and the 9-node element. The sensitivities calculated at the initial point using the 4-node element will be compared to a finite difference approximation to verify the calculation as done with the linear compliance optimisation.

Clamped Angle

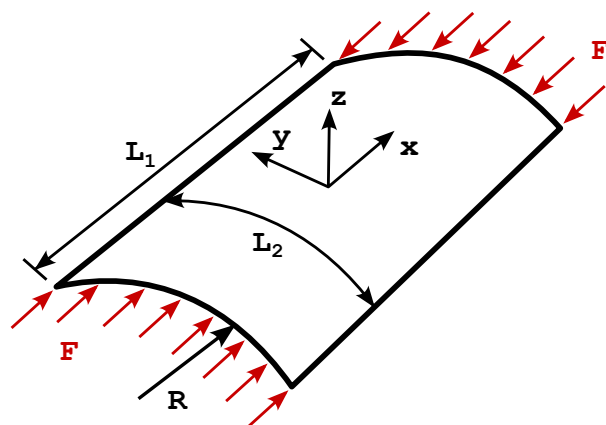
The first buckling optimisation test structure is the clamped angle used in section 7.1 to test the non-linear and buckling capabilities of the shell element. For the buckling optimisation, the structure has been redefined from using an isotropic material to have 2 layers with the same 12 candidate fibre angles for each layer as used in the linear compliance optimisation. Since draping is not considered with buckling, the clamped angle test is allowed to use a different candidate for each element. Each layer uses an orthotropic material with the parameters stated in table 7.9.

E_{11}	E_{22}	E_{33}	G_{12}	G_{23}	G_{13}	ν_{12}	ν_{23}	ν_{13}
71240 Pa	20254 Pa	20254 Pa	7543 Pa	6751 Pa	7543 Pa	0.29	0.3	0.3

Table 7.9. Material parameters of the FRP laminate used in clamped angle test.

Cylindrical Shell Panel

The second buckling optimisation test structure is a shell panel taken from Kühlmeier (2006). The structure is illustrated with loads, supports and geometrical definitions in Fig. 7.15 and table 7.10. The material parameters are listed in table 7.11. The laminate is built up as a sandwich structure with a fixed core material and face sheets composed of 2 layers of orthotropic material. Thickness of the layers are $(0.0012m, 0.0012m, 0.03m, 0.0012m, 0.0012m)$. Each layer in the face sheets has the same 12 candidate fibre angles as used in all previous tests. The core material only has a single candidate corresponding to the fixed material used.



Parameter	Value
Radius R	$0.696m$
Length L_1	$2m$
Width L_2	$0.5m$
Thickness	$0.0348m$
Mesh	24×96
Load F	$10^6 N/m$

Figure 7.15 & Table 7.10. Cylindrical shell panel geometry and loads. The mesh has 24 elements along the width L_2 and 96 elements along the length L_1 . The geometry is supported along all edges, where $v = w = 0$.

	E_{11}	E_{22}	G_{12}	G_{23}	G_{13}	ν_{12}
Face sheets	30.6 GPa	8.7 GPa	3.24 GPa	2.9 GPa	3.24 GPa	0.29
Core	57.5 GPa	0.62 GPa	1.2 GPa	1.1 GPa	1.2 GPa	0.45

Table 7.11. Material parameters of the materials used in the cylindrical shell panel test.

DMO Results of Buckling Optimisation

The optimal design from the buckling optimisation of the clamped angle geometry can be seen in Fig. 7.16 compared between the 4-node and 9-node elements.

The results on Fig. 7.16 show similar results in terms of optimal fibre angles with the same first buckling eigenvalue. It should be noted that the buckling eigenvalues being the same to the third decimal is a coincidence of the slightly different fibre angles and accuracy of the 4-node and 9-node elements. However, the results show that the 4-node shell element is applicable in buckling optimisation using DMO. Additionally, it shows that the implementation allows for each element to have a different candidate.

The results from the buckling optimisation of the cylindrical shell panel can be seen in table 7.12, compared between the 4-node and 9-node elements. The first buckling mode of the initial design with an even mix of candidates and the optimised design can be seen in Fig. 7.17.

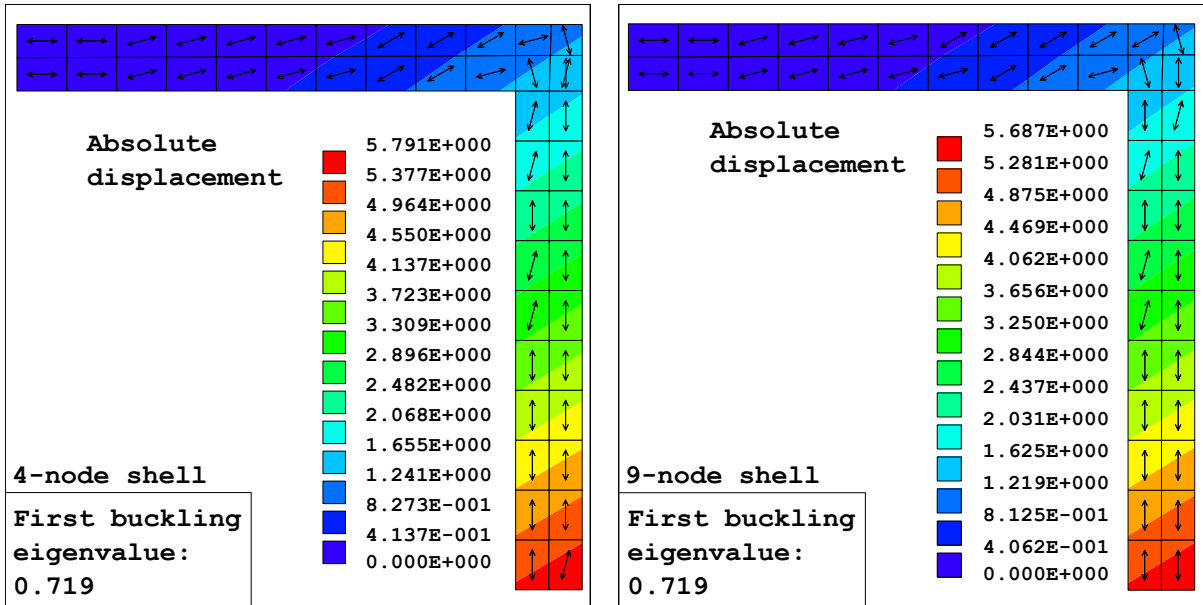


Figure 7.16. Optimal fibre angle indicated by the black arrows in both layers of each element on clamped angle structure found using 4-node and 9-node shell elements. If only one arrow is present the angles are the same in both layers. The absolute displacement is given in meters and taken from the initial linear analysis used for the evaluation of $[K_\sigma]$.

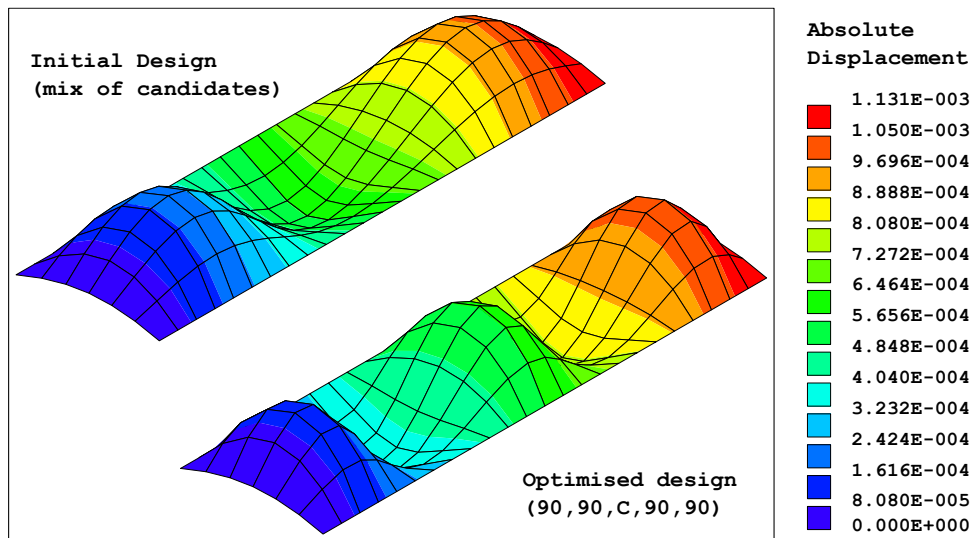


Figure 7.17. First buckling mode of initial design with a mix of candidates and the optimised design of the cylindrical shell panel. C denotes the core layer in the layup. Displacements emanate from the linear static analysis and are given in meters.

Cylindrical Shell Panel	4-node shell	9-node shell
Optimal design	(90,90,C,90,90)	(90,90,C,90,90)
First buckling eigenvalue	13.77	13.40

Table 7.12. Optimal designs found using DMO with the final value of the first buckling eigenvalue. In the design specification C denotes the core layer, which is not varied in the optimisation.

The results of the cylindrical shell panel further confirms the applicability in buckling optimisation with DMO using the 4-node shell element presented in this thesis. Interestingly, the first buckling mode changes from the initial to the optimal design.

Verification of Linear Buckling DMO Implementation

The implementation of the 4-node shell element is verified with regards to buckling optimisation in the same way as for the linear compliance through a comparison of the sensitivities. The sensitivities are compared by the percentage difference calculated using Eq. (7.2). For the clamped angle test, the largest percentage difference is 0.012% and for the cylindrical shell panel the largest percentage difference is 0.019%. These are within the acceptable limit and verifies the implementation. Any difference seen between the optimisation results of the 4-node and 9-node element must therefore be attributed to the difference in element accuracy and the consequent possibility of finding different optima.

7.2.3 Geometrically Non-Linear Compliance Minimisation

The inclusion of large displacements in the element formulation is used in the tests for GNL compliance minimisation. The compliance is evaluated from the displacements of the deformed structure at the end of the non-linear analysis.

The tests are performed on the same geometries as the linear buckling optimisation. Therefore, the GNL compliance optimisation could achieve similar results if the optimal approach in regards to compliance is also to increase the critical buckling load. However, the optimal approach could also be to increase the stiffness of the structure after the critical buckling load is reached, which could result in very different results between the two optimisation methods.

Clamped angle

With the changed clamped angle test problem, the 4-node shell element will be used to minimise the compliance with a GNL analysis. The element formulation is compared with the 9-node shell element in terms of end result and initial design sensitivities. To further test the non-linearity regarded in the analyses, the two shell formulations will also be used in their linear formulation to compare how it affects the formulation to include non-linearities. The minimisation solutions are stated in table 7.13, with the discrete optimum found with 1 patch for the whole structure.

	4-node shell		9-node shell	
	Non-Linear	Linear	Non-Linear	Linear
Optimal design	(60,60)	(0,0)	unconverged	(0,0)
Min. compliance [J]	77.27	2.709 (78.76)	unconverged	2.862 (78.76)

Table 7.13. Optimal designs found using DMO with the final value of the compliance. For the linear optimal designs, compliance values calculated with the 4-node GNL shell formulation are in parentheses.

With the linear formulations, the optimisation with the 4 and 9-node elements reached an identical solution. With the non-linear formulation, the 4-node formulation reached a different solution and the 9-node failed to converge with the same settings for the arc-length solver and also with smaller steps. There is a great difference in the resulting layups for linear and non-linear compliance optimisation, which shows how much different the problem becomes with the non-linearity.

To visualise the structural response, the force displacement curve from the different optimisation solutions are shown in Fig. 7.18, solved with the linear and non-linear 4-node shell element formulations.

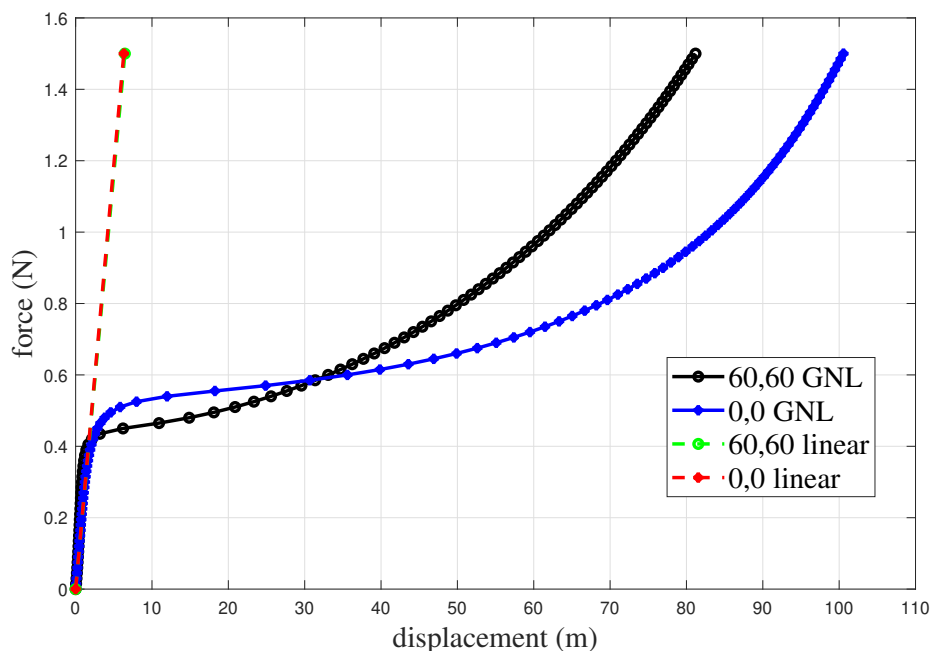


Figure 7.18. Force displacement graph with the optimal laminate obtained in the linear and GNL compliance optimisations.

In the graph it can be seen how the (0,0) layup has a higher buckling load compared to the (60,60) layup. However, after instability it is the (60,60) layup that has the stiffest layup, which makes sense given this behaviour was only modelled with the GNL element formulation. In regards to the initial stiffness all the formulations are quite close, therefore a zoomed in version of the graph is shown in Fig 7.19.

With the zoom in, it becomes more clear to observe the initial behaviour before buckling. It appears from the behaviour until $0.05N$ that the layups behave similarly but with the linear solution the (0,0) layup is slightly more stiff. Interestingly, with the GNL solutions, the (60,60) layup experiences a non-linear behaviour before buckling that causes it to increase in stiffness compared to the more linear behaviour of the (0,0) layup.

It has been shown how including the non-linearity changes the results of the DMO optimisation with a single patch of all elements. Furthermore, it could be interesting to see how the optimisation changes if each element has its own set of design variables. The optimisation completed with the 4-node shell element in MUST with and without GNL is shown in Fig. 7.20.

The analysis with individual element fibre directions clearly show how the optimal fibre angle of almost all the elements in the linear case were 0° or 90° , whereas the non-linear has a wider variety in the optimal fibre angles of each element. In terms of compliance, it can be seen how both are further reduced as the design space has increased.

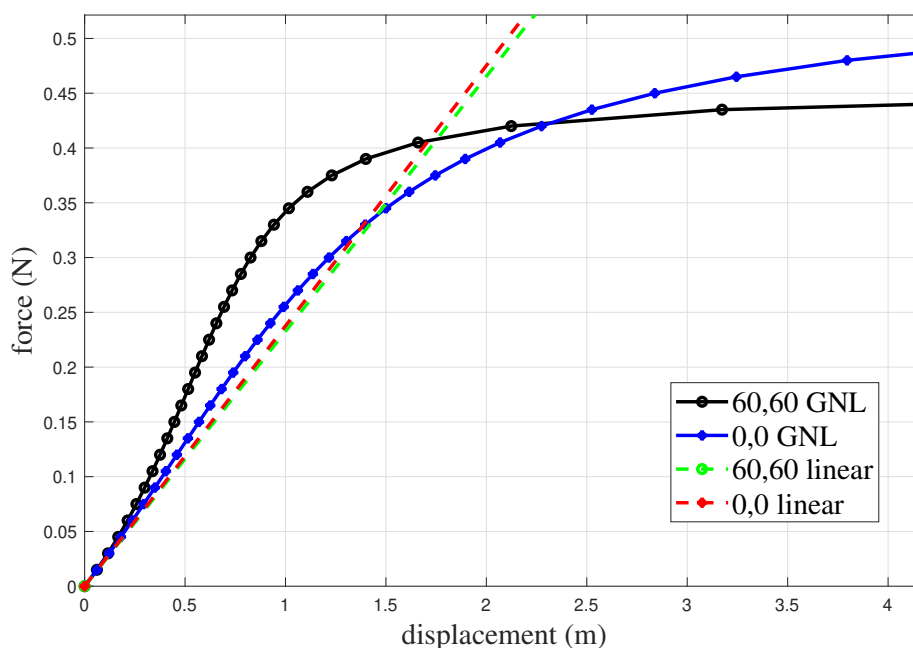


Figure 7.19. Force Displacement graph with the optimal laminate obtained in the linear and GNL compliance optimisations.

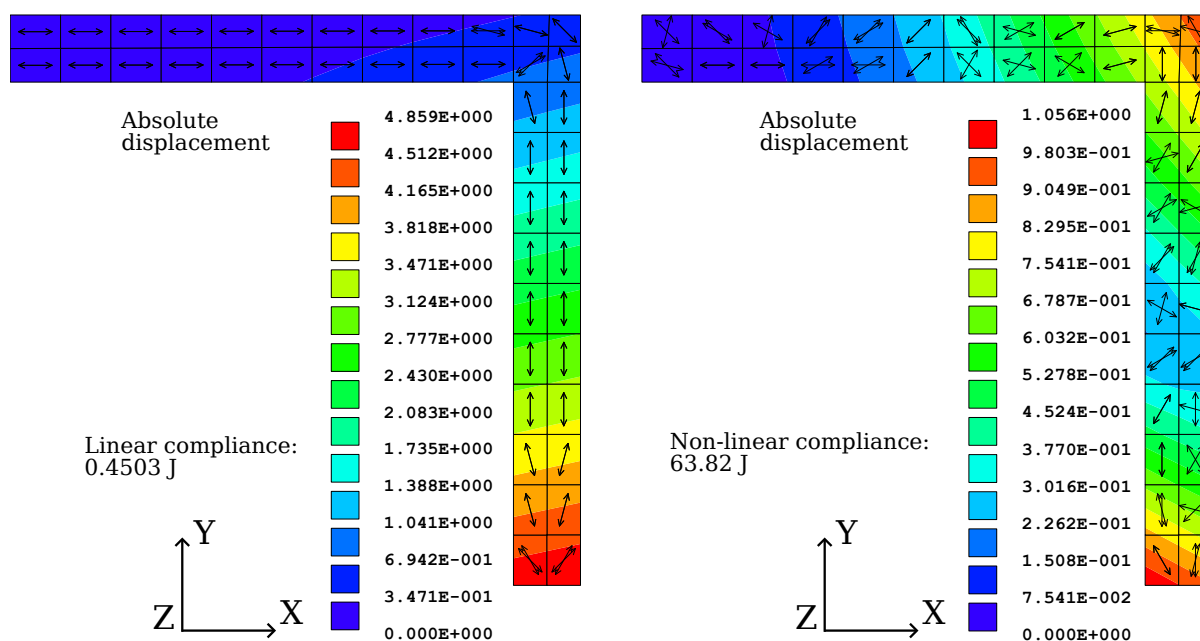


Figure 7.20. Fibre directions for the two layers of the clamped angle geometry with absolute displacement given in meters. The linear element formulation is on the left and the GNL is on the right.

Cylindrical Shell Panel

The other geometry used to test the non-linear behaviour during compliance optimisation is the cylindrical shell panel from Fig. 7.15. The load case has changed in order to make the structure unstable by increasing the primary load and adding a small disturbance load at the middle of the geometry surface. In the linear buckling analysis it was determined that the lowest eigenvalue of

the buckling optimised design was 13.77. For the GNL analyses the primary loads are increased by a factor of 10 as it was observed to be sufficient to cause instability with a disturbance load of $10N$.

	4-node shell		9-node shell	
	Non-Linear	Linear	Non-Linear	Linear
Optimal design	(0,0,C,15,15)	(0,0,C,0,0)	unconverged	(0,0,C,0,0)
Min. compliance [J]	5.646e4	5.437e4 (5.765e4)	unconverged	5.457e4 (5.765e4)

Table 7.14. Optimal designs found using DMO with the final value of the compliance. Compliance values calculated with the 4-node GNL shell formulation are in parentheses. C denotes the core material in the layup definition.

The geometry reaches instability but does not deform much after stability is lost, as shown with the deformed geometry in Fig. 7.21. This explains the small difference between the linear and GNL solution in regards to the compliance shown in table 7.14. Similarly to the clamped angle test, the inclusion of the non-linearity changes the optimal fibre directions and causes a better design to be achieved in regards to the compliance when utilising GNL analysis. As with the clamped angle test, the 9-node shell element could not converge with the arc-length method. Compared to the linear buckling optimisation of the cylindrical shell panel, the non-linear optimisation does not change the first buckling mode.

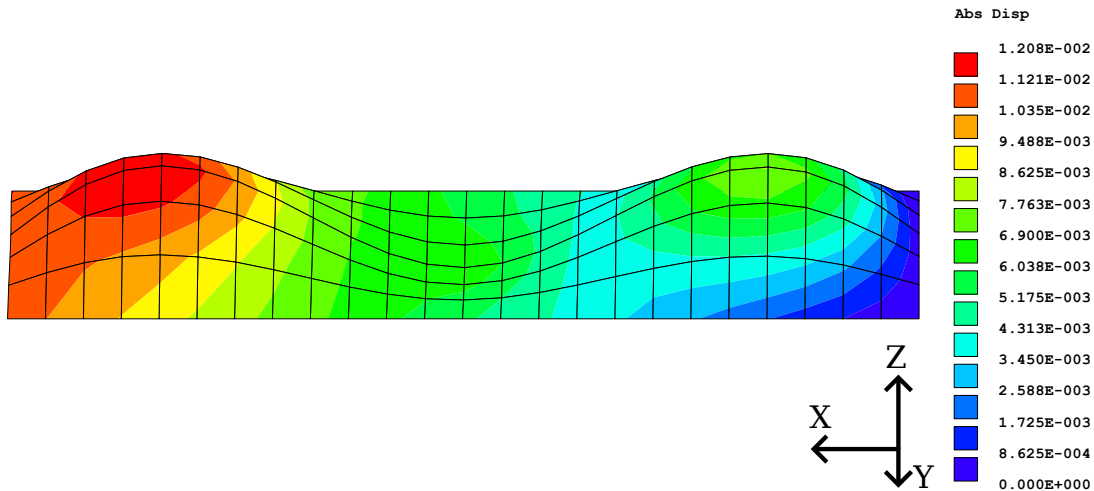


Figure 7.21. Deformed geometry scaled by 20, of the cylindrical shell panel solved with a (0,0,C,15,15) layup. Displacements are given in meters.

Verification of Non-Linear Compliance DMO Implementation

A comparison of design sensitivities is used for verification of the DMO implementation with regards to non-linear compliance optimisation problems. The same approach as for the linear compliance and linear buckling is used. In the non-linear case, only the clamped angle problem is used, as it is possible to use a full Newton-Raphson solver. This solver is needed, as the arc-length solver used for the cylindrical shell panel has slight variations in the load at the end of the analysis. For a finite difference calculation of the sensitivity these slight variations interfere with the finite difference approximation. For the clamped angle non-linear optimisation problem the

largest percentage difference between the sensitivities compared is 0.19%, which is considered acceptable and verifies the non-linear compliance implementation.

7.2.4 Element Formulation Performance in Structural Optimisation with DMO

Through the optimisation tests with the 4-node shell formulation, the design sensitivities and optimised layup have been investigated and compared. The optimisation tests shows the applicability of the presented element for use with DMO in structural optimisation of linear and non-linear compliance as well as linear buckling. The evaluation of the objectives has been verified by the tests in section 5.4 and 7.1. The sensitivities evaluated using the element have been verified by comparison with finite difference approximations using the objective functions. The result is a functional element for use in DMO with linear compliance, linear buckling and non-linear compliance objectives or constraints that can take draped fibre angles into account in both analysis and optimisation. A comparison of the time taken to assemble the global stiffness matrix for 4-node and 9-node elements in the wave test showed that the 4-node element is approximately 5-6 times faster than the 9-node element. Additionally, the 4-node element has proven to be very robust by being able to converge in all the examples tested.

Conclusion 8

This thesis presents the derivation of a geometrically non-linear stabilised 4-node shell element with a novel method for including a drilling DOF and the possibility of accounting for draping in structural analysis and optimisation of laminated composites.

The geometrically non-linear shell element is shown with the non-linear tests and linear buckling analysis in section 7.1 to take large displacements and stress stiffening into account as intended. It manages this using 76% of the iterations used by a similar element from ANSYS Inc. (2018) to achieve convergence for a cylindrical shell under concentrated load, where a similar response was seen.

The novel method presented to include the drilling DOF utilises a transformation of local rotational DOFs from the director coordinate system at each node. The method is applied as a simple expansion without altering existing terms of the 5 DOF stiffness matrix. Applying the method to the linear 4-node shell element resulted in higher or equal accuracy compared to the commercial shell element from ANSYS Inc. (2018) in all tests apart from one. The derived shell element with 6 DOF is capable of achieving the 5 DOF response independent of the penalty stiffness in all cases including curved elements, except if curved edges are used for loads or boundary conditions. This behaviour differ from ANSYS Inc. (2018) and is likely the reason better accuracy was observed in several of the standard FE problems solved. Even in the case of curved edges being loaded, good results are achieved, however the penalty stiffness becomes problem dependent. Additionally, the presented method for including the drilling DOF provides a simple framework for implementing a physically based torsional stiffness using only new terms added to the stiffness matrix.

Draping is included by adding the draped fibre angle deviations from a draping analysis to the nominal fibre angle, which is used for the in-plane rotation of the constitutive matrix of each element. This allows draping to be accounted for in both structural analysis and optimisation. Accounting for draped fibre angles is shown to yield different minimum linear compliance designs using the presented 4-node shell element. For the two test cases, improvements of 2.66% and 1.99% respectively were achieved by accounting for draping. These cases both had relatively large draped fibre angle deviations and the 9-node element provided contradicting results with the same fibre angles. However, the 9-node element does not use the novel method for drilling, which could influence the results and more complex optimisation problems could yield greater benefits from including draping.

Through verification of the design sensitivities, it has been shown that the element is correctly implemented with the DMO method in MUST for linear compliance, linear buckling and non-linear compliance optimisation problems. The 4-node element is shown to assemble the stiffness matrix approximately 5-6 times faster than the 9-node element.

Future Perspective 9

At the end of this master's thesis, there are several areas of particular interest that can be further developed upon to improve the derived element formulation and optimisation process presented.

9.1 Improvements to the Element Formulation

For the 4-node shell element stabilised with EAS and MITC with large displacement taken into account, linear and non-linear test were completed to understand the abilities of the element. Further improvement ideas are given in this section.

Drilling Penalty Stiffness

The novel method for including the drilling stiffness achieves a well functioning element formulation, which could include the drilling DOF without affecting the element behaviour in most cases. In the case of curved edges used for loads or boundary conditions, there was still an effect of the value of the penalty stiffness. To accommodate a general structure, a more physically based stiffness for drilling could be derived, which would allow the element formulation to not be problem dependent in case of curved edges.

Large Rotations

From the non-linear spherical shell and clamped angle tests in section 7.1, a large discrepancy was observed between the present element formulation and the corresponding shell formulation from ANSYS. The discrepancy was attributed to the large rotations being taken into account in the ANSYS shell formulation. To enable the presented element formulation to model general geometric non-linear behaviour more accurately, the element formulation could be further developed to include large rotations.

Analytical Sensitivity Evaluation

The implementation with DMO requires methods for evaluating the sensitivities. This was implemented analytically for the linear compliance optimisation and using finite differences on the element level for linear buckling and non-linear compliance optimisation. It is possible to derive analytical sensitivities for linear buckling and non-linear compliance optimisation, which would significantly increase efficiency in the optimisation. This would be a suitable improvement for extended use of the element with these optimisation objectives.

9.2 Further Optimisation with Draped Fibre Directions

With the draped fibre orientations included for structural analysis and optimisation, further possibilities for optimisation with draping and DMO are given in this section.

Strength Optimisation

The structural optimisation was completed on compliance as a function of the displacements. Another optimisation objective could be to maximise the strength of the laminate by minimising the failure index. It was observed by the authors in a previous semester (Stagsted and Bertelsen, 2022), how the inclusion of draping can have a greater influence on the strength of the laminate than the stiffness. This was due to the changed principal stresses and directions in addition to the changed strength properties as strength also aligns with the fibres. Therefore, an optimisation of the strength could take more advantage of having the draped fibre directions and maybe a greater influence can be observed in optimisation of strength than in compliance.

Draping Design Variables

Another optimisation possibility is to optimise the draping process itself using parameters such as initial fabric contact with the mould as the design variables. Optimisation of the draping parameters does not typically use structural behaviour as objectives. Instead, the shearing angles of the draped fibres are minimised as a measure of the difference between nominal and draped fibre orientations. However, with draping included in the structural analysis and optimisation, the optimisation of the draping process could utilise structural objectives. The initial contact point can influence the draping angles and be included by having additional sets of candidate materials for each origin point investigated. However, with the topology optimisation used in DMO, having additional sets of candidate materials with little difference between them makes it difficult for the optimisation to converge on a single candidate.

It would be possible to optimise with regards to several draping parameters sequentially. E.g. additional candidate materials with different initial contact points could be added after the optimisation of nominal fibre angle. Thereafter, the optimisation of initial contact point would only have to be on the initial contact points for the given nominal fibre angle and the optimisation would have a smaller design space to search.

An optimisation of the draping process could also be fully decoupled from the structural optimisation. By applying DMO, the optimal fibre angle of each element in a structure could be determined. Rather than trying to include draping in the DMO optimisation, a subsequent optimisation of the draping process could be used to minimise the difference between the draped fibre angles of each element and the optimal fibre angles. This would work similarly to existing draping optimisation schemes minimising shearing angles such as that presented in Krogh et al. (2021).

Additions of DMO with Draping

The DMO method used in this master's thesis follows the original method presented in Lund and Stegmann (2005); Stegmann and Lund (2005). Over the years, research and development of additional modifications and improvements have been made. Other parameterisation methods for the optimisation scheme to handle local minima better and convergence could be used and include shape functions with penalization and sequential gradient chase from Bruyneel (2011) and Yan et al. (2022) respectively.

There is also the discrete material and thickness optimisation method from Sørensen et al. (2014), which further allows for optimisation of thickness and manufacturing considerations to reduce delamination failure probability. Using this method with draping data allows for mass minimisation with more physically realistic material data being used in the optimisation.

Bibliography

- Ahmad et al., 1970.** Sohrabuddin Ahmad, Bruce M. Irons and O. C. Zienkiewicz. *Analysis of thick and thin shell structures by curved finite elements*. International journal for numerical methods in engineering, 2(3), 419–451, 1970.
- ANSYS, 2023.** ANSYS. *Large Deformations*, 2023. URL <https://courses.ansys.com/index.php/courses/large-deformation/>.
- ANSYS Inc., 2018.** ANSYS Inc. *SHELL181*, 2018. URL https://www.mm.bme.hu/~gyebro/files/ans_help_v182/ans_elem/Hlp_E_SHELL181.html.
- Arora, 2012.** Jasbir Arora. *Introduction to Optimum Design*. Elsevier, 2012. ISBN 9780123813756. doi: 10.1016/C2009-0-61700-1.
- Bloomfield et al., 2008.** M.V. Bloomfield, C.G. Diaconu and P.M Weaver. *On feasible regions of lamination parameters for lay-up optimization of laminated composites*, 2008. URL <https://royalsocietypublishing.org/doi/10.1098/rspa.2008.0380>.
- Bruyneel, 2011.** Michael Bruyneel. *SFP-a new parameterization based on shape functions for optimal material selection: Application to conventional composite plies*. Structural and Multidisciplinary Optimization, 43(1), 17–27, 2011. doi: 10.1007/s00158-010-0548-0.
- Cook et al., 2001.** Robert D. Cook, David S. Malkus, Michael E. Plesha and Robert J. Witt. *Concepts and Applications of Finite Element Analysis, 4th edition*. Wiley, 2001.
- Creech and Pickett, 2006.** G. Creech and A. K. Pickett. *Meso-modelling of Non-crimp Fabric composites for coupled drape and failure analysis*. Journal of Materials Science, 41(20), 6725–6736, 2006. doi: 10.1007/s10853-006-0213-6.
- Dassault Systemes, 2023.** Dassault Systemes. *Five Degree of Freedom Shells Versus Six Degree of Freedom Shells*, 2023. URL <https://help.3ds.com/2023x/English/DsDoc/SIMA3DXELMRefMap/simaelm-c-shellelem.htm?contextscope=all&id=46a78825ce794ced837f8bdd3416a798#simaelm-c-shellelem-t-FiveDegreeOfFreedomShellsVersusSixDegreeOfFreedomShells-sma-topic21>.
- Dassault Systemes, 2022.** Dassault Systemes. *Composites Modeler for Abaqus/CAE*, 2022. URL <https://www.3ds.com/products-services/simulia/products/abaqus/add-ons/composites-modeler-for-abaquscae/>.
- Denkena et al., 2021.** Berend Denkena, Carsten Schmidt, Simon Werner and Dietmar Schwittay. *Development of a shape replicating draping unit for continuous layup of unidirectional non-crimp fabrics on complex surface geometries*. Journal of Composites Science, 5(4), 1–13, 2021. doi: 10.3390/jcs5040093.

- Dvorkin and Bathe, 1984.** Eduardo N. Dvorkin and Klaus-Jürgen Bathe. *A continuum mechanics based four-node shell element for general non-linear analysis*. Engineering computations, 1(1), 77–88, 1984.
- Dym and Shames, 2013.** Clive L. Dym and Irving H. Shames. *Solid Mechanics : A Variational Approach, Augmented Edition*. Springer New York, New York, NY, elektronisk udgave. edition, 2013. ISBN 9781461460343.
- Fathelrahman et al., 2013.** M. Adam Fathelrahman, E. Mohamed Abdelrahman and A. E. Hassaballa. *Degenerated Four Nodes Shell Element with Drilling Degree of Freedom*. IOSR Journal of Engineering, pages 10–20, 2013.
- Fengler et al., 2018.** Benedikt Fengler, Luise Kärger, Frank Henning and Andrew Hrymak. *Multi-objective patch optimization with integrated kinematic draping simulation for continuous-discontinuous fiber-reinforced composite structures*. Journal of Composites Science, 2(2), 22–, 2018.
- Fleisch, 2012.** Daniel A. Fleisch. *A Student’s Guide to Vectors and Tensors*. Cambridge University Press, 2012.
- Gruttmann et al., 1992.** F. Gruttmann, W. Wagner and P. Wriggers. *A nonlinear quadrilateral shell element with drilling degrees of freedom*. Archive of applied mechanics (1991), 62(7), 474–486, 1992.
- Heinbockel, 1996.** J. H. Heinbockel. *Introduction to Tensor Calculus and Continuum Mechanics*, Department of Mathematics and Statistics, Old Dominion University, 1996.
- Hvejsel and Lund, 2011.** Christian Frier Hvejsel and Erik Lund. *Material interpolation schemes for unified topology and multi-material optimization*. Structural and multidisciplinary optimization, 43(6), 811–825, 2011.
- Johansen, 2009.** Leon S. Johansen. *Analysis and Optimization of Composite Structures using Adaptive Analysis Methods*. Ph.D. thesis, Aalborg University, 2009.
- Jones, 1999.** Robert M. Jones. *Mechanics of Composite Materials*. Taylor and Francis Group, second edition, 1999.
- Klinkel and Wagner, 1997.** S. Klinkel and W. Wagner. *A geometrical non-linear brick element based on the EAS-method*. International journal for numerical methods in engineering, 40(24), 4529–4545, 1997.
- Klinkel et al., 1999.** S. Klinkel, F. Gruttmann and W. Wagner. *A continuum based three-dimensional shell element for laminated structures*. Computers & structures, 71(1), 43–62, 1999.
- Krogh et al., 2021.** Christian Krogh, Brian L.V. Bak, Esben Lindgaard, Asbjørn M. Olesen, Sebastian M. Hermansen, Peter H. Broberg, Jørgen A. Kepler, Erik Lund and Johnny Jakobsen. *A simple MATLAB draping code for fiber-reinforced composites with application to*

- optimization of manufacturing process parameters*. Structural and Multidisciplinary Optimization, 64(1), 457–471, 2021. doi: 10.1007/s00158-021-02925-z.
- Kussmaul et al., 2019.** Ralph Kussmaul, Jónas Grétar Jónasson, Markus Zogg and Paolo Ermanni. *A novel computational framework for structural optimization with patched laminates*. Structural and multidisciplinary optimization, 60(5), 2073–2091, 2019.
- Kühlmeier, 2006.** Lennart Kühlmeier. *Buckling of wind turbine rotor blades : analysis, design and experimental validation*. Ph.D. thesis, Aalborg University, 2006.
- Lim and Ramakrishna, 2002.** Teik-Cheng Lim and S. Ramakrishna. *Modelling of composite sheet forming: a review*. Composites. Part A, Applied science and manufacturing, 33(4), 515–537, 2002.
- Lund, 2022.** Erik Lund. *Analysis of Laminated Composite Structures*, Ph.D. course on Aalborg University, 2022.
- Lund, 2009.** Erik Lund. *Buckling topology optimization of laminated multi-material composite shell structures*. Composite structures, 91(2), 158–167, 2009.
- Lund and Lindgaard, 2021.** Erik Lund and Esben Lindgaard. *Notes for course on Finite Element Methods*, M.Sc. course on Aalborg University, 2021.
- Lund and Stegmann, 2005.** Erik Lund and Jan Stegmann. *On structural optimization of composite shell structures using a discrete constitutive parametrization*. Wind Energy, 8(1), 109–124, 2005. doi: 10.1002/we.132.
- MacNeal and Harder, 1985.** Richard H. MacNeal and Robert L. Harder. *A proposed standard set of problems to test finite element accuracy*. Finite elements in analysis and design, 1(1), 3–20, 1985.
- Meek and Ristic, 1997.** J. L. Meek and S. Ristic. *Large displacement analysis of thin plates and shells using a flat facet finite element formulation*. Computer Methods in Applied Mechanics and Engineering, 145(3-4), 285–299, 1997. doi: 10.1016/S0045-7825(96)01220-0.
- Research and Markets, 2022.** Research and Markets. *Worldwide Fiber Reinforced Polymer Composites Industry to 2026 - by Type, End-user Industry and Geography*, 2022. URL <https://www.globenewswire.com/en/news-release/2022/04/04/2415435/28124/en/Worldwide-Fiber-Reinforced-Polymer-Composites-Industry-to-2026-by-Type-End-user-Industry-and-Geography.html>.
- Schirmaier et al., 2016.** F. J. Schirmaier, K. A. Weidenmann, L. Kärger and F. Henning. *Characterisation of the draping behaviour of unidirectional non-crimp fabrics (UD-NCF)*. Composites Part A: Applied Science and Manufacturing, 80, 28–38, 2016. doi: 10.1016/j.compositesa.2015.10.004.
- Simo and Rifai, 1990.** J. C. Simo and M. S. Rifai. *A class of mixed assumed strain methods and the method of incompatible modes*. International journal for numerical methods in engineering, 29(8), 1595–1638, 1990.

- Sørensen et al., 2014.** Søren N. Sørensen, René Sørensen and Erik Lund. *DMTO - A method for Discrete Material and Thickness Optimization of laminated composite structures*. Structural and Multidisciplinary Optimization, 50(1), 25–47, 2014. doi: 10.1007/s00158-014-1047-5.
- Stagsted and Bertelsen, 2022.** Niklas K. K. Stagsted and Nikolaj Madum Bertelsen. *An Efficient Stabilised Shell Element Taking Into Account Draped Fibre Directions*, 3. Semester M.Sc. Project at Department of Materials and Production, Aalborg University, 2022.
- Stegmann and Lund, 2005.** J. Stegmann and E. Lund. *Discrete material optimization of general composite shell structures*. International Journal for Numerical Methods in Engineering, 62(14), 2009–2027, 2005. doi: 10.1002/nme.1259.
- Tavares et al., 2022.** Rodrigo P. Tavares, Vincent Bouwman and W. Van Paepegem. *Finite element analysis of wind turbine blades subjected to torsional loads: Shell vs solid elements*. Composite structures, 280, 114905–, 2022.
- Taylor et al., 1986.** R. L. Taylor, J. C. Simo, O. C. Zienkiewicz and A. C. H. Chan. *The patch test-a condition for assessing FEM convergence*. International journal for numerical methods in engineering, 22(1), 39–62, 1986.
- Thije and Akkerman, 2005.** R. H. W. Thije and R. Akkerman. *Finite Element Simulation of Draping With Non-Crimp Fabrics*. 15th International Conference on Composite Materials, ICCM-15, 2005 - Durban, South Africa, 2005.
- Tsai and Hahn, 1980.** Stephen W. Tsai and H. Thomas Hahn. *Introduction to composite materials*. Technomic Pub., Westport, Conn., 1980. ISBN 0877622884.
- Vanclooster et al., 2008.** K. Vanclooster, S. V. Lomov and I. Verpoest. *Simulating and validating the draping of woven fiber reinforced polymers*. International Journal of Material Forming, 1(SUPPL. 1), 961–964, 2008. doi: 10.1007/s12289-008-0217-7.
- Vu-Quoc and Tan, 2003.** L. Vu-Quoc and X.G. Tan. *Optimal solid shells for non-linear analyses of multilayer composites. I. Statics*. Computer methods in applied mechanics and engineering, 192(9), 975–1016, 2003.
- Washizu, 1975.** Kyuichiro Washizu. *Variational methods in elasticity and plasticity*. International series of monographs in aeronautics and astronautics ; division 1 : solid and structural mechanics ; vol.9. Pergamon, Oxford (etc.), 2nd ed. edition, 1975. ISBN 0080176534.
- Wilson et al., 1973.** E.L. Wilson, R.L. Taylor, W.P. Doherty and J. Ghaboussi. *Incompatible Displacement Models*. pages 43–57, 1973. doi: <https://doi.org/10.1016/B978-0-12-253250-4.50008-7>. URL <https://www.sciencedirect.com/science/article/pii/B9780122532504500087>.
- Yan et al., 2022.** Jinshun Yan, Pengwen Sun, Lanting Zhang, Weifei Hu and Kai Long. *SGC—a novel optimization method for the discrete fiber orientation of composites*.

Structural and Multidisciplinary Optimization, 65(4), 1–16, 2022. doi:
10.1007/s00158-022-03230-z. URL <https://doi.org/10.1007/s00158-022-03230-z>.

Yang et al., 2000. Henry T. Y. Yang, S. Saigal, A. Masud and R. K. Kapania. *A survey of recent shell finite elements*. International journal for numerical methods in engineering, 47 (1-3), 101–127, 2000.

Strain Displacement Matrix



A.1 Strain Displacement Matrices on Matrix-Vector Form

From the derivation in Vu-Quoc and Tan (2003), the covariant components of the Green-Lagrange strain tensor was defined in Eq. (4.33) repeated below

$$(A.1) \quad E_{ij} = \frac{1}{2} \left(\{G_i\} \cdot \frac{\partial\{u\}}{\partial r^j} + \frac{\partial\{u\}}{\partial r^i} \cdot \{G_j\} + \frac{\partial\{u\}}{\partial r^i} \cdot \frac{\partial\{u\}}{\partial r^j} \right)$$

With the expression of the displacement field derivative as

$$(A.2) \quad \frac{\partial\{u\}_{3 \times 1}}{\partial r_i} = \left[\frac{\partial N}{\partial r_i} \right]_{3 \times 20} \{d\}_{20 \times 1} \quad r_i = r, s, t$$

and the contravariant base vectors $\{G_i\}_{3 \times 1}$, the Green-Lagrange strain tensor can be stated in matrix form as

$$(A.3) \quad \{E_{ij}\} = \begin{Bmatrix} E_{11} \\ E_{22} \\ E_{33} \\ 2E_{12} \\ 2E_{23} \\ 2E_{13} \end{Bmatrix} = \begin{bmatrix} \{G_1\}^T \left[\frac{\partial N}{\partial r} \right] \{d\} + \frac{1}{2} \{d\}^T \left[\frac{\partial N}{\partial r} \right]^T \left[\frac{\partial N}{\partial r} \right] \{d\} \\ \{G_2\}^T \left[\frac{\partial N}{\partial s} \right] \{d\} + \frac{1}{2} \{d\}^T \left[\frac{\partial N}{\partial s} \right]^T \left[\frac{\partial N}{\partial s} \right] \{d\} \\ \{G_3\}^T \left[\frac{\partial N}{\partial t} \right] \{d\} + \frac{1}{2} \{d\}^T \left[\frac{\partial N}{\partial t} \right]^T \left[\frac{\partial N}{\partial t} \right] \{d\} \\ \{G_1\}^T \left[\frac{\partial N}{\partial s} \right] \{d\} + \{G_2\}^T \left[\frac{\partial N}{\partial r} \right] \{d\} + \{d\}^T \left[\frac{\partial N}{\partial r} \right]^T \left[\frac{\partial N}{\partial s} \right] \{d\} \\ \{G_2\}^T \left[\frac{\partial N}{\partial t} \right] \{d\} + \{G_3\}^T \left[\frac{\partial N}{\partial s} \right] \{d\} + \{d\}^T \left[\frac{\partial N}{\partial s} \right]^T \left[\frac{\partial N}{\partial t} \right] \{d\} \\ \{G_1\}^T \left[\frac{\partial N}{\partial t} \right] \{d\} + \{G_3\}^T \left[\frac{\partial N}{\partial r} \right] \{d\} + \{d\}^T \left[\frac{\partial N}{\partial r} \right]^T \left[\frac{\partial N}{\partial t} \right] \{d\} \end{bmatrix}_{6 \times 1}$$

The strain displacement matrix is defined as the deformation-dependent displacement-to-strain operator through

$$(A.4) \quad \{\delta E_{ij}\} = [B(\{d\})] \delta\{d\}$$

The strain displacement matrix is then defined as

$$(A.5) \quad [B] = \begin{bmatrix} \{G_1\}^T \left[\frac{\partial N}{\partial r} \right] + \{d\}^T \left[\frac{\partial N}{\partial r} \right]^T \left[\frac{\partial N}{\partial r} \right] \\ \{G_2\}^T \left[\frac{\partial N}{\partial s} \right] + \{d\}^T \left[\frac{\partial N}{\partial s} \right]^T \left[\frac{\partial N}{\partial s} \right] \\ \{G_3\}^T \left[\frac{\partial N}{\partial t} \right] + \{d\}^T \left[\frac{\partial N}{\partial t} \right]^T \left[\frac{\partial N}{\partial t} \right] \\ \{G_1\}^T \left[\frac{\partial N}{\partial s} \right] + \{G_2\}^T \left[\frac{\partial N}{\partial r} \right] + \{d\}^T \left[\frac{\partial N}{\partial r} \right]^T \left[\frac{\partial N}{\partial s} \right] + \{d\}^T \left[\frac{\partial N}{\partial s} \right]^T \left[\frac{\partial N}{\partial r} \right] \\ \{G_2\}^T \left[\frac{\partial N}{\partial t} \right] + \{G_3\}^T \left[\frac{\partial N}{\partial s} \right] + \{d\}^T \left[\frac{\partial N}{\partial s} \right]^T \left[\frac{\partial N}{\partial t} \right] + \{d\}^T \left[\frac{\partial N}{\partial t} \right]^T \left[\frac{\partial N}{\partial s} \right] \\ \{G_1\}^T \left[\frac{\partial N}{\partial t} \right] + \{G_3\}^T \left[\frac{\partial N}{\partial r} \right] + \{d\}^T \left[\frac{\partial N}{\partial r} \right]^T \left[\frac{\partial N}{\partial t} \right] + \{d\}^T \left[\frac{\partial N}{\partial t} \right]^T \left[\frac{\partial N}{\partial r} \right] \end{bmatrix}_{6 \times 20}$$

The matrix is split into the linear part

$$(A.6) \quad [B_0] = \begin{bmatrix} \{G_1\}^T \left[\frac{\partial N}{\partial r} \right] \\ \{G_2\}^T \left[\frac{\partial N}{\partial s} \right] \\ \{G_3\}^T \left[\frac{\partial N}{\partial t} \right] \\ \{G_1\}^T \left[\frac{\partial N}{\partial s} \right] + \{G_2\}^T \left[\frac{\partial N}{\partial r} \right] \\ \{G_2\}^T \left[\frac{\partial N}{\partial t} \right] + \{G_3\}^T \left[\frac{\partial N}{\partial s} \right] \\ \{G_1\}^T \left[\frac{\partial N}{\partial t} \right] + \{G_3\}^T \left[\frac{\partial N}{\partial r} \right] \end{bmatrix}_{6 \times 20}$$

and the nonlinear part

$$(A.7) \quad [B_L] = \begin{bmatrix} \{d\}^T \left[\frac{\partial N}{\partial r} \right]^T \left[\frac{\partial N}{\partial r} \right] \\ \{d\}^T \left[\frac{\partial N}{\partial s} \right]^T \left[\frac{\partial N}{\partial s} \right] \\ \{d\}^T \left[\frac{\partial N}{\partial t} \right]^T \left[\frac{\partial N}{\partial t} \right] \\ \{d\}^T \left[\frac{\partial N}{\partial r} \right]^T \left[\frac{\partial N}{\partial s} \right] + \{d\}^T \left[\frac{\partial N}{\partial s} \right]^T \left[\frac{\partial N}{\partial r} \right] \\ \{d\}^T \left[\frac{\partial N}{\partial s} \right]^T \left[\frac{\partial N}{\partial t} \right] + \{d\}^T \left[\frac{\partial N}{\partial t} \right]^T \left[\frac{\partial N}{\partial s} \right] \\ \{d\}^T \left[\frac{\partial N}{\partial r} \right]^T \left[\frac{\partial N}{\partial t} \right] + \{d\}^T \left[\frac{\partial N}{\partial t} \right]^T \left[\frac{\partial N}{\partial r} \right] \end{bmatrix}_{6 \times 20}$$

For the 4-node shell element formulation, the derivative of the shape functions with regard to the natural coordinates are given as

$$(A.8) \quad \left[\frac{\partial N}{\partial r} \right] = \begin{bmatrix} \dots & \left| \begin{array}{cccc} \frac{\partial N_i}{\partial r} & 0 & 0 & -\frac{t}{2} \frac{\partial N_i}{\partial r} h_i V_{2i}^{(1)} \\ 0 & \frac{\partial N_i}{\partial r} & 0 & -\frac{t}{2} \frac{\partial N_i}{\partial r} h_i V_{2i}^{(2)} \\ 0 & 0 & \frac{\partial N_i}{\partial r} & -\frac{t}{2} \frac{\partial N_i}{\partial r} h_i V_{2i}^{(3)} \end{array} \right| & \left. \begin{array}{c} \frac{t}{2} \frac{\partial N_i}{\partial r} h_i V_{1i}^{(1)} \\ \frac{t}{2} \frac{\partial N_i}{\partial r} h_i V_{1i}^{(2)} \\ \frac{t}{2} \frac{\partial N_i}{\partial r} h_i V_{1i}^{(3)} \end{array} \right|_i \dots \end{bmatrix}_{3 \times 20} \quad i = 1, 2, 3, 4$$

$$(A.9) \quad \left[\frac{\partial N}{\partial s} \right] = \begin{bmatrix} \dots & \left| \begin{array}{cccc} \frac{\partial N_i}{\partial s} & 0 & 0 & -\frac{t}{2} \frac{\partial N_i}{\partial s} h_i V_{2i}^{(1)} \\ 0 & \frac{\partial N_i}{\partial s} & 0 & -\frac{t}{2} \frac{\partial N_i}{\partial s} h_i V_{2i}^{(2)} \\ 0 & 0 & \frac{\partial N_i}{\partial s} & -\frac{t}{2} \frac{\partial N_i}{\partial s} h_i V_{2i}^{(3)} \end{array} \right| & \left. \begin{array}{c} \frac{t}{2} \frac{\partial N_i}{\partial s} h_i V_{1i}^{(1)} \\ \frac{t}{2} \frac{\partial N_i}{\partial s} h_i V_{1i}^{(2)} \\ \frac{t}{2} \frac{\partial N_i}{\partial s} h_i V_{1i}^{(3)} \end{array} \right|_i \dots \end{bmatrix}_{3 \times 20} \quad i = 1, 2, 3, 4$$

$$(A.10) \quad \left[\frac{\partial N}{\partial t} \right] = \begin{bmatrix} \dots & \left| \begin{array}{cccc} 0 & 0 & 0 & -\frac{1}{2} N_i h_i V_{2i}^{(1)} \\ 0 & 0 & 0 & -\frac{1}{2} N_i h_i V_{2i}^{(2)} \\ 0 & 0 & 0 & -\frac{1}{2} N_i h_i V_{2i}^{(3)} \end{array} \right| & \left. \begin{array}{c} \frac{1}{2} N_i h_i V_{1i}^{(1)} \\ \frac{1}{2} N_i h_i V_{1i}^{(2)} \\ \frac{1}{2} N_i h_i V_{1i}^{(3)} \end{array} \right|_i \dots \end{bmatrix}_{3 \times 20} \quad i = 1, 2, 3, 4$$

For consistency the displacement vector and covariant base vectors are repeated. The displacement vector was given as

$$(A.11) \quad \{d\} = \left\{ \dots \left| u_i, v_i, w_i, \alpha_i, \beta_i \right|_i \dots \right\}_{20 \times 1}^T \quad i = 1, 2, 3, 4$$

The covariant base vectors were given as

$$(A.12) \quad \{G_1\} = \left\{ \frac{\partial X}{\partial R}, \frac{\partial Y}{\partial R}, \frac{\partial Z}{\partial R} \right\}_{3 \times 1}^T$$

$$(A.13) \quad \{G_2\} = \left\{ \frac{\partial X}{\partial S}, \frac{\partial Y}{\partial S}, \frac{\partial Z}{\partial S} \right\}_{3 \times 1}^T$$

$$(A.14) \quad \{G_3\} = \left\{ \frac{\partial X}{\partial T}, \frac{\partial Y}{\partial T}, \frac{\partial Z}{\partial T} \right\}_{3 \times 1}^T$$

A.2 Derivative of Strain-Displacement Matrix

For the stress stiffness matrix, the derivative of the strain-displacement matrix with regard to the degrees of freedom is needed.

$$(A.15) \quad [k_\sigma]_{20 \times 20} = \int_V \left[\frac{d[B]^T}{d\{d\}} \right]_{20 \times 20 \times 6} \{ \sigma \}_{6 \times 1} dV$$

This can be achieved through taking the derivative of the transposed strain displacement matrix by each of the 20 degrees of freedom in the 4-node shell element to achieve a $20 \times 20 \times 6$ matrix.

$$(A.16) \quad \left[\frac{\partial [B]^T_{20 \times 6}}{\partial \{d\}_{20 \times 1}} \right] = \left[\begin{array}{c} \left. \begin{array}{c} \frac{\partial B_{1,i}}{\partial d_j} \\ \frac{\partial B_{2,i}}{\partial d_j} \\ \frac{\partial B_{3,i}}{\partial d_j} \\ \frac{\partial B_{4,i}}{\partial d_j} \\ \frac{\partial B_{5,i}}{\partial d_j} \\ \frac{\partial B_{6,i}}{\partial d_j} \end{array} \right|_i^T \\ \dots \\ \dots \end{array} \right]_{20 \times 20 \times 6} \quad i = 1, \dots, 20 \quad j = 1, \dots, 20$$

Each of the 20 degrees of freedom strain displacement matrix derivative matrices 6×20 are then transposed and multiplied with the stress vector 6×1 and integrated through numerical integration to derive the $20 \times 20 \times 1$ matrix which is equivalent to the 20×20 stress stiffness matrix.

Plots for Non-Linear Problems

B

B.1 Residual Plot Spherical Shell Tests

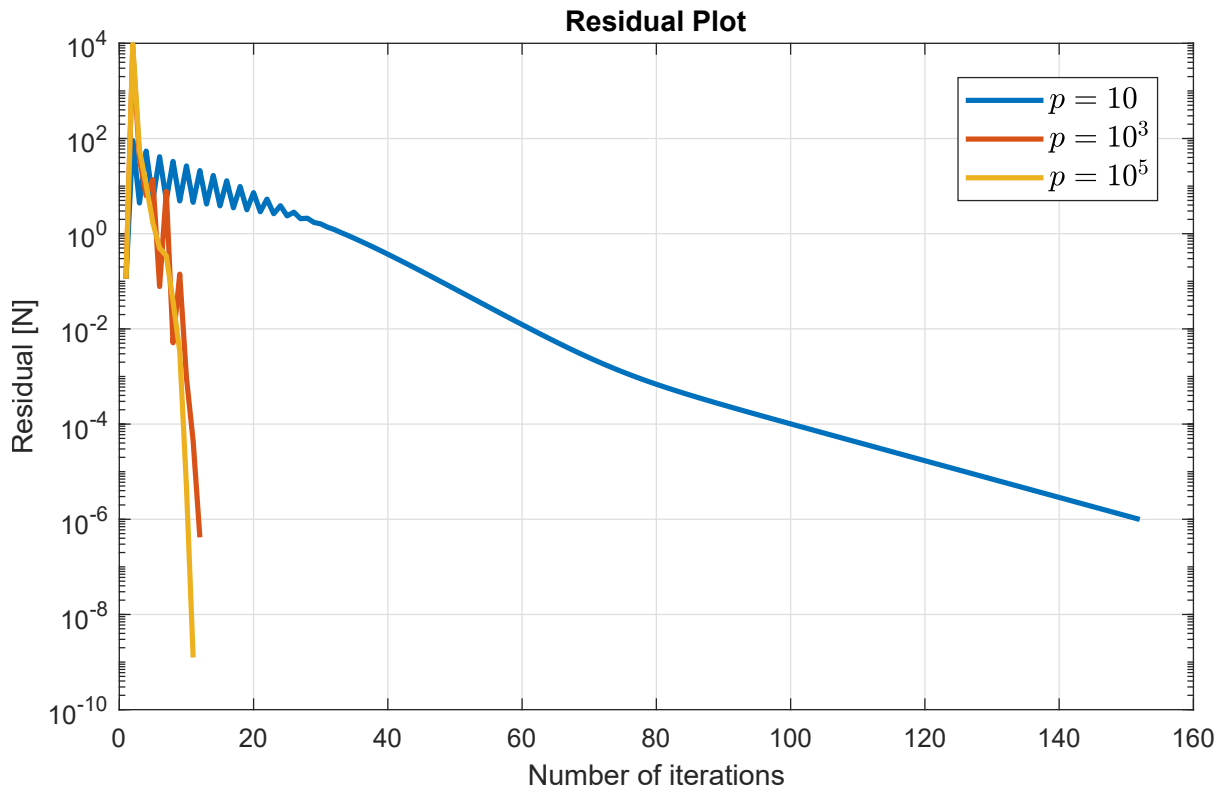


Figure B.1. Log plot of residual at iterations for first load step.

B.2 Clamped Angle Response 5 and 6 DOF

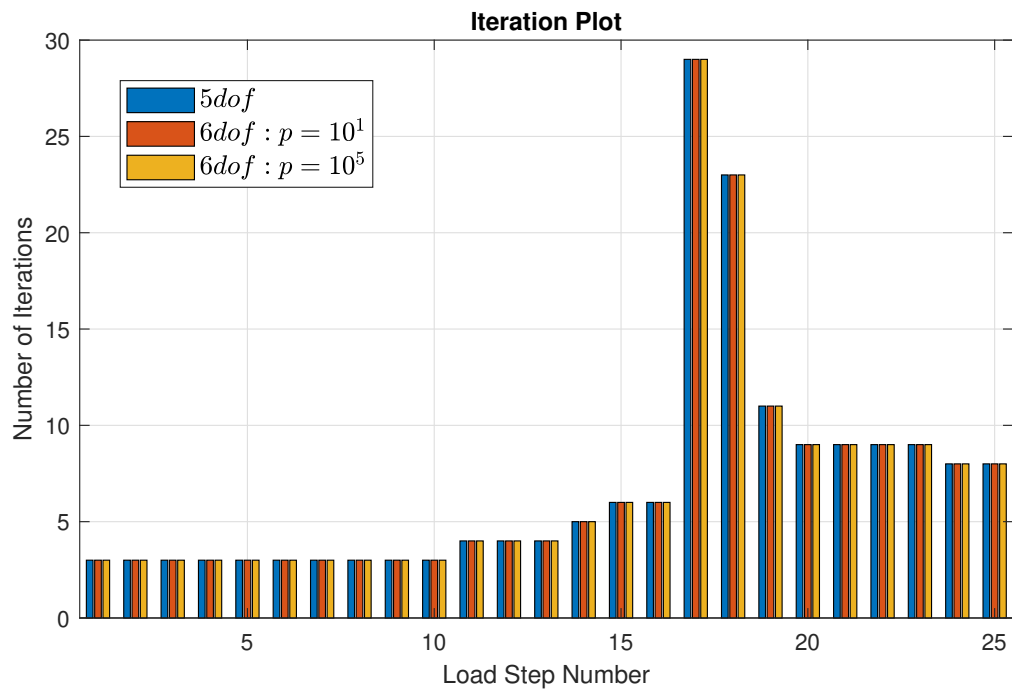


Figure B.2. Iteration plot to solve the clamped angle problem for 25 load steps.